Retinal Ischemia in the In Vivo Rodent: Cellular and Vascular Characteristics

A DISSERTATION
SUBMITTED TO THE FACULTY OF
THE UNIVERSITY OF MINNESOTA
BY

Anja Iwona Srienc

IN PARTIAL FULFILLMENT OF THE REQUIREMENTS
FOR THE DEGREE OF DOCTOR OF PHILOSOPHY

ADVISOR: Eric A. Newman

September 2015

Acknowledgements

I thank my advisor, Eric Newman, for all these years of thoughtful mentorship, guidance, and joyful enthusiasm for scientific inquiry. I am also especially grateful for his steadfast support in my decision to follow a less traditional route through graduate school.

I thank my wonderful family and friends for their patience, humor, and love through all the ups and downs.

I thank my colleagues in the lab for lively, thought-provoking discussions, scientific and otherwise, and for their friendship. Especially to:

> Mike Burian, for his loyal support, technical assistance, and thoughtful advice.
>
> Anusha Mishra, for welcoming me into the lab with such warmth, and for serving as an inspiring role model.
>
> Tess Kornfield, for her creative insights, analytical and programming prowess, encouragement, advice, and playfulness.
>
> Joanna Kur, for her generous willingness to engage in thought experiments and talk through all sorts of problems.
>
> Kyle Biesecker, for his work ethic, dedication, and for being one of the best scientific partners I could have ever hoped to have.
>
> Angela Shimoda, for her cheerful dedication and help with animals.

I thank my committee members, Paulo Kofuji, Erik van Kuijk, and Walt Low, for their insightful ideas related to my thesis project and for being so approachable for scientific discussion outside of committee meetings.

I thank Jan Dubinsky for her scientific mentorship, genuine interest in my career, and supportive encouragement of my goals.

I thank Ann Parr for her clinical mentorship and teaching, and for serving as wonderful role model.

I thank Susan Shurson and Nick Berg for their encouragement, humor, and advocacy.

Portions of this work have been published in *Frontiers in Neuroenergetics* and Astrocytes: Methods and Protocols (ed. Milner, R.). Many thanks to Anusha Mishra and Tess Kornfield for comments on the manuscript and Michael Burian for technical assistance.

Work was supported by Fondation Leducq, NIH EY004077, NIH TRINOD Training Grant, AHA Predoctoral Fellowship 13PRE16960081, and NIH T-32 GM 008244.

I dedicate this dissertation to my family.

To my parents:
For being academic role models and reminding me about balance during the journey

and

To my siblings:
Whose humor and encouragement means more than they know

Table of Contents

List of Tables

List of Equations

List of Abbreviations

LSF – laser speckle flowmetry
RSD – retinal spreading depression
CNS – central nervous system
CSD – cortical spreading depression
ONL – outer nuclear layer
OPL – outer plexiform layer
INL – inner nuclear layer
IPL – inner plexiform layer
GCL – ganglion cell layer
RGC – retinal ganglion cell
NFL – nerve fiber layer
CRA – central retinal artery
IOP – intraocular pressure
NO – nitric oxide
PLA_2 – phospholipase A_2
EETs – epoxyeicosatrienoic acids
PGE_2 – prostaglandin E_2
20-HETE – 20-hydroxyeicosatetraenoic acid
tPA – tissue plasminogen activator
IOS – intrinsic optical signal
AV – arteriovenous
ERG – electroretinogram
HIF-1α – hypoxia inducible factor 1α
VEGF – vascular endothelial growth factor
BRVO – branch retinal vein occlusion
BRAO – branch retinal artery occlusion
CRVO – central retinal vein occlusion
CRAO – central retinal artery occlusion
POAG – primary open angle glaucoma
TA – triamcinolone acetonide
IP – intraperitoneal
IV – intravenous
GPS – gonioscopic prism solution
GECI – genetically encoded calcium indicator.

List of Figures

Abstract

Retinal vessel occlusion is among the leading causes of vision loss. The functional & cellular effects of acute loss of blood flow have not been investigated fully, and current treatments only address secondary complications of ischemic damage. This work has developed new tools with which to investigate retinal blood flow and glial Ca^{2+} signaling in health and disease. Retinal blood flow in the rat was examined by using an imaging technique known as laser speckle flowmetry (LSF) to generate two dimensional maps of blood flow changes. We demonstrated that the inner retinal and choroidal circulations could be imaged noninvasively, and used this technique to study functional hyperemia responses in the retina. We discovered that blood flow increases were more difficult to evoke in areas away from primary arterioles, suggesting that capillary regulation of functional hyperemia is unlikely. To determine the role of glial Ca^{2+} signaling on neurovascular coupling, we developed a method of injecting Ca^{2+} indicator dyes and caged Ca^{2+} compounds into the vitreous, near the retinal surface. This study demonstrated that glial Ca^{2+} signaling plays a role in retinal blood flow regulation. Finally, using a variety of imaging tools, including LSF, we discovered that retinal spreading depression (RSD) is evoked by acute retinal ischemia. RSD in the in vivo, vascular retina has never previously been seen. Spreading depression in the cortex has been shown to play a role in expanding brain injuries. Our observation of RSD is an important finding that carries exciting clinical implications and may be a promising therapeutic target for preventing vision loss after retinal ischemia.

CHAPTER 1: Introduction

The retina is a highly specialized sensory tissue responsible for processing light and converting it to neural signals that are analyzed as visual stimuli. As an extension of the central nervous system (CNS), the retina is structurally and functionally similar to the brain, and similarly, has very high metabolic demands. Consequently, loss of blood flow to the retina results injury and cell death that lead to vision loss. The time course of retinal ischemia has been described histologically to chronicle cellular injury patterns and clinically to understand its natural history and prognosis. Animal models have provided mechanistic insights into the secondary complications of retinal vessel occlusion. However, much less is understood about the functional response to retinal ischemia at the cellular level. In the brain, injury is accompanied by a phenomenon known as cortical spreading depression (CSD), which depolarizes cells, increases glial Ca^{2+} signaling, massively disrupts ion homeostasis, and increases metabolic demand, ultimately exacerbating the injury. Nothing like CSD has ever been observed in the in vivo retina. The aim of this work has been to characterize the cellular, particularly glial, effects of retinal ischemia in an in vivo rodent model, and to determine whether CSD-like events also occur in the in vivo retina in response to ischemic injury.

Retinal anatomy

To appreciate the consequences of ischemic injury in the retina, it is important to understand the retina's cellular and vascular anatomy. This section aims to provide a very brief overview of these topics, but more detailed discussions are provided by [1-3].

The neural retina is a thin tissue found in the posterior part of the eye, between the retinal pigment epithelium and the vitreous body[3], and is organized into specific cell layers (Fig. 1.1) that are defined by the path along which visual information is processed. The retina has two nuclear layers that contain the cell bodies of retinal cells, and two plexiform layers in which synaptic transmission and modulation of information flow occurs. The outer layers lie deeper, while the inner layers are closer to the vitreous body. In order, starting deepest, these layers are: (1) the outer nuclear layer (ONL), made up of the cell bodies of photoreceptors, is where these cells convert photons into chemical signals; (2) the outer plexiform layer (OPL) is the site of synaptic transmission

between photoreceptor cells and bipolar cells; (3) the inner nuclear layer (INL) contains the cell bodies of bipolar cells, but also contains modulatory Müller cells and retinal interneurons (horizontal and amacrine cells), strategically positioning them between the two synaptic layers for effective modulation of retinal processing[4]; (4) the inner plexiform layer (IPL), where bipolar cells signal to retinal ganglion cells; (5) the ganglion cell layer (GCL) is comprised of the cell bodies of retinal ganglion cells (RGCs) and amacrine cells; and (6) the nerve fiber layer (NFL), home to retinal astrocytes and where the axons of RGCs converge on the optic disc to bundle together and exit the retina as the optic nerve[1].

The retinal circulation (Fig. 1.2) reflects the laminar cellular organization of the retinal tissue. Two primary vascular beds supply the retina[2, 3, 5]: (1) the choroid, characterized by its high rate of blood flow and large, dense, fenestrated capillaries, lies behind the retinal pigment epithelium and feeds the metabolically demanding outer retina[6]; and (2) the inner retinal, or superficial, circulation supplies the inner retina and has been the focus of this thesis work. The central retinal artery (CRA), a branch of the ophthalmic artery, enters the retina at the optic disc and gives rise to the inner retinal vascular bed. At the optic disc, the CRA branches into primary branch retinal arterioles that radiate outward towards the retinal periphery. As terminal vessels, they do not anastomose with each other[5]. Rather, these arterioles supply three serially arranged capillary beds that are strategically positioned in series: (i) in the ganglion cell layer, (ii) in the junction between the inner plexiform and the inner nuclear layers, and (iii) in the junction between the inner nuclear and the outer plexiform layers[7]. All three capillary beds drain into small venules to bring blood to the branch retinal venules. Like the primary branch retinal arterioles, these venules also have a radial arrangement at the vitreal surface of the retina and drain into the central retinal vein at the optic disc[2].

Notably, the capillary bed organization of the inner retina ensures that active synaptic zones receive adequate metabolic support while maintaining relative vascular sparseness so as not to interfere with light passage to photoreceptors[8]. When the partial pressure of O_2 is measured at different retinal depths, the distribution of tissue O_2 reflects this trade-off between vascular density and providing metabolic support: tissue O_2 tension is high at the retinovitreous border from the superficial capillary bed but quickly drops to its nadir of ~3 mmHg in the highly active inner plexiform layer where the

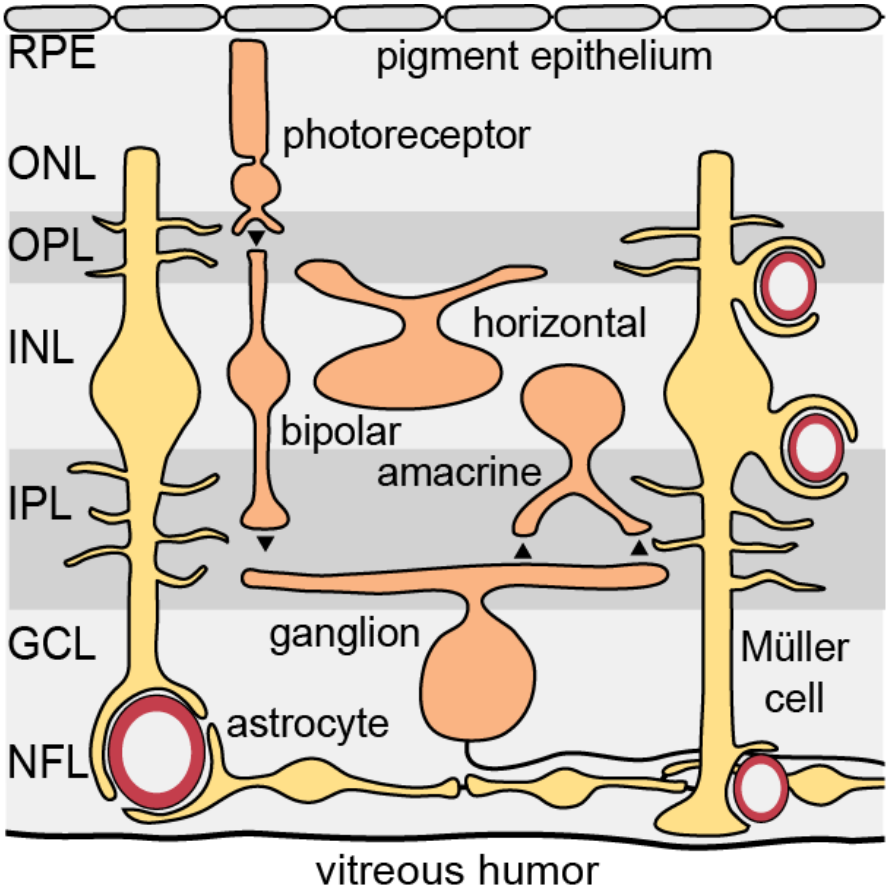

Figure 1.1. Laminar organization of the retina. Retinal neurons are orange and retinal glia are yellow. RPE, retinal pigment epithelium. ONL, outer nuclear layer. OPL, outer plexiform layer. INL, inner nuclear layer. IPL, inner plexiform layer. GCL, ganglion cell layer. NFL, nerve fiber layer. Note how Müller cell processes extend into the plexiform layers. Red circles represent the inner retinal circulation, with the larger circle representing the primary branch vessels, and the three smaller circles representing the three capillary beds that arise from the inner retinal circulation. Modified from [9].

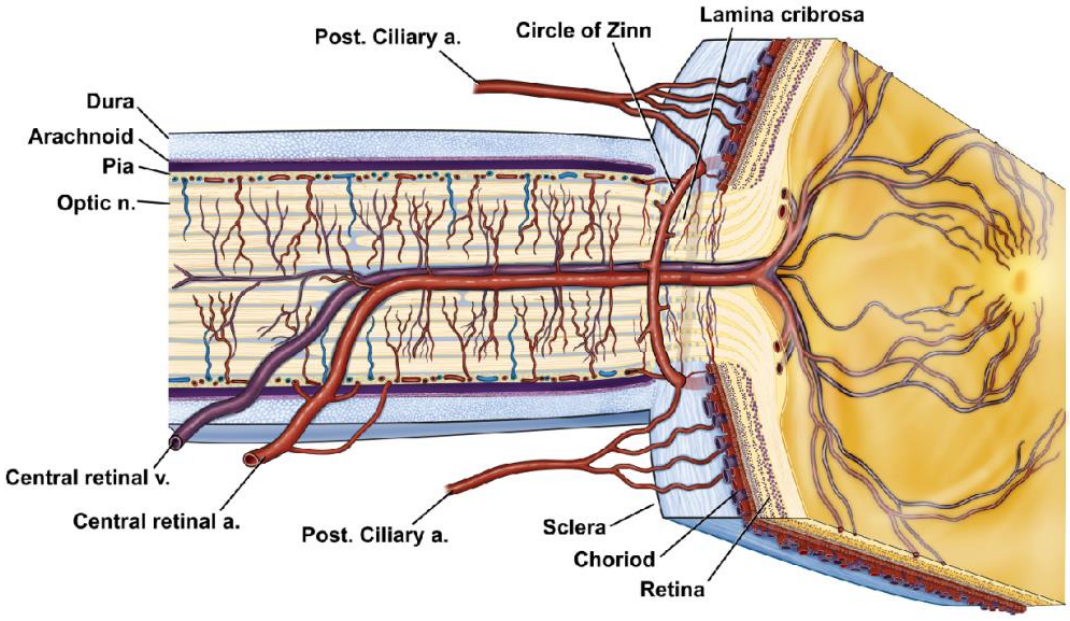

Figure 1.2. Retinal circulation. Cross sectional depiction of the optic nerve and the blood vessels that run with it. The point on the retinal surface where the central retinal artery enters and the central retinal vein exits the retina is the optic disc. From [3].

intermediate capillary layer is the least dense[7]. Tissue O_2 tension is rescued slightly by the deepest capillary layer, but drops again due to the high metabolic activity of the photoreceptor inner segments before steadily increasing again with as measurements move closer to the choroid[8].

Müller cells

Müller cells are the principle glial cells of the retina and function analogously to the brain's astrocytes. Unlike astrocytes, however, Müller cells have a unique radial glia-like morphology because they extend from the subretinal space to the vitreous body, spanning the entire thickness of the retina[10, 11]. As a result, they are ideally positioned to provide metabolic and functional support to all retinal layers. Among other functions, Müller cells take up and recycle neurotransmitters. They have transporters for a variety of transmitters, including glutamate[10]. Not only does such uptake effectively help terminate synaptic transmission to fine-tune signaling, but subsequent conversion of glutamate to glutamine provides the substrate for synthesizing the anti-oxidant, glutathione, and supplements other cells with the necessary precursor for glutamate or GABA synthesis[10, 12, 13]. Müller cells can also modulate neuronal activity by releasing gliotransmitters such as D-serine[14], ATP[15], and glutamate[15, 16] onto neurons. Additionally, Müller cells play a critical role in maintaining the extracellular milieu to optimize neuronal signaling. Neuronal activity results in extracellular K^+ increases, and without rapid clearance of this ion, cells would depolarize. Müller cells provide a functional network to spatially buffer local K^+ increases[17] by taking up K^+ ions through Kir4.1 channels[18] and depositing K^+ in areas away from the site of neuronal activity in the vitreous humor[19, 20]. Finally, Müller cells are critical for regulating blood flow[21]. This is discussed in the next section.

Metabolic support: blood flow

The retinal circulation delivers O_2 and glucose to retinal cells and takes away metabolic byproducts. Therefore, ensuring adequate blood flow is critical for proper retinal function. Two factors determine blood flow through a tissue: (1) the perfusion pressure driving blood into the vascular bed, and (2) the resistance of the circulatory bed being perfused. In the retina, perfusion pressure is determined by the difference between arterial pressure in the ophthalmic artery and the intraocular pressure (IOP)[22]. Since arterial pressure and IOP can vary, autoregulation ensures physiological blood flow across variable parameters. The mechanisms underlying autoregulation of retinal blood flow are

controversial. In the CNS, blood flow is regulated by signaling molecules as well as by perivascular nerves that control blood vessel tone[23]. While there is evidence for autonomic innervation of retinal vessels[24], retinal vessel tone is thought to be controlled largely by humoral mechanisms[22]. For example, nitric oxide (NO) appears to regulate vascular tone in human subjects in response to changes in blood pressure, but not IOP[25]. Additionally, retinal endothelial cells have mechano-receptors that can respond to changes in perfusion pressure and activate myocytes accordingly[22]. Recently, new evidence has emerged that release of ATP, likely from glial cells, is critical for maintaining vascular tone in the inner retinal circulation[26].

While autoregulation is responsible for general blood flow homeostasis, functional hyperemia dictates finer control of retinal blood flow. This phenomenon, first described by Mosso in 1880[27] and then Roy and Sherrington a decade later[28], occurs when blood flow increases locally in areas of increased neuronal activity through a mechanism known as neurovascular coupling. In the brain, diffusible molecules are responsible for vascular responses to neuronal activity. In particular, NO is a potent vasodilator and is produced by neurons in response to NMDA receptor activation by glutamate[29, 30]. However, astrocytes (from herein, referred to as “glia”) are really the central players in mediating neurovascular coupling because their processes border synapses and terminate on blood vessels, ideally positioning them to sense neuronal activity and mediate vascular responses. In the retina and in the brain, synaptically release neurotransmitters diffuse to receptors on glial cells to initiate IP_3-mediated Ca^{2+} increases. Glial Ca^{2+} activates the enzyme phospholipase A_2 (PLA_2), which metabolizes membrane phospholipids into vasoactive metabolites. Specifically, synthesis and release of epoxyeicosatrienoic acids (EETs) and prostaglandin E_2 (PGE_2) result in local vasodilation, while 20-hydroxy-eicosatetraenoic acid (20-HETE) produces vasoconstriction[30]. This same signaling system with Müller cells as the central players functions in the retina, too[21], and Chapters 3 and 4 demonstrate this phenomenon.

Ischemic injury in the brain

Stroke is the second leading cause of death worldwide. Defined as the sudden loss of perfusion to the brain, strokes can be classified as either ischemic (~85%, owing to vascular embolism) and the focus of this work, or hemorrhagic (< 15%, owing to vascular rupture). Hemorrhagic strokes are often lethal, but ischemic strokes carry a 58.4%

survival rate and high rates of secondary morbidity. In fact, health complications due to stroke came at a cost of over 7 billion dollars in the USA in 2010[31]. Current therapies for stroke are limited to interventions that try to reestablish blood flow, such as tissue plasminogen activator (tPA) or endovascular mechanical thrombectomy, and do little to curb secondary complications. tPA, in particular, is only approved for use within three hours of the onset of symptoms and carries a risk of hemorrhagic adverse events[31]. To complicate matters further, reperfusion after a period of ischemia results in reperfusion injury, a paradoxical phenomenon in which delivery of nutrients suddenly provides cells with enough energy to activate apoptotic signaling cascades and generate damaging reactive oxygen species[5, 31].

A variety of animal models have been employed to study the evolution of ischemic injury in the CNS. These experimental systems can create strokes of varying severity by altering duration and method of ischemia. For example, cell culture or brain slices can be subjected to oxygen glucose deprivation[32]. In vivo, the popular middle cerebral artery occlusion generates large strokes[33] in a distribution akin to strokes commonly occurring in humans, and can be made reversible or permanent. Smaller strokes can be produced using a technique called photothrombosis[33-35]. This method relies on a dye, Rose Bengal, whose photoactivation produces localized thrombi by way of local damage to the endothelium[35]. These common models, and many others, have greatly advanced current knowledge about ischemic damage. From these studies, several universal observations have been made.

Firstly, ischemia in the nervous system results in excitotoxicity, a specific type of damage that is unique to the nervous system[5]. The brain's high demand for glucose and O_2 comes from heavy cellular reliance on tightly maintained ion gradients and their rapid restoration after neuronal activity. As a result, disproportionately large amounts of ATP are required to keep Na^+-K^+ pumps running[36]. When blood flow is suddenly lost and oxidative phosphorylation is disrupted, ion gradients fail within minutes, causing cells to depolarize and release glutamate. This sequence of events produces cell damage via several mechanisms: (1) additional depolarization due to transmitter binding at ionotropic receptors (NMDA, AMPA, and kainate) causes shifts in Na^+ and Cl^-, resulting in excess water entry into cells and leading to cell swelling and lysis[5]; and (2) glutamate binding at NMDA receptors results in excess Ca^{2+} influx that can activate a variety of enzymes that

promote cytoskeletal and DNA damage, and overload mitochondrial buffering mechanisms and initiate cell death cascades[5, 31].

Secondly, glial cells contribute to ischemic injury in several ways. First, these cells also serve as a glutamate source during excitotoxicity. Since glial glutamate uptake mechanisms rely on the Na^+ gradient, loss of this gradient impairs glutamate uptake by glia[36]. And under conditions of increased extracellular K^+, the glial glutamate transporter reverses its transport direction causing glia to actively contribute to the rise in extracellular glutamate[37]. Additionally, it is known that glial Ca^{2+} increases under pathological conditions in the CNS[38, 39], including in ischemia[34, 36]. Two forms of glial Ca^{2+} can occur: (1) oscillations limited to single cells, and (2) multicellular Ca^{2+} waves[40]. However, the functional consequences of this Ca^{2+} signaling remain controversial. There is some evidence that glial Ca^{2+} signaling may be protective. One study showed that stimulation of glial Ca^{2+} by activating the purinergic $P2Y_1$ receptor, ischemia-induced dendritic damage and cell death was decreased[41]. Others have shown that glial Ca^{2+} is associated with glutamate release that increases injury[34, 42]. The effect of ischemic glial Ca^{2+} signaling on glial blood flow regulation is unknown. It has been observed that pericytes, contractile cells that enwrap capillaries, contract and stiffen after ischemia, limiting parenchymal blood flow[43, 44]. One speculation is that glial Ca^{2+} signaling may result in the release of a preponderance of vasoconstrictors which could account for some of the observed pericyte constrictions. However, this hypothesis is yet untested.

Thirdly, the immune system plays a critical role in injury expansion and tissue remodeling after ischemic infarction. In the acute phase, thrombus formation and early injury activate components of the innate immune system (ie: microglia), resulting in a positive feedback loop of cytokine release and increased trafficking of more immune cells to the area of damage[45]. While leukocytes do play a role in injury expansion, the mechanisms of their involvement are not yet clear[46]. Over time, the peripheral boundaries of the dead tissue become walled off by reactive astrocytes, and the dead tissue is replaced by a scar. Interestingly, recent evidence has come to reveal that this scar remains populated by immune cells that continue to release cytokines and other factors that may affect the function of nearby healthy tissue. This has become the new hypothesis for the mechanisms underlying vascular dementia, a common complication of stroke in human patients. In support of this theory, it has been shown that stroke scars in

mice become populated with B-cells several weeks after the stroke, and this is associated with cognitive deficits; if B-cells are depleted, cognitive deficits are delayed[33].

Lastly, ischemic injury follows a circumscribed course during which loss of blood flow generates a non-perfused area of tissue, known as the core, and a surrounding hypoperfused penumbra. It has become clear that saving cells from the core is a futile task. However, the penumbra is a dynamic region in which function is impaired, but which can be rescued by timely intervention. Conversely, if left under-perfused, the penumbra can deteriorate into an expanding core. Additionally, the penumbra is the source of peri-infarct depolarizations, a type of cortical spreading depression that can expand the ischemic infarct[47, 48], discussed in the following section.

Cortical spreading depression (CSD)

CSD is a phenomenon that was first described by the Brazilian physiologist Aristides Leão in the rabbit[49]. In trying to evoke epileptic seizures, Leão observed that an intense electrical stimulus produced a silencing of neuronal activity that spread across the cortical surface. This wave of depressed signaling also appeared to have a dramatic effect on blood flow. These original findings were initially taken for a curious phenomenon without physiological relevance. However, strong evidence has accumulated implicating cortical spreading depression as the mechanism that underlies migraine auras[50, 51]. More recently, CSD has also been shown to spontaneously occur in response to severe acute trauma to the brain, such as ischemic stroke, subarachnoid hemorrhage, or traumatic brain injury[52]. Notably, CSD only affects grey matter and cannot be sustained by white matter[53].

CSD is a complex phenomenon that involves massive depolarization of neurons that is accompanied by dramatic shifts in ion gradients and extracellular accumulation of neurotransmitters. While the physiological trigger for CSD remains unknown, there is agreement that synchronous depolarization of a critical volume of tissue, ~1 mm^3 is required[54]. The subsequent rise in extracellular K^+ is rapid and massive: $[K^+]_e$ elevates from ~3 mM to more than 10-fold. Meanwhile, Na^+, Cl^-, and Ca^{2+} travel down their ionic gradients and enter cells[53, 54].

This loss of ion homeostasis has significant consequences. Firstly, the substantial increase in $[K^+]_e$ overwhelms K^+ buffering and clearance mechanisms[19]. As a result, K^+ ions accumulate in the extracellular space, diffuse outward, and promote depolarization of neighboring tissue, thereby propagating the CSD wave. Secondly, depolarization and Ca^{2+} entry promote the release of neuro- and gliotransmitters. These signaling molecules are then free to act synaptically[36] and extra-synaptically[55] to enhance and propagate the CSD depolarization. Finally, entry of ions into cells is accompanied by water influx to cause cell swelling and a decrease in extracellular volume. Cell swelling accounts for changes in reflectance properties of the tissue, a characteristic that can be used to image CSD as an intrinsic optical signal (IOS) by reflectance microscopy[56]. Increased cell volume further promotes transmitter release via volume-activated channels[57]. Cell swelling also decreases extracellular volume, effectively raising the extracellular concentrations of K^+ and neurotransmitters, further promoting depolarization (Somjen). Together, these mechanisms allow CSD waves to propagate out from the initiation point at a rate of ~3 mm/min until they eventually extinguish[49, 53, 54, 58].

Electrophysiologically, CSD is characterized by a transient increase in neuronal firing, followed by a prolonged period of neuronal silence lasting from ~5 minutes[49, 59] to several hours if CSD occurs in injured tissue[60]. Since neuronal spiking activity depends on maintained physiological ion gradients, the period of electrical silence is determined by the time it takes to restore ion gradients following a CSD episode[53]. Spiking activity alone is a poor marker for CSD since, under pathological conditions, spiking activity can be silenced by mechanisms other than CSD[54, 61]. Compared to very rapid action potentials that occur on the order of milliseconds, the massive depolarization of CSD takes several seconds to develop and resolve. As a result, it is more reliable to measure extracellular changes in DC potential where CSD manifests as a negative shift in potential that can be up to 30 mV or more in amplitude and last from a few second to over two minutes[54, 62].

CSD also causes a complex series of blood flow changes. These changes can be divided into four phases. The first phase is a rapid and transient vasoconstriction that coincides with[63] or just precedes[64] the drop in DC potential. Second, there is a period of transient hyperemia that typically begins shortly after the negative DC shift. This

increase in blood flow only lasts a few minutes, but generally outlasts the electrophysiological changes that occur with CSD[54]. Third, there is a smaller, secondary hyperemic response[64]. Finally, an extended oligemia remains for over an hour[54, 65] after the tissue has otherwise recovered from the 2-6 minute long CSD episode[66].

The molecular signals driving each of these blood flow phases remain unclear. For example, the initial vasoconstriction is thought to be caused by the substantial K^+ rise at the onset of SD, since high K^+ has been shown to depolarize vascular smooth muscle cells[63, 67]. However, this initial vasoconstriction is most pronounced for only the first CSD wave; subsequent CSD episodes result in only slight vasoconstrictions, if any at all[63]. It is generally accepted that glial cells play a central role in coupling neuronal activity to changes in blood flow, as discussed earlier. In this model under healthy conditions, the synthesis of dilating molecules prevails over constricting molecules[30]. However, there is evidence that this balance shifts in CSD, resulting in increased 20-HETE, a vasoconstrictor. This shift may account for the prolonged oligemia that follows CSD[68]. However, it is unclear when this shift occurs and how it is regulated. Generally, these blood flow changes have been difficult to study because their courses are influenced by CSD wave frequency[63], animal species[54], anesthesia[69], blood pressure[54], and a plethora of other variables. Nevertheless, it is clear that CSD results in pronounced changes in blood flow that may contribute to CSD's pathophysiological effects.

CSD is a highly metabolically taxing phenomenon. The massive shifts in ion gradients must be restored, a process that is dependent on ATP-driven Na^+-K^+ pumps[53, 54]. As a result, in the minutes that follow a CSD episode, glucose metabolism, glycogen breakdown, lactate production, and tissue demand for O_2 increase dramatically[54]. When tissue is healthy, recovery from CSD occurs without any lasting consequences. However, in the face of injury, these added metabolic demands exacerbate tissue damage and increase cell death, resulting in a perpetuating cascade of additional injury[47, 48]. Additionally, in the ischemic rat cortex, frequent CSD waves have been shown to induce excitotoxic lesions in a glutamate-dependent manner[62]. In human patients recovering from subarachnoid hemorrhage, traumatic brain injury, or malignant stroke, spontaneous SD episodes have been linked to delayed neurological deficits and increased infarct volume[60].

Retinal spreading depression (RSD)

Spreading depression has also been studied in the retina. Less than a decade after the discovery of CSD, Gouras observed a similar phenomenon in the isolated toad retina, appearing as a milky wave that spread over the retinal surface[66]. Since this initial observation, RSD has been widely studied in many animal models, including chick[59, 70, 71], frog[72, 73], carp[74], and salamander[53].

RSD studies have revealed that spreading depression in the retina recapitulates CSD. RSD can be elicited by mechanical or electrical stimulation[59, 66], ions (high K^+ or low Cl^- media)[71-74], glutamate[55, 75], free radicals[70], and injury[76]. RSD propagates at a velocity of 1-10 mm/min[77], is accompanied by cell swelling[56], and results in a negative shift in DC potential and silencing of spontaneous neuronal activity[66, 77]. Also like in the brain, RSD is associated with cell death, as demonstrated by Yu et al.[76]. They showed that a cut injury in the hypoglycemic chick retina can trigger SD episodes that are correlated with increased cell death in the macula. These macular lesions can themselves become new foci for new SD waves[76].

To date, with the exception of one report on cat eyecup[78], all RSD studies have used species with avascular retinas. Investigating RSD in these model systems have been considered an ideal experimental paradigm in which to study the effects of spreading depression on neural tissue, independent of vascular confounds. Additionally, all RSD research has also been limited to ex vivo preparations. Chapter 5 of this dissertation describes the novel finding that the in vivo, vascular retina can sustain spreading depression events, and that RSD in the in vivo rat occurs in response to retinal vessel occlusion.

Ischemic injury in the retina

The retina is susceptible to acute ischemic injury. Embolism of the inner retinal vessels can occur on either the arterial or the venous side of the circulation, and can affect the central retinal vessels or the branch retinal vessels. As mentioned previously, the primary branch vessels of the inner circulation are end-terminal vessels that do not anastomose. Consequently, losing perfusion of a particular vessel results in injury to all the tissue in that vascular territory[5].

Clinically, venous occlusions occur more frequently than arterial occlusions, and occlusions of the primary branch veins of the retina are encountered most often. Many studies have demonstrated that the sites of retinal venous occlusions tend to be at arteriovenous (AV) crossings[79]. Primary branch retinal vessels run together and share a single adventitial sheath. A long-standing hypothesis proposed that occlusions at AV crossings might be due to compression of the flimsy venous vessel walls by thicker arteries, increasing turbulent flow and predisposing to thrombus formation at that site[79]. Recently, a number of reports using a variety of imaging techniques disproved this hypothesis, demonstrating that veins remain uncompressed at AV crossings[79, 80]. Instead, it appears that hypertrophy of the adventitial sheath encompassing the retinal vessels causes trophic alterations to venous endothelial cells, increasing risk of thrombosis at that site[79]. The precise mechanisms have not yet been identified.

The severity of the occlusive injury generally depends on site and duration of occlusion. For example, higher-order branch vessels that supply a smaller territory will produce a smaller lesion; but if considered in functional terms, even a very small lesion may significantly affect vision if it occurs in the macula. Likewise, the shorter time that blood flow is blocked, the more likely the tissue can recover. Regardless of the site of occlusion, the gross histological changes in response to loss of blood flow have been well described. Within only minutes of occlusion, the electroretinogram (ERG) b-wave disappears, indicating bipolar cell dysfunction[81, 82]. By an hour, the retina becomes edematous[81]. This is the primary cause of initial vision loss after vessel occlusion[79, 83]. After several hours, edema peaks and particularly affects the OPL and IPL, with formation of vacuoles in those layers. At this time, pyknotic changes can be observed in the INL and GCL, indicating irreversible DNA changes in cells slated for death[84]. Degenerative changes in cellular organelles can be identified in the INL and GCL by electron microscopy. Cell death peaks between 6-48 hours after occlusion[82]. In the days that follow occlusion, activated microglia and infiltrating macrophages clear cellular debris while occluded vessels and ischemic tissues continues to undergo both necrosis and apoptosis[82]. The injury stabilizes within weeks, but residual changes are still present[81, 83, 85]. Functionally, the b-wave of the ERG remains depressed[82]. Immunohistochemical analysis reveals gliosis in the inner retina, loss of RGCs, retinal thinning, and Müller cell detachment from the inner limiting membrane[81, 82, 85, 86].

These cellular changes are accompanied by a wide array of changes in gene expression that largely promote secondary complications of acute ischemia. Loss of blood flow causes hypoxia, activating hypoxia-inducible factor 1α (HIF-1α). This cascade upregulates vascular endothelial growth factor (VEGF) expression in the ischemic region along with many other pro-angiogenic genes[87-89]. Together, these altered protein expression patterns promote retinal neovascularization. Additionally, VEGF can act on local blood vessels to increase vascular permeability, contributing to retinal edema[87]. While increases in VEGF expression are limited to only the ischemic portion of the retina, changes in other edema-promoting genes occur throughout the whole retina, even in areas that remain perfused[89]. Specifically, there is a decrease in the Müller cell-specific channels, Kir4.1 (an inwardly rectifying K^+ channel) and AQP-4 (aquaporin-4)[89, 90]. Müller cells play an important role in mediating K^+ and water homeostasis in the retina. In the healthy tissue, K^+ is rapidly buffered after neuronal activity, and water follows[10, 19]. The K^+-water transport system is optimized by limiting Kir4.1 and AQP-4 expression to Müller cell processes in the plexiform layers and in the endfeet close to blood vessels[90]. However, in retinal ischemia, the polarity of Kir4.1 and AQP-4 expression is rapidly lost, and there is overall decrease in expression of these channels[10, 90]. As a result, glial water and ion transport is compromised, contributing to retinal edema.

As discussed above, ischemic brain injury is typically associated with an increase in excitotoxic cell death. Likewise, glutamate-mediated excitotoxicity plays a role in retinal ischemic injury. There is a lot of experimental evidence that extracellular levels of glutamate rise during retinal ischemia[5]. This becomes problematic after reperfusion, when glutamate receptors become sensitive to glutamate again. Since neurons of the inner retina, including RGCs, express high levels of ionotropic glutamate receptors, they are more susceptible to subsequent glutamate excitotoxicity[5]. The hypothesis of glutamate-mediated cell death in the retina is supported by observations that exogenously added glutamate produces similar cellular changes as retinal ischemia[84], while pharmacological blockade of glutamate signaling protects against loss of RGCs[91].

It would be remiss not to mention the most glaring difference between retinal and cerebral ischemia: the retina is significantly more resistant to acute ischemic injury than the brain. While the brain becomes irreversibly injured within only a few minutes, the

retina can remain ischemic for nearly 2 hours before cells become irrecoverable[92]. Several reasons for this have been proposed. Firstly, two vascular beds sandwich the retina, and loss of inner retinal blood flow may be rescued by diffusion of O_2 from the choroid. Indeed, this hypothesis was tested to identify whether hyperoxic ventilation could prevent inner retinal dysfunction in retinal artery occlusion. This study found that choroid was unable to provide adequate oxygenation of the inner retina, even in hyperoxia[93]. Alternately, there is evidence that the retina has better sources of energy substrates than the brain: the vitreous contains glucose stores and glycogen, and these stores get depleted during ischemia[94]. These findings, combined with the observation that the retina can derive ATP under anaerobic conditions more efficiently than the brain[5], suggest that the retinal cells can survive longer in conditions of low glucose and O_2. Finally, the edema that accompanies ischemic injury may have more harmful consequences in the brain than in the retina, because cerebral swelling against the immovable cranium may compress additional blood vessels and limit any available collateral perfusion. The retina remains unbound by such physical constraints and can swell into the vitreous without microvascular obstruction[5].

Clinical overview of retinal vessel occlusion

Retinal vessel occlusion accounts for the most common cause of ischemic vision loss after diabetic retinopathy. Clinically, retinal vessel occlusion is classified by vessel type (vein vs. artery) and vessel size (central vs. branch) to create four primary clinical categories: branch retinal vein occlusion (BRVO), central retinal vein occlusion (CRVO), branch retinal artery occlusion (BRAO), and central retinal artery occlusion (CRAO). When relevant, vessel occlusions can also be subcategorized to provide more detail regarding the site of occlusion (ie: optic cup vs. optic nerve head)[95]. Typically, vein occlusion is also subdivided into two categories, major or macular, to indicate embolism of a larger peripheral vein (major) or of a smaller branch in the macula (macular)[96]. The effort to classify retinal vessel occlusion with as much detail and precision as possible comes from observations that different occlusion sites carry different risk factors, implying that differing underlying pathological processes are responsible for retinal vessel occlusions at different sites. For example, age, hypertension, smoking, diabetes, and primary open angle glaucoma (POAG) are all risk factors for developing retinal vessel occlusion, but vein occlusion at AV crossings is much more likely if the patient is a smoker and/or hypertensive, while vein occlusion at the optic cup tends to occur more

often in older patients or those with a history of POAG[95], and arterial occlusion is more likely with underlying systemic disease, such as giant cell arteritis[97]. These underlying risk factors affect prognosis and management strategies.

At clinical presentation, patients typically complain of sudden onset blurring or loss of vision. On fundoscopic exam, the retina is edematous, the affected vessel appears dilated and tortuous with small hemorrhages in a flame-shaped distribution, exudates (areas of fluid or lipid deposition) are often appreciated, and, if the macula is not affected by the occluded vessel, it appears as a cherry-red spot against the edematous retina[79]. Visual acuity and peripheral vision are impaired, but degree of impairment can be quite variable, with a range of visual acuities at time of presentation ranging from better than 20/40 to worse than 20/200. The initial severity of vision loss after vein occlusion may be a useful prognostic indicator for later visual outcomes[79]. A meta-analysis of vein occlusions reported that when initial visual acuity is worse than 20/200, vision does not improve for the majority of untreated patients. Similarly, the visual prognosis for BRAO may a better prognosis, regardless of initial acuity[96] as long as the initial loss of acuity is not too severe[98], while CRAO is associated with worse outcomes[99]. Over time, a significant proportion of patients also experience complications of vessel occlusion: (1) 25-60% of patients develop neovascularization which contributes to vision loss by leading to additional hemorrhage or to retinal detachment from traction of neovascular outgrowths into the vitreous[79]; (2) chronic macular edema occurs in 60% of eyes and is associated with worse visual prognosis[99].

Treatments for retinal vessel occlusions are aimed at reducing secondary complications, since efficacy of thrombolysis alone has yielded conflicting data[79]. The two primary methods of intervention are (1) laser therapy and (2) intravitreal injections. Macular grid laser photocoagulation is a procedure that has been the clinical mainstay in treating macular edema for several decades. This therapy is based on the theory that the underlying causes of edema are leaky microaneurysms, cellular release of factors that promote vascular leakage (ie: VEGF, IL-1β, IL-6, etc.), and dysfunctional fluid clearance by retinal cells. Laser elimination of small areas of tissue in the affected area improves edema by coagulating leaky microvessels and reducing how many cells are secreting these leak factors. Reducing VEGF release also limits neovascularization. Other laser therapies include scatter photocoagulation for treating the peripheral retina, and

arteriolar constriction, a technique that partially coagulates the arteriole feeding the ischemic region in vein occlusion to try to limit vasogenic edema in that area.

Alternately, intravitreal injections can also be used to treat edema and neovascularization. Specifically, intravitreal steroid injections have been shown to be efficacious. One study showed that intravitreal triamcinolone acetonide (TA) reduced macular edema and improved visual outcomes, but best results were obtained when TA was used in combination with macular grid laser photocoagulation[100]. In another study, intravitreal injection of dexamethasone had beneficial short-term effects, but was associated with a higher rate of complications when used long-term[101]. Finally, intravitreal injections of VEGF inhibitors target edema and neovascularization at the molecular level. Many studies have demonstrated improved visual acuity and reduced edema with these drugs[79, 101]. However, the primary disadvantage of VEGF inhibitors is the frequent injections patients must receive in order to continue seeing benefits. Most often, however, these therapies are used in combination at the discretion of the physician to optimize time course and combination of therapies for each patient's particular clinical picture.

It is important to appreciate that, as with cerebral strokes, retinal vessel occlusions have secondary complications that require regular intervention. In most cases, vision never fully recovers. Thus, there is an obvious need for additional comprehensive therapies. The therapeutic advantage to treating retinal vessel occlusions is that interventional time window may be longer than with cerebral stroke, since, as previously discussed, the retina is much more resistant to ischemia. The discovery of RSD (Chapter 5) offers exciting avenues to explore for new therapeutic strategies.

Goals of this project

The goals of this research were to understand the cellular consequences of acute retinal ischemia with the secondary goal of identifying new therapeutic targets to treat retinal ischemic disorders. To accomplish this, it was necessary to establish new in vivo imaging techniques to monitor blood flow (Chapter 3) and glial Ca^{2+} signaling (Chapter 4). These methods were employed to study acute retinal ischemia and led to the discovery of retinal spreading depression (Chapter 5), offering new therapeutic target to limit ischemic vision loss.

CHAPTER 2: Methods

In vivo retina preparation

Experiments were performed on male Long-Evans rats (250–350 g). Animals were treated in accordance with the guidelines of the Institutional Animal Care and Use Committee of the University of Minnesota. The initial surgery was performed under isoflurane anesthesia (2% in 30% O_2/70% N_2, 1 L/min) introduced through a cone covering the mouth and nose. Depth of anesthesia was assessed periodically by paw pinch and depth of breathing: an appropriately anesthetized animal should not be responsive to any paw pinch and breathing should be deep and regular. The femoral vein and artery were cannulated for drug administration and monitoring of blood pressure for experiments (left side for experiments described in Chapter 3, right side for experiments described in Chapter 5).

A tracheotomy was performed to allow for mechanical ventilation of the animal during the experiment. The procedure begins by exposing a 2.5 cm segment of the trachea. The trachea was snipped perpendicularly, between two cartilage segments, and a rat endotracheal tube that was cut to a length of 4 cm was inserted. The tube was slid approximately 2.5 cm into the trachea and secured with suture. The surgical incision was closed and secured with staples. The animal was allowed to breathe on its own through the tracheal tube until all preparatory procedures are complete. The isoflurane cone was moved from the animal's mouth and nose, to the tracheal tube to continue administration of anesthesia.

The animal was wrapped in a heating blanket and placed in a modified stereotaxic frame with a three-point head restraint: standard ear bars and a nose clamp are attached to the frame, and its dimensions are 9 × 40 cm. Metal rods mounted on the two ends of the frame allow for the rat to be rotated around its rostral-caudal axis under the microscope (see Fig. 2.1A).

A bolus of atropine (0.1 mg/kg) was delivered IP or IV prior beginning eye manipulations to counter the oculocardiac reflex, which can reduce blood pressure (see Note 2). The cornea and conjunctiva of the right eye were numbed with proparacaine hydrochloride

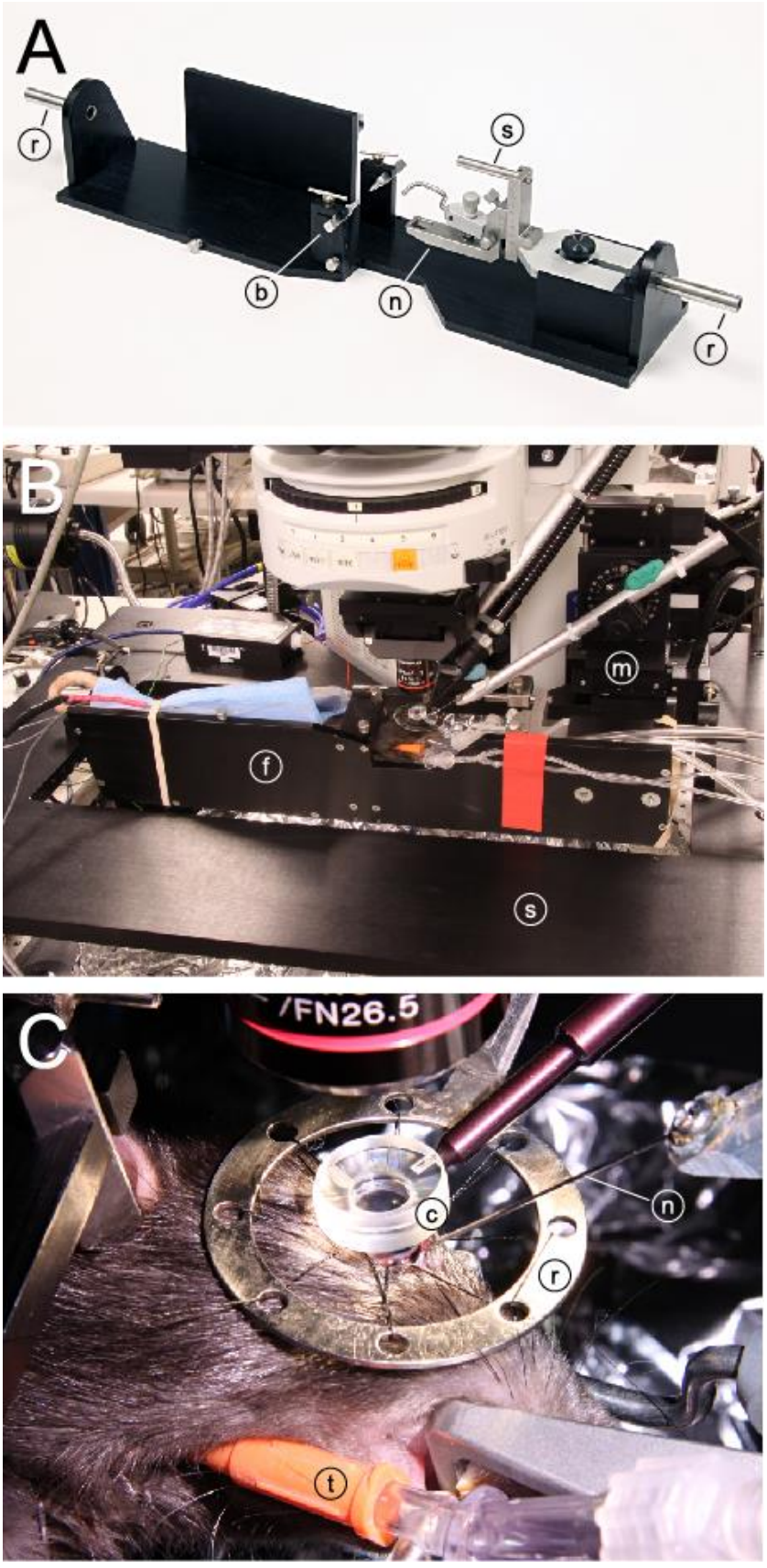

Figure 2.1. Photographs of the in vivo rat preparation. (**A**) Rat stereotaxic frame. A standard nose clamp (n) and ear bars (b) are mounted on a custom frame, which is attached to the microscope stage by the two rods (r) extending from the frame. The eye is sutured to a metal ring (not shown) that is fixed to the frame by a small rod (s). (**B**) An anesthetized rat, restrained in the stereotaxic frame (f), is attached to a movable stage (s) below the microscope. The rat and frame can be rotated around the long axis of the animal to view different regions of the retina. A hypodermic needle is advanced into the eye by a micromanipulator (m). (**C**) The eye is sutured to a metal ring (r), which is attached to the stereotaxic frame. The retina is viewed through a contact lens (c), which neutralizes the optics of the cornea. A guide needle (n), positioned by the micromanipulator, is inserted into the vitreous humor of the eye. The rat is ventilated via a tracheal tube (t).

(0.5% solution) and the pupil dilated with atropine sulfate (1% solution). The eye was sutured to a metal ring (see Fig. 2.1C) to hold it in place and allow penetration of a needle. A metal ring with eight holes spaced along the circumference was secured to the stereotaxic frame and positioned over the right eye. Working clockwise around the ring, the eye was secured to the ring by eight sutures through the conjunctiva. The sutures were tightened until the eye was held firmly without stretching or distorting the eye. One drop of GPS was applied to the cornea. Then, a contact lens was carefully lowered onto the cornea such that the anterior surface of the lens was parallel with the table and the posterior, concave surface of the lens was completely in contact with the GPS, without introducing any air bubbles (see Figs. 2.1C and 2.2A). The handle of the contact lens was secured to the stereotaxic frame with modeling clay. The angle of the contact lens could be adjusted later to maximize the retinal area being imaged (see Note 3).

The stereotaxic holder was fixed to a movable stage below an upright microscope that served to image the retina for both laser speckle flowmetry (LSF) and confocal microscopy (Fig. 2.1B). The frame can be rotated along its long axis to view different regions of the retina. The axis of rotation is in line with the right eye of the rat so that when the frame is rotated, the eye remains stationary and the retina in focus.

Following surgery, anesthesia was maintained for the duration of the experiment by continuous infusion of α-chloralose (55 mg/kg/h). A soluble form of α-chloralose (α-chloralose-HBC-complex, Sigma; see Notes 1 and 4) was used. Animals were paralyzed with gallamine triethiodide (initial bolus of 20 mg/kg and continuous infusion at 20 mg/kg/h) to prevent eye movements. Depth of anesthesia was assessed by monitoring heart rate and blood pressure. The heart rate increases if the animal is underanesthetized. From a nominal level of 90–115 mmHg, the blood pressure increases if the anesthetic level is too light and decreases if it is too heavy. Anesthesia infusion rate was adjusted accordingly (see Note 5). Core body temperature was monitored and maintained at 37°C (TC-1000 Temperature Controller, CWE). The animal was artificially ventilated (40–60 breaths/min; CWE SAR-830-P). Blood O_2 saturation level and heart rate (MouseOx, Starr Life Sciences Corp), arterial blood pressure (Pressure Monitor BP-1, World Precision Instruments), and end-tidal CO_2 (microCapStar, CWE) were monitored continuously. For all experiments that did not involve photothrombosis, blood gases and pH were sampled periodically

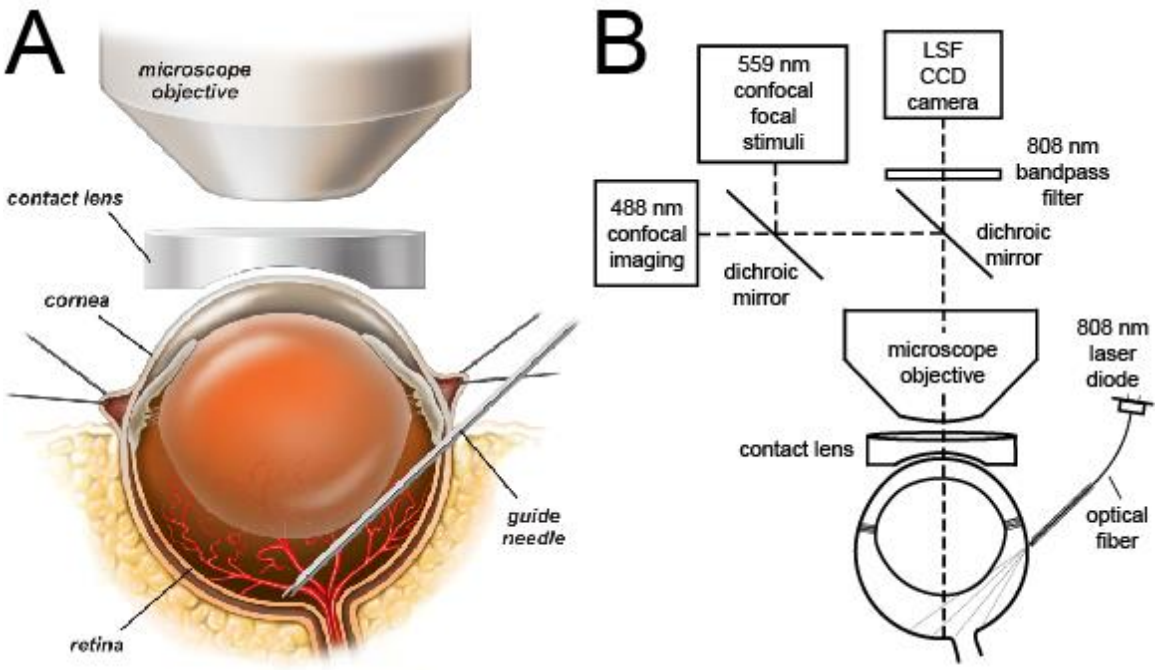

Figure 2.2. Drawings of the in vivo rat preparation. (**A**) The retina is imaged through an upright microscope and a contact lens placed over the cornea. A hypodermic needle is advanced through the sclera into the vitreous humor and serves as a guide needle through which a smaller needle is inserted to eject dyes onto the retinal surface, or through which O_2 sensors or recording pipettes for electrophysiology can be advanced to the retinal surface. Alternately, the guide needle can remain outside the globe be used to position an optical fiber for LSF illumination. (**B**) The schematic shows the optical path for imaging the retina with confocal microscopy while simultaneously monitoring retinal blood flow with laser speckle flowmetry (LSF). The retina is illuminated for LSF by 808 nm light passing though an optical fiber that is pressed against the outer surface of the eye. A dichroic mirror directs the appropriate wavelengths of light from the retina to the LSF camera and the confocal microscope. An 808 nm bandpass filter prevents confocal excitation or emission light from entering the LSF camera. The confocal microscope has a primary scanner (488 nm) for imaging retinal vessels and a secondary scanner for generating 559 nm stimulating light flashes. The secondary scanner also generates 405 nm light pulses for photolysis of caged compounds or 559 nm light pulses for activation of Rose Bengal for photothrombosis. See [102] for a further discussion of LSF. Modified from[102].

(Instrumentation Laboratory Gem Premier 3000) and maintained within physiological limits (pO_2: 100–125; pCO_2: 35–45, and pH: 7.35– 7.45, respectively) by adjusting the O_2 level of inspired air and the ventilator breath rate and pressure (see Note 6).

Retinal imaging

The retina was viewed through the cornea and lens with an Olympus BX61W1 upright microscope and 4× and 10× dry objectives. The refractive properties of the cornea were neutralized by placing gonioscopic prism solution and a contact lens (5.4 mm fundus laser lens, Ocular Instruments) over the cornea (Fig. 2.1C and 2.2A). A CoolSnap ES digital CCD camera (Photometrics) was attached to the phototube of the microscope for LSF. The retina was imaged simultaneously with an Olympus FluoView 1000 laser scanning confocal microscope. Light from the retina was separated by a dichroic mirror (T600lpxr, Chroma Technology) in the microscope, with 808 nm light passing through to the LSF digital camera and 400–600 nm wavelengths reflected into the confocal scanner (Fig. 2.2B). An 808 nm bandpass filter was placed in front of the LSF camera to block residual visible wavelengths.

Confocal microscopy

In Chapters 3 and 4, the diameter of retinal arterioles was monitored with laser scanning microscopy. Blood vessels were labeled by IV injection of dextran–fluorescein (2,000,000 MW, 1 ml, 3% solution) and imaged with 488 nm illumination (see Fig. 2.3A). Alternately, dextran rhodamine B isothiocyanate dye (0.5 mL) and 559 nm illumination was used to image retinal vessels if glial Ca^{2+} was being monitored simultaneously using 488 nm illumination (see Fig. 4.1). By using the confocal microscope in the “line scan” mode, both the diameter of retinal vessels[102] and the velocity of red blood cells flowing through vessels[103] can be monitored. In the resulting distance vs. time line scan images (see Fig. 2.3B) vessel dilation is seen as a widening of the bright lumen of the vessel.

In Chapter 5, the retinal surface was imaged by reflectance microscopy with 405 nm illumination. For photothrombosis, Rose Bengal was administered IV (70 mg/kg bolus; Sigma 330000) and imaged with low intensity 559 nm illumination. Blood vessels were labeled by IV injection of dextran–fluorescein (2,000,000 MW, 0.3 ml, 1.5% solution) and

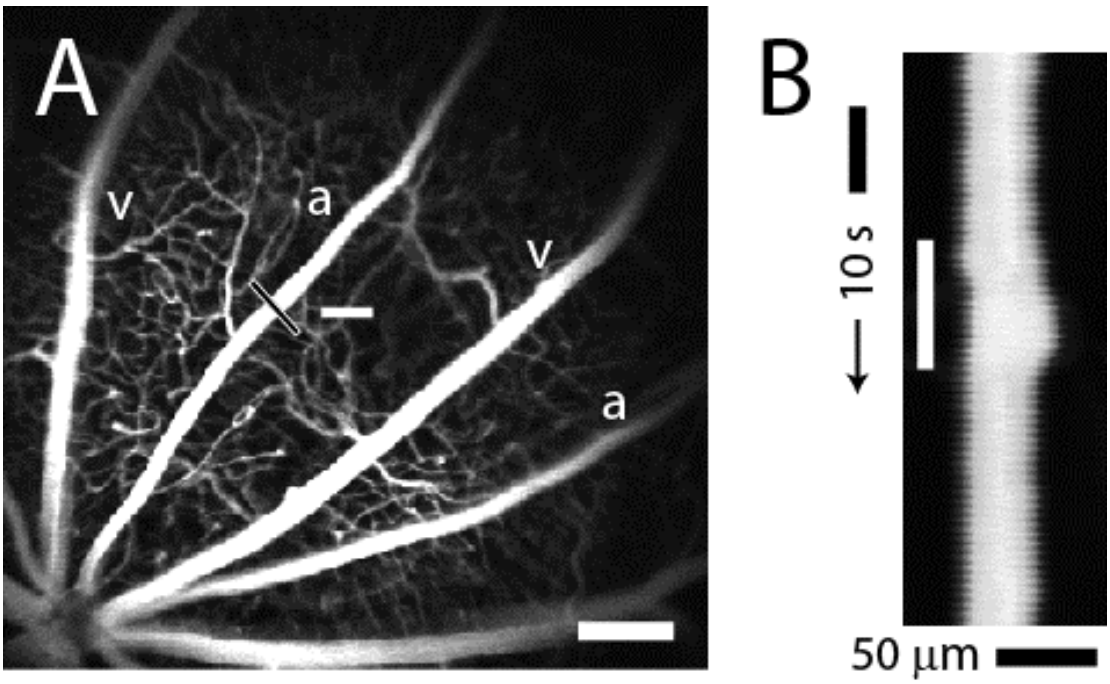

Figure 2.3. Confocal images of retinal vessels. (**A**) Retinal arterioles (a), venules (v), and capillaries are filled with dextran fluorescein isothiocyanate and imaged with confocal microscopy. The optic disc is at the lower left. The luminal diameter of the upper arteriole is measured with confocal line scans (black line). The nearby white bar indicates the location of the flickering light stimulus. Scale bar, 250 μm. (**B**) Line scan image obtained from the arteriole in (A). Distance (across the black line in (A)) is plotted as a function of time. A flickering light (white bar in (B)) evokes vessel dilation, indicated by the widening of the vessel cross section. The uneven edges of the vessel are caused by a respiratory movement artifact. Modified from [102].

imaged with 488 nm illumination; for assessment of vessel diameter changes, line scans were created post-hoc from these whole-frame images using a custom MatLab routine.

Laser speckle flowmetry

Retinal blood flow was monitored by LSF. The retina was illuminated with 808 nm infrared light from a laser diode (200 mW, L808P200, ThorLabs) and imaged with the digital camera. The retina was illuminated by focusing light from the laser diode onto one end of an optical fiber (240 μm diameter) and placing the other end of the fiber against the globe. The end of the optical fiber was positioned on the eye at a 35° angle from the horizontal, approximately 1.5 mm below the limbus. The precise position of the end of the optical fiber was adjusted to maximize signals from the retinal vasculature and minimize signals from the choroidal circulation. The infrared beam emerging from the optical fiber was sufficiently dim as to not cause damage to the eye and was kept on continuously.

Images of the retina were acquired with a 30-40 ms exposure time. In preliminary experiments, we found that shorter exposure times reduced the speckle signals in smaller vessels, while longer exposure times decreased the signals in larger vessels[104]. Two-dimensional LSF images were calculated using a custom MatLab routine. Raw images were spatially binned into 5 × 5 pixel arrays and speckle contrast values computed using the following relation[105],

$$Speckle\ contrast\ value = \frac{Standard\ deviation\ of\ pixels\ in\ array}{Mean\ intensity\ of\ pixels\ in\ array} \qquad \text{(Eq. 1)}$$

LSF ratio images, showing changes in blood flow produced by light stimulation, were computed by first averaging all speckle images acquired before a stimulus and the images acquired during a stimulus and dividing the latter averaged image by the former. Ratio images were low pass filtered to reduce noise. In ratio images, regions with values less than 1 (decreased speckle contrast) indicate areas of stimulus-induced increase in blood flow.

The relative velocity of blood flow can be derived from speckle contrast values using a computationally intensive relation[106]. However, over the limited range of speckle contrast

values that we observed experimentally (0.2–0.4), relative velocity values can be approximated using the following relation[107],

$$Velocity\ \alpha\ \frac{1}{(speckle\ contrast)^2} \qquad \text{(Eq. 2)}$$

We used this relation to compute blood velocity images from speckle contrast images. As above, images showing changes in blood velocity were obtained by computing blood velocity ratio images. Blood velocity images obtained during light stimulation were divided by those obtained during a pre-stimulus period.

Light stimulation

In Chapters 3 and 4, retinal photoreceptors were stimulated by light generated by the secondary (SIM) scanner of the FluoView 1000 laser scanning confocal microscope. Using the SIM scanner, the wavelength, intensity and scanning of a laser beam can be controlled independently of light from the primary scanner, which was used to acquire confocal and line scan images of retinal vessels.

We stimulated retinal photoreceptors with a 12 Hz flickering 559 nm light of 15 s duration. This wavelength is near the maximal absorption wavelength of rat photoreceptors[108] and it does not interfere with the imaging of retinal vessels, which utilizes 488 nm excitation and a 500–550 nm emission bandpass. The luminous flux of the stimulus was 0.02 lumens. A flicker frequency of 12 Hz was chosen because it produces a maximal functional hyperemia response in many species[109]. A flicker rate of 12 Hz with a duty cycle of 50% was generated by scanning a 135 by 20 μm region of the retina with the secondary confocal scanner. With a pixel dwell time of 100 μs, this elongated horizontal rectangle was scanned downwards in 42 ms. At the end of the scan, the 559 nm light was blanked and the beam returned to the top of the rectangle. The return scan took an additional 42 ms. When the scan is repeated continuously, a flickering 12 Hz light is produced. Although the dimensions of the scanned rectangle were chosen to generate the appropriate stimulus frequency, the rectangular region is sufficiently small compared to the overall size of the retina to be useful for mapping localized hemodynamic responses.

Retinal photoreceptors were also stimulated with a 12 Hz diffuse white light having a luminous flux of 1.9 lumens falling on the eye. Light from a fiber optic illuminator was gated with an electromechanical shutter and focused onto the eye through a fiber bundle. This light effectively stimulated the entire retinal surface.

Labeling and stimulating glial cells

The Ca^{2+} indicator dye Oregon Green 488 BAPTA-1AM (OGB) was used to label glial cells (see Note 7). The labeling solution was prepared immediately before use by mixing 3 µL OGB (300 µg/mL) with 1 µL pluronic F-127 (7 mg/mL), 3 µL serine (100 µM), and 25 µL saline (see Note 8). For experiments where glial cells were stimulated, 3 µL of the caged Ca^{2+} compound NP-EGTA was included in the labeling solution.

Prior to labeling, the vitreous humor was digested by enzymatic treatment with hyaluronidase to achieve efficient retinal glial cell labeling. 10 µL of hyaluronidase in saline (125 U/10 µL) was loaded into a Hamilton syringe attached to a 31-gauge needle. The needle was inserted into a 25-gauge guide needle until the tip of the inner needle was in line with the tip of the guide needle. With the animal mounted under the microscope, the guide needle was inserted through the sclera and into the vitreous humor at a 35° angle from the horizontal, approximately 1.5 mm below the limbus. Once the 25-gauge guide needle had passed through the sclera and retina, the 31-gauge needle was advanced through the guide needle until it was touching the surface of the retina (see Fig. 2.2A). The needle was positioned under confocal observation using reflected light to view the retina. The hyaluronidase solution was injected onto the surface of the retina at several locations. The needle was then withdrawn from the surface and the preparation was maintained for 1–2 h as the hyaluronidase broke down the hyaluronic acid of the vitreous humor. After the rest period of 1–2 h, the labeling solution was injected into the vitreous humor. 10 µL of the labeling solution was loaded into the same 31-gauge needle attached to the Hamilton syringe, which had been withdrawn from the 25-gauge guide needle. The 31-gauge needle was reinserted into the guide needle, which had remained in the eye. The labeling solution was injected into the vitreous humor near the retinal surface. Good labeling of glial cells was achieved 60–90 min after injection of the solution. The dye and caged Ca^{2+} compound were taken up selectively by the glial cells of the retina[110] (see Fig. 4.1).

Glial cells were stimulated by photolysis of caged Ca^{2+} with 405 nm light (see Note 9). The uncaging light was generated by the SIM scanner of the confocal microscope and was focused onto a small 5–10 µm spot on the retinal surface using the tornado scan mode of the SIM scanner (see Note 10). A 10 ms to 1 s pulse of 405 nm light was sufficient to generate a large Ca^{2+} increase in the stimulated cells (see Fig. 4.2A). Photolysis of caged Ca^{2+} often evoked a propagated Ca^{2+} wave that traveled into adjacent glial cells.

Photothrombosis

In Chapter 5, photoactivation of Rose Bengal for photothrombosis was achieved using the SIM scanner's 559 nm laser. The "tornado" bleach setting was used to focus light onto a ~20 µm area on a primary retinal vessel.

Electrophysiology

Extracellular recordings of retinal ganglion cell (RGC) activity and the DC potential were conducted in ex vivo eyecup and in vivo preparations. Eyecups were prepared as previously described[111]. Briefly, eyes from 2-3 month old male Long Evans rats were bisected at the equator and everted over a dome in a custom superperfusion chamber[111]. The eyecup was superfused at 2-3 ml/min with bicarbonate Ringers solution bubbled with carbogen at 33 deg C. Retinas were imaged by reflectance microscopy with a confocal microscope (Olympus FV1000) and a 10X water immersion objective. Recording pipettes (~10 µm tip diameter) were filled with bicarbonate Ringers and advanced into the RGC layer. Signals were band-pass filtered (156 – 1800 Hz) to record RGC spike activity and low-pass filtered (0.2 Hz) to record DC potentials. K^+ gluconate ejection pipettes were filled with 150 mM K^+ gluconate and positioned just above the retinal surface at the periphery of the eyecup. For OGD experiments, eyecups were superfused with OGD Ringers solution.

For in vivo electrophysiology experiments, recording pipettes (~0.5 µm tip diameter) were filled with 3 M NaCl. Pipettes were advanced though the sclera and vitreous within a 25 gauge guard needle attached to a custom microadvancer[112]. The pipette was advanced ~10 µm into the retina. Signals were low-pass filtered (0.5 Hz) to record DC potentials.

Oxygen partial pressure

O_2 tension at the surface of the retina was measured with a custom optical O_2 probe (OxyLite NX pO_2 Bare Fiber Beveled Sensor; Oxford Optronix Ltd.) that was advanced through the sclera and vitreous humor inside a 25 gauge guard needle. The O_2-sensitive tip of the probe was beveled so that it lay flat against the surface of the retina when it was in place. Control experiments demonstrated that the photothrombosis bleaching light did not interfere with O_2 measurements.

Red blood cell flux

Red blood cell (RBC) flux through arterioles was measured as previously described[113]. Briefly, blood was withdrawn from the animal at the beginning of an experiment and RBCs were isolated and incubated for 5 min in the fluorescent lipophilic dye DiD (carbocyanide 1,1'-dioctadecyl-3,3,3',3'-tetramethylindodicarbocyanide,4-chlorobenzenesulfonate salt solid; Invitrogen; #D-7757). Cells were washed to remove unbound dye and reinjected into the animal. Fluorescent RBCs were imaged with 635 nm confocal line scans oriented perpendicular to the vessel lumen. Line scans were acquired at 4200 Hz and labeled RBCs detected by a custom MatLab routine.

Immunohistochemistry

A modified in vivo preparation was adopted to permit animal survival following thrombus formation. Animals were anesthetized with 2% isoflurane and the tail vein cannulated for delivery of alpha chloralose anesthetic and Rose Bengal dye. Animals breathed a mixture of 30% O_2 and 70% nitrogen. O_2 saturation was monitored by pulse oximetry to ensure adequate ventilation. Following 60 minutes of photothrombosis, the animal recovered from anesthesia. Animals were sacrificed after 14 days and the retina was removed from the experimental eye and fixed in 4% paraformaldehyde for 2 hours. Retinas were immunolabeled for the RGC marker Brn3a with primary goat antibodies (1:500; 24 hours; sc-31984, Lot # L2414; Santa Cruz Biotechnology) and Alexa Fluor 488 donkey anti-goat secondary antibodies (1:500; 2 hours; A11055; Lot # 1369678; Life Technologies) as previously described[114]. The retinal vasculature was labeled with Isolectin GS-IB4-647 (1:75; 2 hours; Invitrogen I32450). Retinas were imaged with confocal microscopy. To confirm loss of RGCs, retinas were also imaged with infrared differential interference contrast microscopy.

Solutions

All pharmacological agents that were injected i.v. during in vivo experiments were dissolved in medical grade saline. Bicarbonate Ringers solution used in eyecup exeriments contained, in mM: 111 NaCl, 3.0 KCl, 2.0 $CaCl_2$, 1.0 $MgSO_4$, 0.5 NaH_2PO_4, 15.0 dextrose, 32 $NaHCO_3$ (bubbled with 95% O_2 and 5% CO_2, pH 7.4). OGD Ringers solution contained, in mM: 111 NaCl, 3.0 KCl, 2.0 $CaCl_2$, 1.0 $MgSO_4$, 0.5 NaH_2PO_4, 15.0 sucrose, 32 $NaHCO_3$ (bubbled with 95% N_2 and 5% CO_2, pH 7.4).

Image processing

LSF images were analyzed using a custom MatLab routine as previously described[102]. Ratio speckle images were calculated by first averaging all speckle images acquired before vessel occlusion and the images acquired during occlusion and dividing the latter by the former. Vessel diameter measurements were analyzed from confocal line scans using a custom MatLab routine. Alternately, line scans were created from confocal images post-hoc and analyzed using a different custom MatLab routine. RSD waves were analyzed from reflectance intrinsic optical signal (IOS) images using a custom MatLab routine. IOS images were acquired at 0.61 Hz. Δ intensity/intensity IOS images were calculated by low pass filtering each frame to reduce noise, then subtracting from each frame the mean of the preceding 20 frames and then dividing that difference by the mean. These images highlighted the leading edge of the RSD waves. Matlab routines also calculated the radius and velocity of RSD waves based on a user-specified identification of wave origin and the distal extent of the wave. RBC flux confocal line scan images were analyzed using a custom MatLab routine as previously described[113].

Statistics

Data are presented as mean ± SEM. Comparisons between two groups were performed using two-tailed Student's t-test. The parametric version of the test was chosen when variances were equal between groups, while the non-parametric version of the test was chosen for groups with unequal variances. When multiple groups were compared to the same control, statistical differences were calculated using an ANOVA with a post-hoc Dunnett's correction. Calculations were carried out in Excel (2013) or GraphPad Prism (version 5.04).

Notes

1. α-Chloralose HBC complex, rather than uncomplexed α-chloralose, is used, as the HBC complex of α-chloralose is fully soluble in water while uncomplexed chloralose is difficult to solubilize. Chloralose concentrations are specified for the molecular weight of the α-chloralose HBC complex, which is ten times the molecular weight of the uncomplexed α-chloralose.
2. The oculocardiac reflex is triggered by pressure on the eyeball or traction on the extraocular muscles and results in a decrease in heart rate and blood pressure. The reflex is a parasympathetic response mediated by the trigeminal and vagus nerves. It can be prevented by intravenous injection of the muscarinic antagonist atropine, which blocks the vagal reflex.
3. The GPS solution sometimes leaks out from under the contact lens during the course of an experiment. If this occurs, the contact lens is removed, more solution added to the cornea, and the contact lens replaced. Alternately, additional GPS solution can be injected under the contact lens using a syringe with a 25-gauge needle.
4. The choice of anesthetic is critical when characterizing vascular responses. Some anesthetics suppress the functional hyperemia response while α-chloralose leaves the response largely intact[115].
5. It is particularly important to maintain blood pressure within the normal range when characterizing vascular responses. If blood pressure drops below the physiological range, the diameter of retinal arterioles oscillates and the functional hyperemia response is lost.
6. It is critically important to maintain blood gases within the physiological range when characterizing vascular responses. High pO_2 results in attenuation of light-evoked vasodilation while low pO_2 leads to vessel oscillations and a loss of light-evoked dilation. A pulse oximeter can be used to continuously monitor blood O_2 saturation, which gives an estimate of blood pO_2 levels. Blood pH is also important. If the pH falls outside the normal range, either high or low, light-evoked vasodilations are attenuated or are eliminated and vessels may oscillate. pCO_2 is directly linked to pH and can be monitored continuously by measuring end-tidal CO_2 levels.
7. The Ca^{2+} indicator dye Fluo-4 is often used to measure glial Ca^{2+} and was used previously to monitor Ca^{2+} levels in the isolated retina preparation[116]. However,

we find that Fluo-4 is ineffective in labeling retinal glial cells in vivo while OGB labels both astrocytes and Müller cells. OGB has a higher Ca^{2+} affinity than does Fluo-4 (K_d of 170 vs. 345 nM) and this may account for the difference in labeling.

8. Pluronic F-127 facilitates the uptake of OGB and NP-EGTA into retinal glial cells. Eserine inhibits esterases in the vitreous humor and prevents cleavage of the AM ester groups of OGB and NP-EGTA until it enters the glial cells[117].
9. 405 nm light, rather than UV light (normally employed for photolysis of caged compounds), is used in this preparation for several reasons. First, the plastic contact lens and the lens of the eye are transparent at 405 nm but not at UV wavelengths. Second, confocal microscopes are typically equipped with 405 nm but not UV lasers. Third, the optics of the SIM scanner of the Olympus FV1000 microscope is not compatible with UV wavelengths.
10. Due to chromatic aberration of the eye, 405 nm light projected onto the retina is distorted. A 5 µm spot will be blurred to a circle ~40 µm in diameter. In addition, the spot will be displaced laterally if the illumination is off axis.

CHAPTER 3:
Imaging retinal blood flow with laser speckle flowmetry

Summary

Laser speckle flowmetry (LSF) was initially developed to measure blood flow in the retina. More recently, its primary application has been to image baseline blood flow and activity-dependent changes in blood flow in the brain. We now describe experiments in the rat retina in which LSF was used in conjunction with confocal microscopy to monitor light-evoked changes in blood flow in retinal vessels. This dual imaging technique permitted us to stimulate retinal photoreceptors and measure vessel diameter with confocal microscopy while simultaneously monitoring blood flow with LSF. We found that a flickering light dilated retinal arterioles and evoked increases in retinal blood velocity with similar time courses. In addition, focal light stimulation evoked local increases in blood velocity. The spatial distribution of these increases depended on the location of the stimulus relative to retinal arterioles and venules. The results suggest that capillaries are largely unresponsive to local neuronal activity and that hemodynamic responses are mediated primarily by arterioles. The use of LSF to image retinal blood flow holds promise in elucidating the mechanisms mediating functional hyperemia in the retina and in characterizing changes in blood flow that occur during retinal pathology.

Introduction

Laser speckle flowmetry (LSF) has been successfully employed to measure blood flow in the CNS for three decades. It has the distinct advantage over other methods of monitoring blood flow, such as laser Doppler flowmetry, as it can produce two-dimensional images of blood flow with high spatial and temporal resolution.

The principals underlying LSF have been described in detail elsewhere[104-106]. Briefly, when an optically rough surface is illuminated with coherent light, a speckle pattern is produced as the incident light is reflected off of surfaces lying at different depths. Some areas of the surface appear bright due to constructive interference while other areas appear dark due to destructive interference. If the surface is stationary, the speckle pattern of bright and dark spots will remain stationary as well. However, if the surface

moves (e.g., blood cells moving through vessels), the speckle pattern will blur with time. Thus, a stationary region on the surface will have a high speckle contrast while a moving region will have a low speckle contrast when imaged over the appropriate time window[104]. In practice, local speckle contrast is calculated by imaging a surface with a digital camera and computing the standard deviation of brightness divided by the mean brightness over a small array of pixels. The resulting speckle contrast value is used to evaluate relative velocity. With modern computational techniques, speckle contrast can be calculated and speckle images analyzed almost instantaneously.

Although LSF has been used in many studies to monitor blood flow in the cortex[118-120], the very first use of LSF was to monitor blood flow in the retina. The first studies[106, 121] were conducted in the early 1980s, before it was practical to calculate speckle contrast with digital techniques. Instead, the retina was imaged on film and speckle contrast images were obtained with high-pass spatial filtering optical techniques. The resulting images displayed patterns of blood flow in the human retina, with arterioles and venules highlighted because the velocity of blood flow was greatest in these vessels.

More recently, LSF has been used to monitor blood flow in the retina using digital cameras and computational techniques to calculate speckle contrast images. Retinal vessels have been imaged in rabbit[122] and rat[123] retinas and changes in blood flow have been monitored in response to varying intraocular pressure and varying levels of inspired O_2. LSF has also been employed to investigate the effects of glaucoma therapies on retinal circulation in rabbits[124], monkeys[125], and people[126] and to monitor the choroidal circulation in patients with polypoidal choroidal vasculopathy[127].

We now describe results obtained using LSF to image blood flow in the in vivo rat retina. The goals of this project were twofold. First, we wanted to develop a technique to combine LSF with laser scanning confocal microscopy of the retina. This would allow us to monitor spatial and temporal patterns of retinal blood flow with LSF while simultaneously monitoring the diameter of retinal vessels with confocal line scans. An added benefit of this technique is that a second channel of the confocal microscope can generate spatially and temporally defined visual stimuli to activate retinal photoreceptors.

The second goal of this project was to determine whether blood flow is regulated at the local level in the retina. In the brain, localized increases in neuronal activity lead to spatially restricted increases in blood flow[128]. This hemodynamic response, termed functional hyperemia, supplies active neurons with needed O_2 and nutrients. Previous work using laser Doppler flowmetry and other techniques[109] has shown that global stimulation of the retina results in global increases in retinal blood flow. In addition, an fMRI study has demonstrated that when one-half of the retina is stimulated with light, blood flow increases in that half, but not the other half of the retina[129]. However, fMRI does not currently have the resolution to accurately determine the spatial extent of the functional hyperemia response in the retina. Laser speckle flowmetry, in contrast, is ideally suited to mapping the spatial extent of blood flow increases evoked by focal stimulation[105, 119].

We describe in this report methods for successfully combining LSF and laser scanning confocal microscopy to monitor blood flow in the retina of the anesthetized rat. With this combined imaging system, we use confocal microscopy to stimulate photoreceptors in restricted retinal regions while simultaneously monitoring arteriole diameter with confocal line scans. At the same time, we use LSF to visualize spatial patterns of blood flow changes. We find that, as in the brain, focal stimulation of retinal photoreceptors does indeed produce localized increases in blood flow in the retinal circulation. Spatial patterns of functional hyperemia responses suggest that blood flow is regulated primarily by first and second order arterioles in the retina, but not by capillaries or venules.

Results

Simultaneous confocal and LSF imaging of the retina

We imaged the retina through the cornea and lens using an upright microscope though which confocal and laser speckle images were obtained simultaneously. The refractive properties of the cornea were neutralized with a contact lens placed between the eye and the microscope objective lens (Fig. 2.2A). For LSF, the retina was illuminated with 808 nm infrared light (Fig. 2.2B). This wavelength is well outside the absorption range of photoreceptor photopigments[108]. Thus, retinal photoreceptors and neurons were not stimulated by the LSF illumination light.

Arterioles and venules, which radiate from the optic disc, can be visualized simultaneously by confocal microscopy and LSF. This is illustrated in Fig. 3.1, where a

confocal image of retinal vessels is shown in Fig. 3.1A, a raw laser speckle image acquired simultaneously in Fig. 3.1B, a computed laser speckle contrast image in Fig. 3.1C and a computed blood velocity image in Fig. 3.1D. In the confocal image (Fig. 3.1A), primary arterioles and venules, filled with fluorescent dye, radiate from the optic disc at the bottom left. Arterioles can be distinguished from venules by their smaller diameter. Secondary and tertiary arterioles, branching from the primary vessels, are clearly seen in this image, as are retinal capillaries. In the raw speckle image (Fig. 3.1B), the larger vessels are seen as regions of reduced speckle contrast. They appear smoother than surrounding retinal areas, which are more speckled. When a speckle contrast image (Fig. 3.1C) is computed from the raw image, the larger vessels appear darker. This is because blood is flowing more rapidly through the larger vessels, resulting in blurring of the speckles and lowering of the speckle contrast. Computed speckle contrast (Chapter 2, Eq. 1) is invariant with incident illumination. Thus, the intensity of the speckle contrast image (excluding the major vessels) is relatively uniform, even though the intensity of the raw speckle image (Fig. 3.1B) varies greatly. When a blood velocity image (Fig. 3.1D) is computed from the speckle contrast image, vessels with high blood velocity appear brighter. Blood velocity is roughly proportional to pixel intensity in this image and is greatest in the primary arterioles and venules.

Illumination of the retina

The LSF in the retina has previously been achieved using a custom fundus camera that allows on-axis illumination of coherent light that passes through the cornea and lens[122]. However, when using an upright microscope to obtain simultaneous LSF and confocal images, on-axis illumination is difficult to implement in practice. Reflection of the coherent light off of the microscope lenses and the contact lens produces strong interference patterns which obscure portions of the LSF images.

Instead of using on-axis illumination, we have employed an off-axis method of illumination. Light from an 808 nm laser diode is directed through an optical fiber and onto the sclera at the appropriate position and angle to illuminate the retinal area being imaged (Fig. 2.2B). Sufficient light passes through the sclera and the retinal pigment epithelium to illuminate the retina. This trans-scleral illumination pathway is aided by the

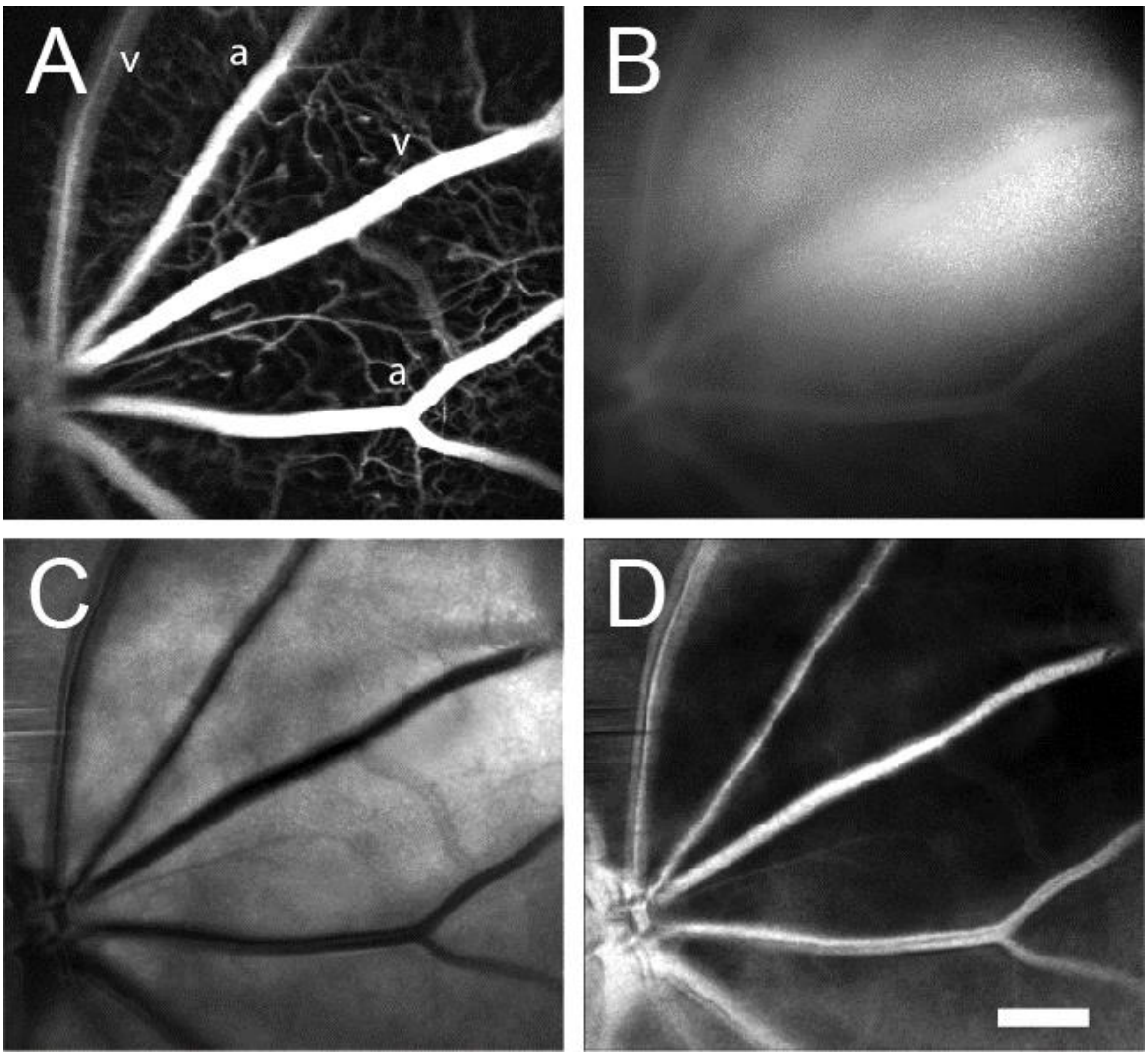

Figure 3.1. Laser speckle flowmetry of retinal blood vessels. (A) Confocal image of retinal blood vessels labeled with dextran-fluorescein. Primary arterioles and venules are seen radiating from the optic disc (at the lower left). **(B)** Raw speckle image acquired simultaneously from the same retina as **(A)**. Note that there is less speckling in the regions corresponding to the major vessels. **(C)** Speckle contrast image calculated from **(B)**. Dark lines indicate regions of reduced speckle contrast, generated by blood flowing rapidly through the primary retinal vessels. **(D)** Blood velocity image calculated from **(C)**. The brighter areas indicate greater blood velocity. In this and subsequent figures, primary arterioles and venules are labeled “a” and “v,” respectively. Scale bar for all panels, 250 μm.

use of infrared light, which passes through tissue more easily than does visible light. Depending on the precise position of the optical fiber illuminating the globe, either the retinal vasculature or the choroidal circulation is imaged. When the optical fiber is positioned 1–2 mm posterior to the limbus, the retinal circulation is visualized (Fig. 3.2A). The pattern of arterioles and venules corresponds to the fluorescence confocal image of the fluorescein-filled vessels (Fig. 3.2B). In some preparations, indistinct splotches, as well as the retinal vessels, are seen in speckle contrast and blood velocity images (Fig. 3.2A, arrowheads). These splotches are out of focus choroidal vessels. As the focus is shifted to the plane of the choroid and the end of the illuminating fiber is moved towards the posterior pole of the globe, the choroidal circulation becomes more distinct (Fig. 3.2C). The splotches seen in images of the retinal vessels correspond to the larger choroidal vessels (Fig. 3.2C, arrowheads). Although LSF images of choroidal vessels are of reduced quality, one must bear in mind that the vessels are imaged through 350 μm of tissue and a heavily pigmented layer, the retinal pigment epithelium. The size and branching patterns of the choroidal vessels imaged with LSF resemble those seen in corrosion casts of the choroidal vasculature (Fig. 3.2D).

Light-evoked changes in arteriole diameter

We monitored light-evoked changes in retinal circulation using both confocal microscopy and LSF. Retinal arterioles dilate in response to light stimulation[109]. This dilation can be quantified with confocal line scans. A line oriented perpendicular to an arteriole (Fig. 3.3A, yellow line) is repeatedly scanned for the duration of a trial. The resulting line scan image (Fig. 3.3B) displays the vessel diameter as a function of time. When retinal photoreceptors are stimulated (Fig. 3.3B, white bar), the vessel dilates. A plot of vessel diameter vs. time (Fig. 3.3D, trace 2) shows that light evokes a rapid increase in vessel diameter with a latency of approximately 1 s. Typically, a flickering light evoked a biphasic response consisting of a transient dilation lasting around 5 s followed by a sustained increase in vessel diameter. In a series of trials, vessel dilation averaged 8.87 ± 0.71% (S.E.M.; n = 60, six animals) of baseline diameter. Latency to the onset of dilation (time to 50% peak amplitude) was 1.51 ± 0.06 s (n = 52, six animals).

Changes in blood velocity were monitored simultaneously with vessel diameter using LSF. Hemodynamic responses were analyzed by calculating blood velocity images from

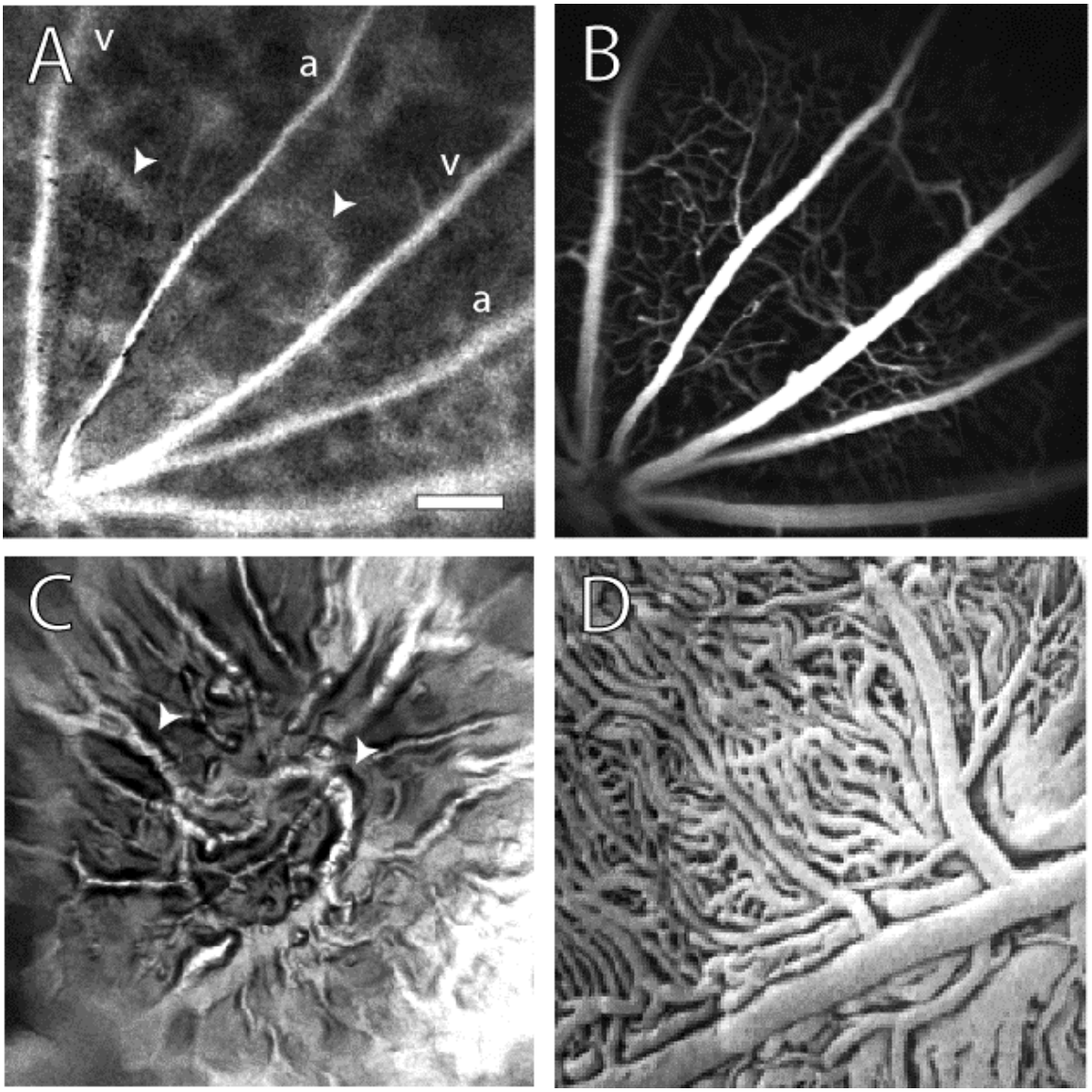

Figure 3.2. Laser speckle flowmetry of the retinal and choroidal vasculature. (A) A blood velocity image of retinal vessels. In addition to the primary arterioles and venules, indistinct splotches (arrowheads), which are generated by choroidal vessels, are seen. **(B)** Confocal image of the retinal vasculature from the same retinal region as **(A)**. **(C)** A blood velocity image of choroidal vessels in the same preparation as **(A)** and **(B)**. The image was obtained by adjusting the focal plane of the microscope and moving the illuminating optical fiber toward the posterior pole of the globe. The splotches visible in **(A)** correspond to major choroidal vessels (arrowheads) visible in **(C)**. **(D)** A corrosion cast of the choroidal vasculature of the rat, reproduced at the same magnification as the other panels. Note that the size and branching patterns of the vessels are similar to those in **(C)**. From [130], used with permission. Scale bar for all panels, 250 μm.

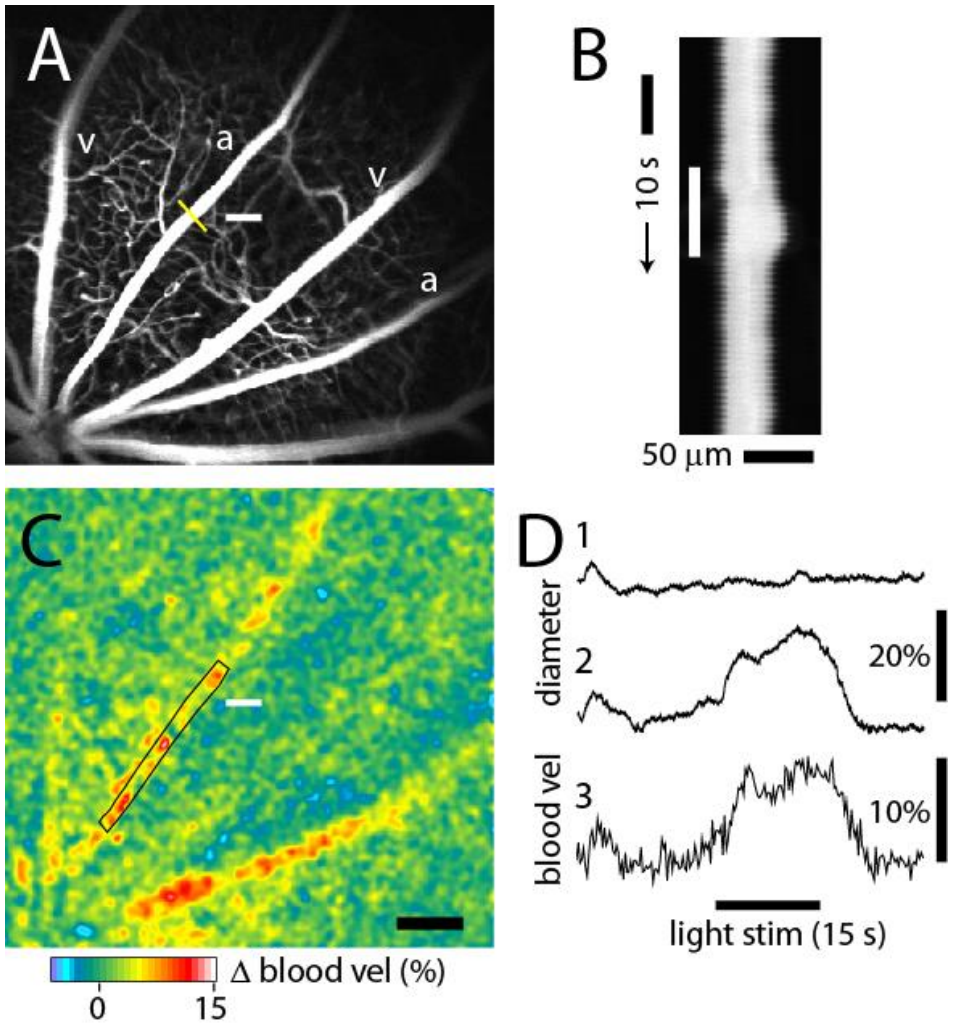

Figure 3.3. Light-evoked changes in retinal blood flow measured with confocal microscopy and LSF. (A) Confocal image of retinal vessels. The diameter of the upper arteriole was measured with confocal line scans (yellow line). The nearby white bar indicates the location of the flickering light stimulus in panels **(A)** and **(C)**. Scale bar for panels **(A)** and **(C)**, 250 µm. **(B)** Line scan image obtained from the arteriole in **(A)**. Distance [across the yellow line in **(A)**] is plotted as a function of time. A flickering light [white bar in **(B)**] evokes vessel dilation, indicated by the widening of the vessel cross section. The uneven edges of the vessel are caused by a respiratory movement artifact. **(C)** Blood velocity ratio image, showing the light-evoked change in velocity, calculated at 2–5 s after onset of the stimulus. The flickering light evoked large blood velocity increases in the two primary arterioles and smaller increases in the venules. **(D)** Time course of the light-evoked responses. (Trace 1) Change in arteriole diameter [measured at the yellow line in **(A)**] evoked by the onset of the 488 nm line scan excitation light, at the beginning of the trace. The flickering light stimulus was not turned on. The small response decayed within 10 s. (Trace 2) The same conditions as trace 1, except that the flickering light stimulus (black bar at bottom) was turned on. (Trace 3) change in blood velocity within the same arteriole, measured in the rectangular region indicated in **(C)**. Changes in light-evoked arteriole diameter and blood velocity were similar.

raw speckle images using equations 1 and 2 (Chapter 2). Changes in blood velocity were visualized by calculating blood velocity ratio images. Averaged velocity images obtained during the transient phase of the light response (2–5 s following stimulus onset) were divided by the averaged images obtained prior to stimulation. Six to 15 ratio images from sequential trials were averaged together to improve signal to noise. In these averaged pseudocolor ratio images, increased blood velocity is indicated by yellows, reds and white. The velocity ratio image for the trial illustrated in Fig. 3.3C, shows a prominent light-evoked increase in blood velocity in the primary arteriole adjacent to the stimulus as well as in a neighboring primary arteriole. Smaller velocity increases are seen in the primary venules. The time course of velocity within one of the arterioles (measured within the boxed area in Fig. 3.3C) is illustrated in Fig. 3.3D, trace 3. It has a similar time course to the dilation measured in the same vessel (Fig. 3.3D, trace 2).

Line scan measurements of arteriole diameter were made using 488 nm light, which stimulates retinal photoreceptors as well as exciting the dye used to image vessels. Although the intensity of the 488 nm light was far dimmer (typically 400-fold) than the 559 nm light used to stimulate retinal photoreceptors, onset of the line scan light did, in many trials, evoke a vascular response. However, as shown in Fig. 3.3D, both the increase in vessel diameter (trace 2) and the increase in blood velocity (trace 3) evoked by the onset of the line scan light were substantially smaller than the responses evoked by the 559 nm flickering stimulus. In addition, the response to the onset of the line scan light decayed rapidly (Fig. 3.3D, trace 1), well before the flickering stimulus was turned on. It should be noted that the 488 nm light was not turned on when only blood velocity, and not vessel diameter, was monitored (Fig. 3.4).

Light-evoked changes in blood flow

Increases in blood flow evoked by retinal stimulation have been characterized using a number of techniques[109]. However, the spatial extent of these increases has not previously been determined. It is not known, for instance, whether a spatially restricted light stimulus will evoke a localized increase in blood flow or whether the increase will spread far beyond the illuminated region.

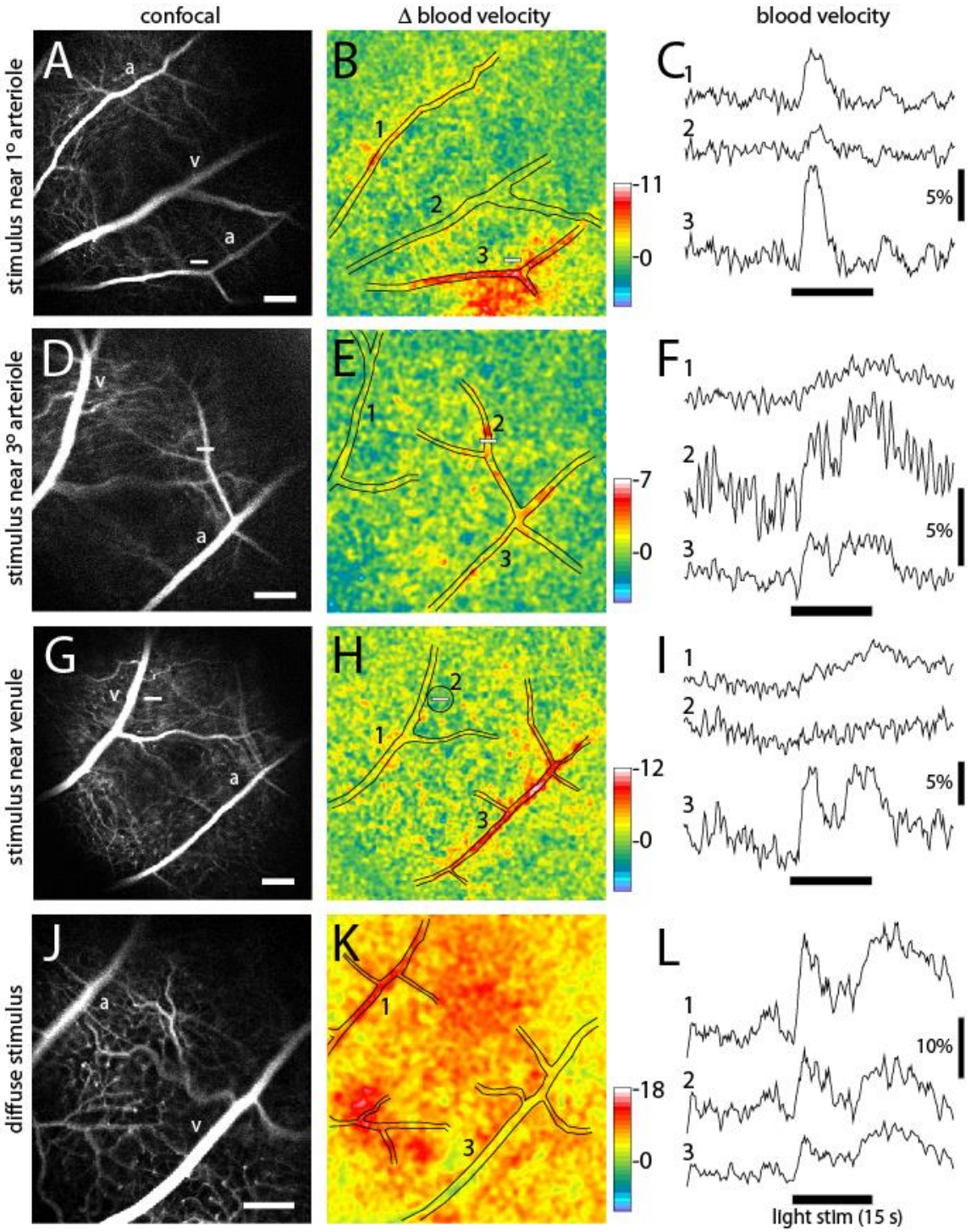

Figure 3.4. Blood velocity increases evoked by focal and diffuse light stimulation. Each row in the figure represents a different stimulus condition. Top three rows, the retina was stimulated with a focal, 15 s flickering light. Bottom row, the retina was stimulated with a diffuse 15 s flickering light. The left panels of each row show confocal images of the retina. Scale bars (at the bottom right of each panel), 250 μm. The middle

(Figure 3.4, cont.) panels show blood velocity ratio images for the same retinal regions. The pseudocolor images show the change in blood velocity at 2–5 s after stimulus onset and the pseudocolor scale bars indicates Δ velocity in percent. The locations of the large vessels are indicated by black lines. The small white bars in the left and middle panels indicate the locations of the focal stimulus. The right panels show the time course of blood velocity changes evoked by the light stimulus (black bars below the traces) for selected retinal regions. The region where each measurement was made is indicated by the numbers in the middle panels. Except when otherwise noted, blood velocity was measured within arterioles or venules. **(A–C)** The retina was stimulated near a branch point of first and second order arterioles. Blood velocity was measured in a non-stimulated arteriole (1), a venule (2), and the stimulated arteriole (3). Increased blood velocity was greatest within and in the regions immediately surrounding the stimulated arteriole. **(D–F)** The stimulus was near a third order arteriole. Blood velocity was measured in a venule (1), the stimulated third order arteriole (2), and the upstream first order arteriole (3). Increased blood velocity was greatest within the stimulated third order arteriole. **(G–I)** The stimulus was in a capillary bed, near a first order venule. Blood velocity was measured in the stimulated venule (1), a 200 μm diameter region surrounding the stimulus (2), and a distant arteriole (3). Increased blood velocity was small in the stimulated region and nearby venule but much larger in the arteriole. **(J–L)** The retina was stimulated uniformly by a diffuse light. Blood velocity was measured in an arteriole (1), across the entire imaged region of the retina (2), and a venule (3). Increased blood velocity was greatest in the primary arterioles and in regions supplied by arteriole branches.We have now characterized retinal blood flow responses to focal stimulation using a combination of LSF and confocal microscopy. We stimulated retinal photoreceptors with a 559 nm, 12 Hz flickering light generated by the confocal microscope. This stimulus illuminated a 135 × 20 μm region on the retinal surface (see Chapter 2). Changes in blood velocity evoked by this stimulus were monitored with LSF using 808 nm illumination.

We found that the spatial pattern of blood velocity increase evoked by this focal stimulus varied depending on the location of the stimulus relative to retinal arterioles and venules. When the stimulus was near a primary arteriole, increased blood velocity was greatest in that arteriole and in the region immediately surrounding the vessel (Fig. 3.4B). In many cases, other nearby primary arterioles also showed large velocity increases (Figs. 3.3C and 3.4B). The time course and amplitude of the velocity increase was calculated for regions corresponding to the stimulated primary arteriole and nearby arterioles and venules. Light-evoked velocity increases in the arterioles and venules typically had similar time courses (Fig. 3.4C), but the velocity increases in the arterioles were larger than were the increases in the venules (Fig. 3.5). The peak velocity increase in the stimulated primary arteriole averaged 7.60 ± 0.83% (*n* = 10, seven animals) and had a latency of 1.49 ± 0.12 s (*n* = 9, six animals). The amplitude of

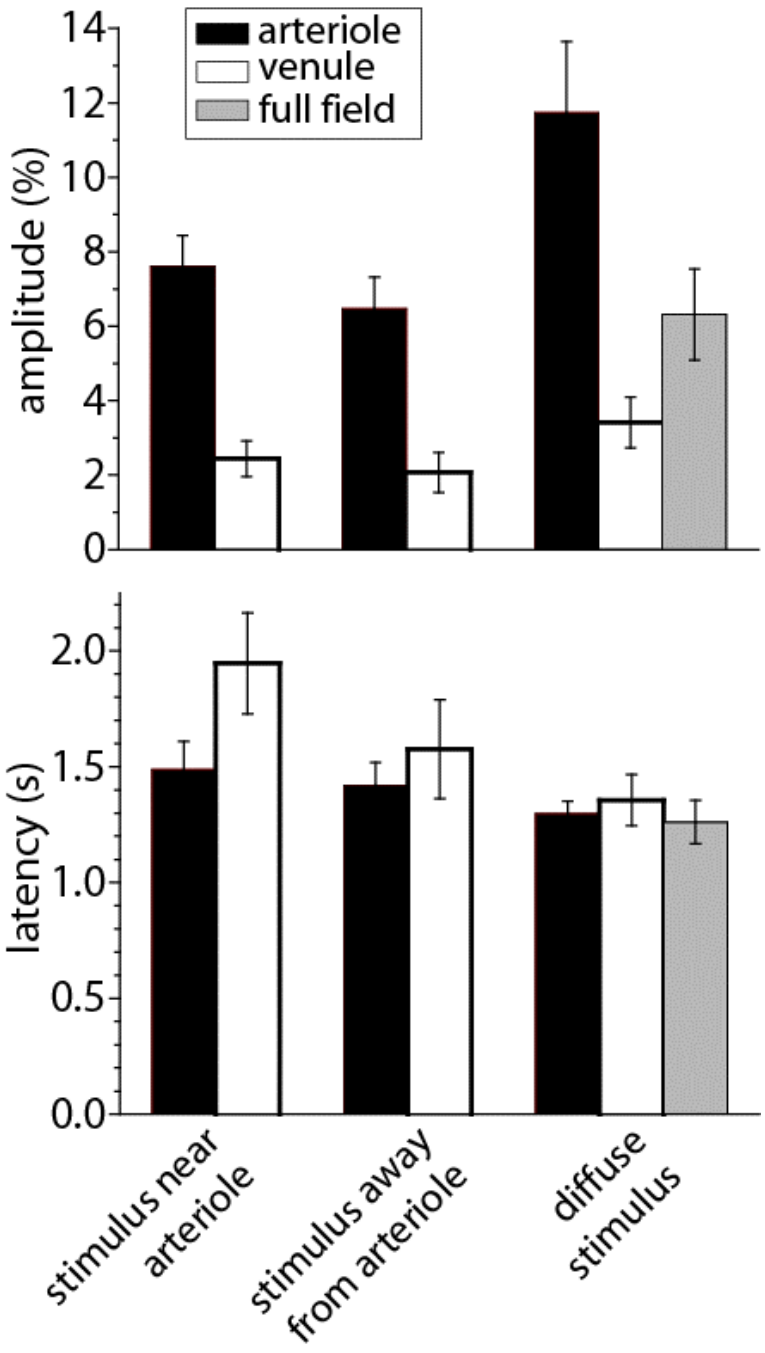

Figure 3.5. Amplitude and latency of blood velocity increases measured with LSF. Shown are mean response amplitude (peak change in blood velocity) and latency (time to 50% peak amplitude) for responses evoked under three different stimulus conditions: a focal stimulus near a primary arteriole, a focal stimulus far from 1°, 2°, or 3° arterioles, and a diffuse stimulus. Blood velocity was measured within primary arterioles (back bars), within primary venules (open bars), and, for diffuse stimulation, over the entire visible retina (gray bars). Error bars, S.E.M.

the velocity increase in the adjacent primary venule was smaller, averaging 2.44 ± 0.48%, with a latency of 1.95 ± 0.22 s (*n* = 6, four animals).

When the focal stimulus was near a second or third order arteriole, increased blood velocity was seen within the stimulated vessel and in upstream arterioles serving the vessel (Fig. 3.4E). The time course of the velocity increase was similar in the stimulated vessel and in upstream vessels. However, the observed temporal similarity of these responses may be due to the fact that our sampling rate (4 Hz) was not fast enough to detect small changes in response latency. It should also be borne in mind that when an increase in blood velocity is observed within a vessel, that increase could be due to active dilation of that vessel or to dilation of upstream arterioles, causing an increase in the pressure head to the vessel.

Blood velocity increases were somewhat smaller when the focal stimulus was distant from first, second, and third order arterioles (Figs. 3.4G and 3.5). In these cases, the largest velocity increases were seen in primary arterioles, even though they were some distance from the stimulus (Figs. 3.4H,I, trace 3). Responses were smaller in venules and in regions near the stimulus (Figs. 3.4H,I, traces 1 and 2). Peak blood velocity increases in the primary arteriole nearest to the stimulus averaged 6.47 ± 0.85% (*n* = 10, seven animals) and had a latency of 1.42 ± 0.10 s (*n* = 10, seven animals). Responses in the nearest primary venule averaged 2.07 ± 0.54% (*n* = 10, seven animals) and had a latency of 1.58 ± 0.21 s (*n* = 8, six animals). Responses averaged 2.08 ± 0.59% (*n* = 10, seven animals) and had a latency of 1.22 ± 0.21 s (*n* = 5, five animals) in a region 200 μm in diameter centered on the stimulus. We also measured the amplitude of blood velocity increase in an annular region 200–400 μm from the stimulus to determine whether the local response was restricted to the area of stimulation. The velocity increase in this annular region was 2.25 ± 0.60% (*n* = 10, seven animals), not significantly different from the response in the 200 μm diameter region centered on the stimulus.

Activation of a local region of the cerebral cortex sometimes evokes decreased blood flow in regions distant from the central region of increased blood flow[131, 132]. In our retinal experiments, we never observed a consistent decrease in blood velocity in response to focal light stimulation, regardless of the location of the stimulus. However, such a decrease could have occurred outside the field of view of our imaging system.

A diffuse flickering white light also evoked increased retinal blood velocity. As expected, blood velocity increases were more uniformly distributed across the retina (Fig. 3.4K) than were increases evoked by focal stimulation. Velocity increases were larger in some retinal regions than others. These regions were generally associated with second and third order arterioles (Fig. 3.4K). Velocity increases were greatest in primary arterioles (11.74 ± 1.91%; latency; 1.30 ± 0.05 s, *n* = 8, five animals; Fig. 3.5) as well as in regions near primary and secondary arterioles. Increases were substantially smaller in primary venules (3.41 ± 0.68%, *n* = 8, five animals; latency; 1.36 ± 0.11 s, *n* = 6, four animals). Blood velocity increases averaged over the entire viewable retina equaled 6.31 ± 1.23% (*n* = 8, five animals; latency; 1.26 ± 0.09 s, *n* = 7, five animals) (Fig. 3.4L, trace 2).

Discussion

We have described methods for combining LSF and laser scanning confocal microscopy to monitor blood flow in the retina. Using this combined imaging system, blood velocity changes were measured with LSF and arteriole diameter monitored with confocal line scans while retinal photoreceptors were stimulated by modulating the laser light from the secondary scanner of the confocal microscope. In contrast to other methods of measuring blood flow, LSF has the distinct advantage of permitting blood velocity to be monitored with high spatial and temporal resolution.

We illuminated the retina for LSF with 808 nm light delivered through an optical fiber pressed against the sclera. This method has several advantages. First, photoreceptors are largely insensitive to this infrared wavelength. Thus, retinal blood flow can be monitored without stimulating retinal neurons. Second, either the retinal vasculature or the choroidal circulation can be imaged with LSF, depending on the position of the illuminating optical fiber. Although LSF has previously been used to monitor choroidal blood flow in patients with polypoidal choroidal vasculopathy[127] and flow in the sub-foveal region of healthy subjects[133], our work is, to our knowledge, the first to image blood flow in an extended network of choroidal vessels in the healthy eye. This technique may prove useful in future studies of the regulation of choroid blood flow under normal and pathological conditions.

Many previous studies have characterized retinal blood flow changes evoked by light stimulation[109]. However, this is the first study to evaluate the spatial distribution of blood flow increases evoked by focal stimulation. We found that focal retinal stimulation evoked local increases in blood flow. This demonstrates that the retina has the ability to control blood flow at a local level. As in the brain, local control of blood flow in the retina allows needed O_2 and nutrients to be supplied to active neurons efficiently, without increasing the supply to inactive retinal regions.

Activity-dependent increases in blood flow in the brain were first described well over a century ago[27, 28]. Yet, the identity of the vessels which mediate this functional hyperemia response remains in question. Earlier studies suggested that a large fraction of hemodynamic resistance in the brain lay within large cerebral arteries[134] or smaller, precapillary arterioles[135] and it was thought that dilation of these vessels was responsible for increased blood flow[136, 137]. More recently, it has been suggested that capillaries may contribute to the regulation of blood flow in the brain. A theoretical study suggested that up to 70% of the total hemodynamic resistance in the brain vasculature lies in the capillary bed[138]. In addition, pericytes, which control capillary diameter, have been shown to contract or relax in response to neurotransmitters and neuronal activity[139-141].

The LSF results presented here bear on this issue and suggest that in the retina, activity-dependent blood flow changes are controlled largely by arterioles and that capillaries contribute little to the response. If capillary dilation contributed to functional hyperemia, focal stimulation of a region devoid of arterioles would result in increased blood flow to that region. However, we found the opposite to be true. When the retina was stimulated near a primary venule or in a region distant from arterioles, little increase in blood velocity was seen in the stimulated region. Rather, blood velocity increases were largest in the arterioles serving the stimulated region. In addition, blood velocity increases in the stimulated region of the retina were no larger than in an annulus surrounding this region. These results suggest that capillaries do not actively dilate in response to local neuronal activity and that more distant arterioles mediate the functional hyperemia response. The results must be interpreted with caution, however, as our LSF technique may not be sensitive enough to detect small changes in blood velocity in the capillary bed.

Previous studies have demonstrated that local arteriole dilations can be propagated upstream, leading to the dilation of larger arterioles and arteries feeding the stimulated vessels[142, 143]. Our LSF results are consistent with this view. When a focal retinal stimulus was near a second or third order arteriole, increased retinal blood velocity was observed, not only near the stimulated arteriole, but also near the primary, upstream arteriole (Fig. 3.4E).

We found that light-evoked velocity increases in primary venules were smaller than those observed in primary arterioles. This result appears at first to be paradoxical, as all blood flowing into the retina through primary arterioles must exit the retina through the venules. We attribute this discrepancy to the fact that primary venules in the retina are significantly larger in diameter than primary arterioles. Thus, for the same increase in total blood flux, velocity would increase to a smaller extent in venules than in arterioles. The differences in observed velocity increases are also attributable to the different time courses of the responses in arterioles and venules. Blood velocity amplitudes were measured during the initial, transient phase of the response (2–5 s after stimulus onset) while, in some cases, responses in venules were larger during the sustained portion of the response (Fig. 3.4I, trace 1).

We believe that the combined use of LSF and confocal microscopy holds great promise for studying the regulation of blood flow, both in the normal retina and in the retina under pathological conditions. A few examples illustrate the potential of this preparation.

- Preliminary experiments from our laboratory demonstrate that retinal glial cells can be labeled with Ca^{2+} indicator dyes and filled with caged-Ca^{2+} compounds introduced into the vitreous humor through a hypodermic needle inserted through the sclera. Photolysis of caged-Ca^{2+} by short wavelength pulses delivered by a confocal microscope generate Ca^{2+} increases in the labeled glial cells. The role of glial cells in regulating retinal blood flow can be evaluated using this technique[21, 144].
- Preliminary studies show that ischemia can be produced in a restricted region of the retina by photothrombosis generated by confocal illumination and bleaching of a photo-labile dye, such as rose bengal[34]. The effect of the thrombolytic lesion on blood flow in the penumbra can then be studied with LSF.

- Preliminary experiments demonstrate that blood vessels and blood flow in the mouse retina can be imaged with the same LSF/confocal microscopy techniques we describe here for the rat.

The potential of this preparation for characterizing mechanisms mediating functional hyperemia in health and disease will be expanded tremendously with the use of transgenic mouse lines.

CHAPTER 4:
Assessment of glial function in the in vivo retina

Summary

Glial cells, traditionally viewed as passive elements in the CNS, are now known to have many essential functions. Many of these functions have been revealed by work on retinal glial cells. This work has been conducted almost exclusively on ex vivo preparations and it is essential that retinal glial cell functions be characterized in vivo as well. To this end, we describe an in vivo rat preparation to assess the functions of retinal glial cells. The retina of anesthetized, paralyzed rats is viewed with confocal microscopy and laser speckle flowmetry to monitor glial cell responses and retinal blood flow. Retinal glial cells are labeled with the Ca^{2+} indicator dye Oregon Green 488 BAPTA-1 and the caged Ca^{2+} compound NP-EGTA by injection of the compounds into the vitreous humor. Glial cells are stimulated by photolysis of caged Ca^{2+} and the activation state of the cells assessed by monitoring Ca^{2+} indicator dye fluorescence. We find that, as in the ex vivo retina, retinal glial cells in vivo generate both spontaneous and evoked intercellular Ca^{2+} waves. We also find that stimulation of glial cells leads to the dilation of neighboring retinal arterioles, supporting the hypothesis that glial cells regulate blood flow in the retina. This in vivo preparation holds great promise for assessing glial cell function in the healthy and pathological retina.

Introduction

The vertebrate retina is an easily accessible part of the CNS and has proved to be a valuable preparation for characterizing glial cell properties and functions. The mammalian retina possesses two types of macroglial cells: astrocytes, which are confined largely to the innermost retinal layer, and Müller cells, which are radial glial cells that span the entire thickness of the retina. In many respects, Müller cells function as astrocytes in those retinal layers where true astrocytes are absent[11].

Previous work, utilizing both isolated retinas and retinal slices, has revealed several important functions of retinal glial cells. Müller cells regulate extracellular K^+ levels[145]. When active neurons release K^+, Müller cells transfer this K^+ to the vitreous humor by the process of K^+ siphoning[20]. Müller cells also regulate glutamate levels through the

action of their high affinity glutamate transporter[146]. Müller cells are stimulated by neuronal activity, generating increases in intracellular Ca^{2+} in response to the release of neurotransmitters[147]. In turn, stimulated Müller cells release ATP, which modulates retinal activity by hyperpolarizing ganglion cells, the output neurons of the retina[15, 148].

Recently, we demonstrated that glial cells mediate functional hyperemia in the retina[21]. When retinal neurons are stimulated by light, retinal arterioles dilate, bringing additional O_2 and nutrients to the active neurons. This response is mediated in large part by retinal glia, which release vasoactive agents that dilate retinal arterioles[30]. Previously, glial cell control of arteriole diameter was characterized in the isolated retina[21, 149]. This preparation is useful for several reasons. Retinal neurons and glia can be patched in the isolated retina so that their membrane potential can be monitored and controlled. The diameter of retinal vessels can also be monitored with high precision and the retina easily perfused with drugs in this preparation. However, the isolated retina has significant disadvantages in studying mechanisms mediating functional hyperemia. Blood does not flow through vessels and vessels do not have normal tone in the isolated retina. These factors can dramatically alter vascular responses. In addition, O_2 and NO levels, which both influence functional hyperemia[21, 150], may not be normal in the isolated retina preparation.

In order to circumvent the problems associated with the isolated retina, we have developed an in vivo preparation to characterize the role of glial cells in mediating functional hyperemia in the retina. Retinal glial cells can be labeled with Ca^{2+} indicator dyes, allowing their physiological state to be monitored with florescence microscopy. They can also be filled with caged Ca^{2+} compounds so that they can be stimulated by short wavelength light pulses. Retinal blood flow can be monitored in the in vivo preparation with both confocal microscopy and laser speckle flowmetry (LSF)[102]. Thus, the role that glial cells play in regulating retinal blood flow can be characterized using this in vivo preparation. In this chapter, we describe materials and methods for conducting in vivo experiments to assess retinal glial cell function.

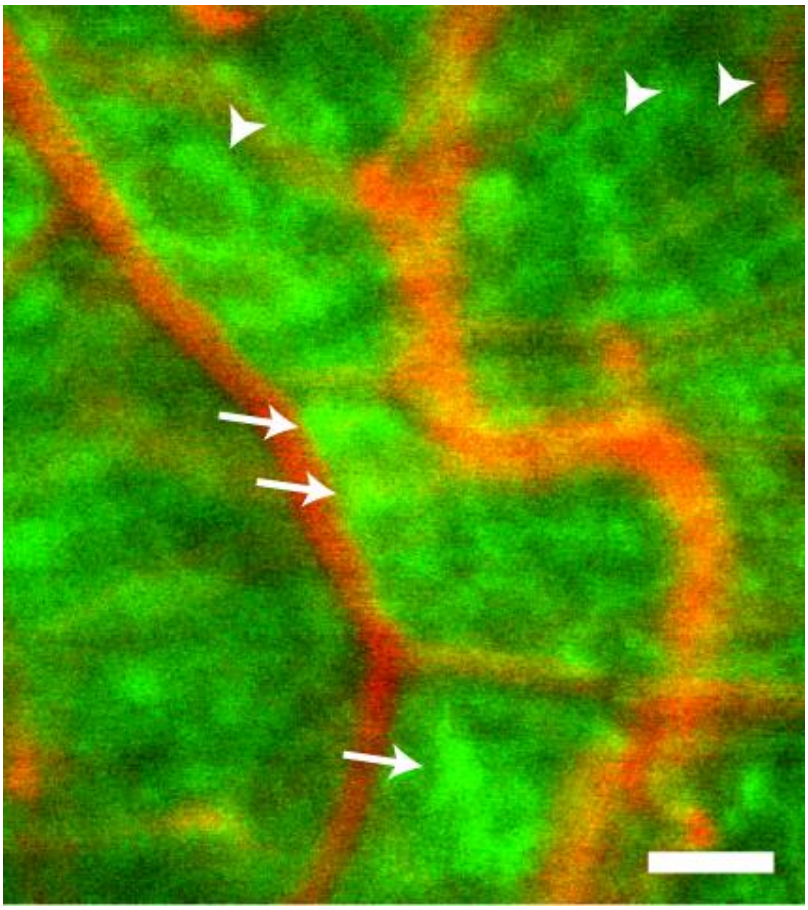

Figure 4.1. Glial cells of the retina. Glial cells (green) are labeled with the Ca^{2+} indicator dye Oregon Green 488 BAPTA-1 and vessels (orange) by intravenous ejection of dextran rhodamine B isothiocyanate in this confocal image of the retina. Several astrocytes (arrows) are visible. Most of the remaining labeled cells are Müller cells. Some Müller cells (arrowheads) are seen surrounding unlabeled somata of retinal ganglion cells. Scale bar, 100 μm.

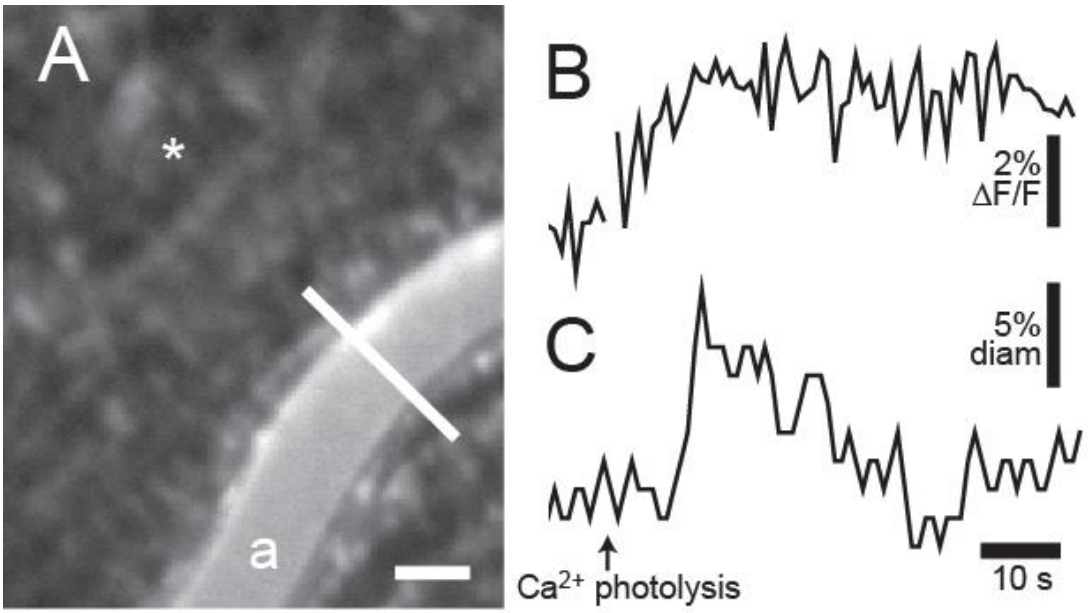

Figure 4.2. Glial-evoked dilation of retinal arteriole. (**A**) Confocal image of the retina, showing OGB-labeled glial cells and an arteriole (a) labeled with dextran rhodamine B isothiocyanate. The luminal diameter of the arteriole is monitored with confocal line scans (the white line across the vessel). Asterisk indicates the site of caged Ca^{2+} photolysis; scale bar, 25 μ m. (**B**) Glial Ca^{2+} fluorescence measured near the arteriole. Photolysis of caged Ca^{2+} evokes a glial Ca^{2+} increase. (**C**) The luminal diameter of the arteriole. Photolysis evokes a transient increase in vessel diameter.

Results

Assessing Glial Function

Previous work using the ex vivo isolated retina preparation demonstrated that retinal glial cells could communicate with each other through the generation of Ca^{2+} increases and intercellular Ca^{2+} waves. When a single glial cell is stimulated with a chemical, electrical, or mechanical stimulus, a Ca^{2+} increase is evoked in the stimulated cell. This Ca^{2+} increase propagates outward into neighboring astrocytes and Müller cells as a Ca^{2+} wave[110]. Spontaneously generated glial Ca^{2+} waves are also observed[151]. It was not known, however, whether these intercellular glial Ca^{2+} waves occur in vivo. The preparation described in this chapter has been employed to test whether glial Ca^{2+} increases and waves occur in vivo.

Glial Regulation of Blood Flow

1. Retinal glial cells are labeled with OGB and caged Ca^{2+}, and vessels labeled by intravenous injection of dextran rhodamine B isothiocyanate (Fig. 4.1).
2. Glial cells near a primary arteriole are stimulated by photolysis of caged Ca^{2+}, while the luminal diameter of the arteriole is monitored with confocal line scans. As described above, glial cell stimulation evokes Ca^{2+} increases in the stimulated cells. When glial cells adjacent to an arteriole are activated, an increase in arteriole diameter is evoked (see Fig. 4.2). These results demonstrate that glial cells can control vessel diameter in vivo and support the hypothesis that glial cells mediate functional hyperemia in the retina.

Glial Ca^{2+} Increases

1. Spontaneous Ca^{2+} waves. Retinal glial cells are labeled with OGB, and confocal images of the labeled glial cells are acquired at a frequency of ~1 Hz. Spontaneous increases in glial Ca^{2+} that propagate outward into adjacent glial cells at a velocity of ~22 μm/s are observed[151], demonstrating that spontaneous intercellular glial Ca^{2+} waves do occur in vivo.
2. Photolysis-evoked Ca^{2+} increases. Retinal glial cells are labeled with OGB and caged Ca^{2+}. Glial cells are stimulated by photolysis of caged Ca^{2+} while confocal images of the labeled glial cells are acquired at a frequency of ~1 Hz. Glial cell stimulation evokes Ca^{2+} increases in the stimulated cells. The increases in glial Ca^{2+} are proportional to the duration of the photolysis flash, with short flashes

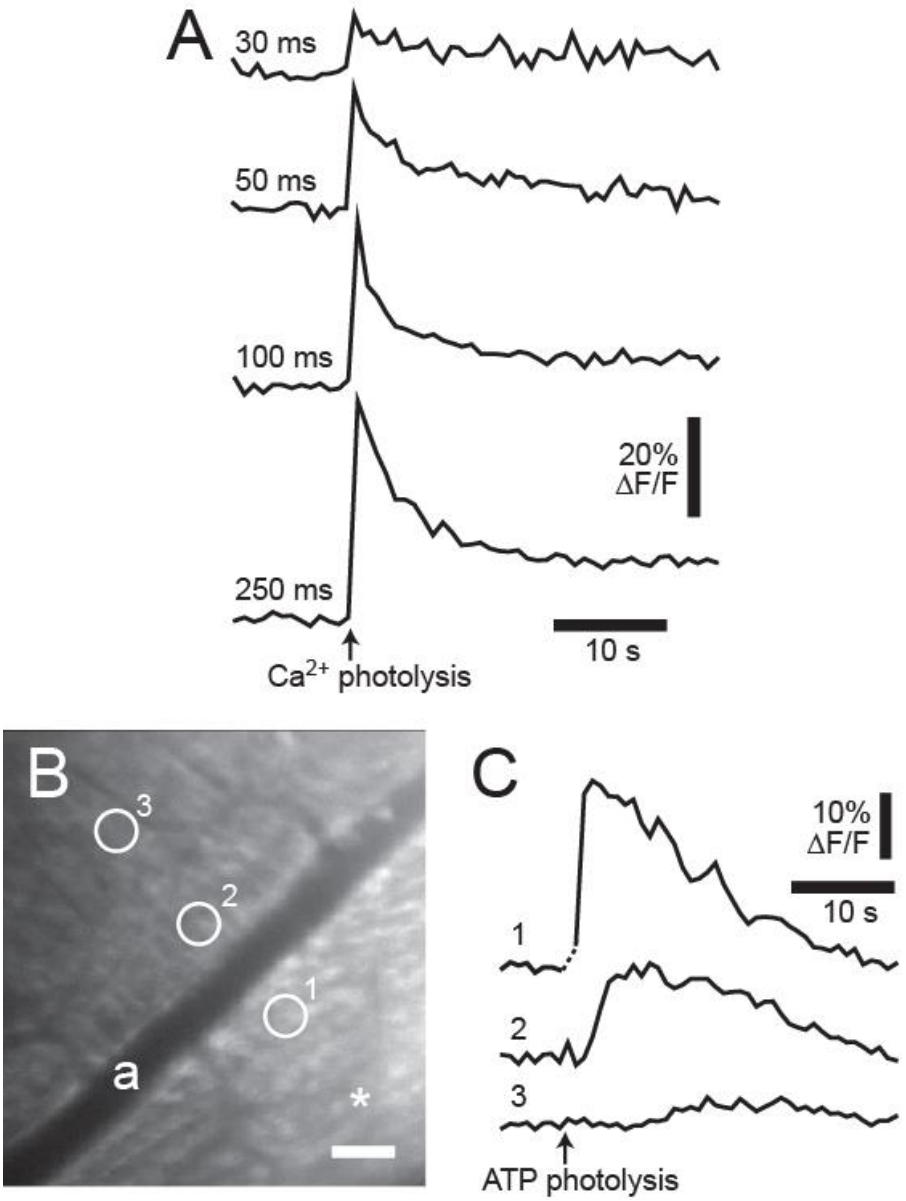

Figure 4.3. Glial cell Ca^{2+} increases. (**A**) Intracellular glial Ca^{2+} increases evoked by photolysis of caged Ca^{2+}. Photolysis evokes Ca^{2+} increases proportional to the duration of the photolysis flash. Numbers indicate flash duration for each trial. (**B, C**) Glial Ca^{2+} increases and a propagated Ca^{2+} wave evoked by photolysis of caged ATP. (**B**) A confocal image of the retina showing OGB-labeled glial cells. Asterisk indicates the site of caged ATP photolysis; scale bar, 50 μ m. (**C**) Stimulation of glial cells by photolysis of caged ATP in the vitreous humor evokes Ca^{2+} increases in the stimulated cells and initiates a propagated Ca^{2+} wave. Ca^{2+} is measured in the three regions indicated in (B).

3. evoking small, brief increases and longer flashes evoking larger, more prolonged increases (see Fig. 4.3A). In many trials, photolysis of caged Ca^{2+} triggers
4. propagated Ca^{2+} waves traveling through adjacent Müller cells and astrocytes. The results demonstrate that, as in the isolated retina[110, 116], photolysis of caged Ca^{2+} in vivo is effective in stimulating retinal glial cells and that glial cell stimulation leads to the initiation of intercellular glial Ca^{2+} waves.
5. ATP-evoked Ca^{2+} waves. Retinal glial cells are labeled with OGB. Glial cells are stimulated by photolysis of caged ATP in the vitreous humor while confocal images are acquired at a frequency of ~1 Hz. 10 µL of caged ATP solution (2 mM in saline) is injected into the vitreous humor near the retinal surface. The caged ATP is activated by brief (0.2–1 s), focused (5 µm diameter) flashes of 405 nm light. The released ATP stimulates retinal glial cells, evoking large increases in Ca^{2+} in the stimulated cells and initiating propagated Ca^{2+} waves (see Fig. 4.35B, C).

The results demonstrate that, as in the isolated retina[116], activation of purinergic receptors evokes Ca^{2+} increases in retinal glial cells in vivo. Activation of retinal neurons by photic stimuli results in the dilation of retinal arterioles and increases in retinal blood flow[109]. This response, termed functional hyperemia, brings added O_2 and glucose to the active neurons. Although the cellular mechanisms that mediate functional hyperemia remain controversial, recent evidence indicates that glial cells play a principal role in coupling neuronal activity to vessel dilation[30]. We have shown that in the isolated retina, stimulation of glial cells results in the dilation of adjacent arterioles[21]. It is not known, however, whether glial stimulation in vivo leads to vessel dilation in the retina. The preparation described in this chapter has been employed to test whether glial cells regulate the diameter of retinal vessels in vivo.

CHAPTER 5:
Ischemia-induced spreading depression in the in vivo retina

Summary

Cortical spreading depression (CSD) is a metabolically costly phenomenon that occurs in the injured brain and contributes to tissue damage. In the retina, spreading depression has only been studied in ex vivo, avascular preparations. Here, we report that spreading depression occurs in the in vivo rat retina in response to occlusion of retinal blood vessels. The properties of retinal spreading depression (RSD) and CSD are similar. RSD waves have a propagation velocity of 3.0 ± 0.1 mm/min and are associated with a negative shift in DC potential, a transient cessation of neuronal spiking, constriction of arterioles, and a drop in tissue O_2 tension. The frequency of wave generation is reduced by MK-801 and sumatriptan. As in the brain following ischemic stroke, RSD waves may occur in patients with branch retinal vein occlusion and related vascular disorders. Blocking RSD in these patients may reduce vision loss caused by vessel occlusion.

Introduction

Cortical spreading depression (CSD) was first described by Leão in the rabbit cortex[49] and has since been characterized extensively[53, 54]. Its hallmark feature is a wave of extreme cellular depolarization that spreads over the cortical surface at a velocity of ~3 mm/min. This wave is accompanied by large shifts in transcellular ion gradients, cell swelling, and increased extracellular concentrations of neurotransmitters, particularly glutamate[49, 53, 55]. CSD is characterized electrophysiologically by a negative shift in DC potential and a transient period of increased neuronal spiking followed by a cessation of neuronal activity that persists until ion gradients are reestablished[53]. K^+ and glutamate released from neurons are believed to overwhelm local glial K^+ buffering and transmitter uptake mechanisms to generate and propagate CSD[54, 72].

CSD results in a complex series of blood flow changes[54]. In its earliest phase, blood vessels constrict, mediated by the release of K^+ and vasoconstrictors from neurons and glia during wave propagation[54, 67, 68]. This initial drop in blood flow is followed by a period

of hyperemia that lasts for several minutes and then by a persistent oligemia lasting for over an hour after the CSD episode[65].

CSD can occur in both healthy and injured tissue. In the healthy brain, CSD is the mechanism that underlies migraine auras and their subsequent scotomas[51, 53]. The brain fully recovers from such CSD episodes without lasting consequences. However, in pathology, such as severe stroke, subarachnoid hemorrhage, or traumatic brain injury, CSD events are initiated at the borders of the injured tissue[47, 48, 52]. The combination of high extracellular levels of excitatory amino acids, increased metabolic demand, the long lasting oligemia induced by CSD waves results in excitotoxicity and metabolic supply-demand mismatch, ultimately leading to additional cell death and injury expansion[47, 60, 62, 152]. In subarachnoid hemorrhage patients, tens of CSD episodes are sometimes generated in the days following the initial ischemic insult, resulting in delayed neurological deficits corresponding with secondary ischemic infarcts[60].

Spreading depression can occur in the retina as well as the cortex[59, 70, 76]. However, retinal spreading depression (RSD) has previously been observed only in ex vivo preparations from species that have avascular retinas[70, 72-74]. Like CSD, RSD can be initiated experimentally by exogenous glutamate application[75], altering ion concentrations (elevating K^+ or lowering Cl^-)[72], by mechanical stimulation[59], or by traumatic injury[76]. Ex vivo RSD and CSD have similar propagation velocities and electrophysiological characteristics[77]. However, RSD has never been described in vivo and it has been questioned whether it may be an artifact of ex vivo preparations[54].
We now demonstrate for the first time that RSD occurs in vivo. RSD episodes are generated following the experimental occlusion of retinal vessels, suggesting that RSD may also occur in patients with branch retinal vein occlusion (BRVO) and related vascular disorders. RSD waves have similar properties as CSD waves and are accompanied by a series of blood flow changes that may contribute to tissue damage. We find that RSD can be blocked by several agents, including MK-801 and sumatriptan, suggesting a therapeutic strategy for reducing vision loss in BRVO patients.

Results

We investigated whether an ischemic insult in the retina evokes spreading depression, as it does in the cortex[53, 54]. A photothrombosis model of focal retinal ischemia was used

to generate blood clots in primary retinal arterioles and venules. Rose Bengal was injected i.v. and bleached with 559 nm light focused onto single vessels to form a thrombus. The intrinsic optical signal (IOS) of the retina was monitored at 405 nm with reflectance microscopy to detect RSD episodes while the Rose Bengal-filled vasculature was imaged with confocal microscopy. Concurrent laser speckle flowmetry permitted real-time visualization of blood flow changes to confirm blockage of blood vessels and to map regions of retinal ischemia.

Photothrombosis completely blocked blood flow in the treated vessels and reduced blood flow in the adjacent tissue (Fig. 5.1a & b). Confocal microscopy and laser speckle flowmetry confirmed that the occluded vessels remained blocked for > 60 min. Animals then recovered and retinas were harvested after a 2 week survival period. Retinal ganglion cells (RGCs) were labeled with an anti-Brn3a antibody. Low power confocal images show a clearly defined region devoid of RGCs which was centered on the occluded vessel (Fig. 5.1c). The absence of RGC labeling was due to a loss of cells rather than a loss of Brn3a immunoreactivity, as demonstrated by differential interference contrast microscopy images showing an absence of cells in the affected retinal region (Fig. 5.1d & e). No such loss of RGCs was observed when vessels were bleached in the absence of Rose Bengal.

Occlusion of blood vessels evokes retinal spreading depression

RSD waves were generated in every instance when a primary branch arteriole (n=15) or venule (n=3) was occluded (Fig. 5.2a & b). The properties of the RSD waves are detailed in Table 5.1. On average, 3.7 ± 0.6 waves were generated within the first hour following vessel occlusion, with few waves (0.2 ± 0.2) generated after this time. Latency to generation of the first wave following vessel occlusion was 7.9 ± 1.4 min. RSD waves had a propagation velocity of 3.0 ± 0.1 mm/min (n=58 waves, 15 rats), similar to that observed in CSD. The majority of RSD waves (81%) were initiated near the optic disc and propagated outward towards the retinal periphery. Occasionally (12.1%), waves were initiated at the periphery and propagated inwards towards the central retina. In a subset of these pheripherally-initiated episodes, the waves reversed direction and/or

Table 5.1. Properties of retinal spreading depression waves.

RSD Properties	Mean ± SEM (n rats)
Number of waves per animal following occlusion	
0-15 minutes	1.33 ± 0.21 (15)
16-30 minutes	1.47 ± 0.31 (15)
31-45 minutes	0.53 ± 0.40 (15)
46-60 minutes	0.33 ± 0.21 (15)
60+ minutes	0.20 ± 0.20 (15)
TOTAL	3.87 ± 0.70 (15)
Latency to first wave (sec)	475 ± 85 (15)
Propagation velocity (mm/min)	3.0 ± 0.1 (15)
Size (radius, µm)	1104 ± 41 (15)
Site of initiation	
Optic disc	47/58 (15)
Periphery	7/58 (15)
Bleach site	4/58 (15)
Arteriole constriction (µm)	4.7 ± 1.1 (5)
pO_2 decrease (mmHg)	11.7 ± 1.4 (5)

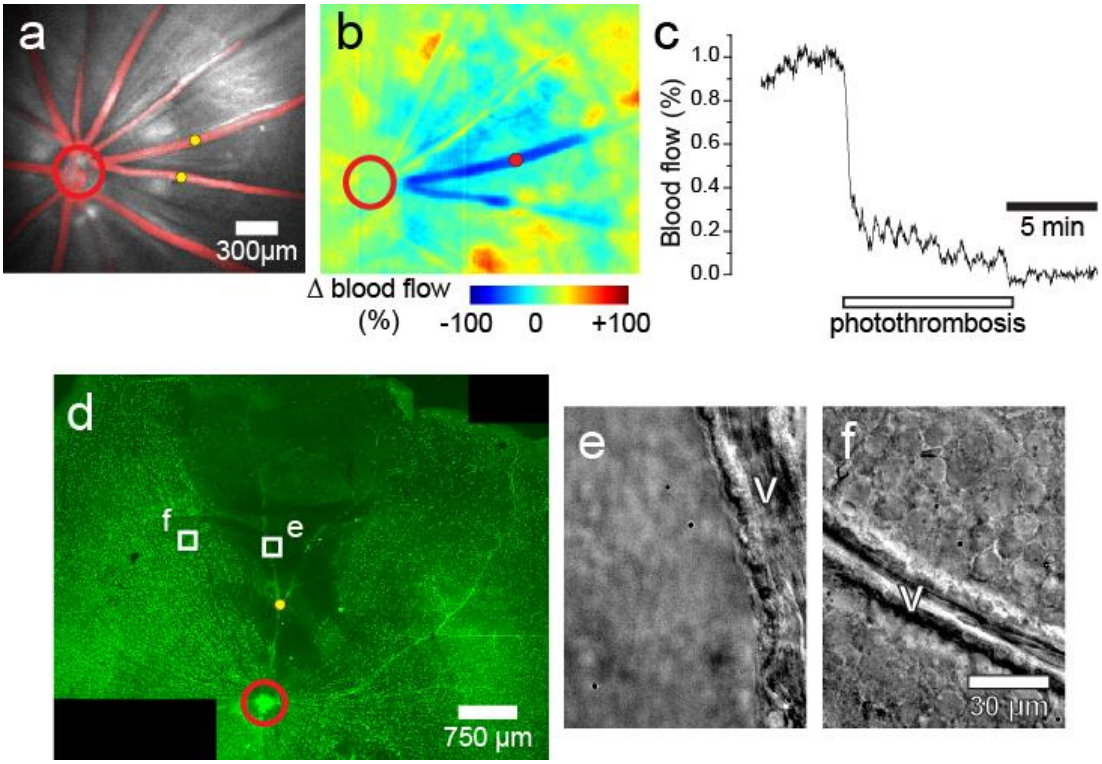

Figure 5.1. Photothrombosis model of branch retinal vessel occlusion. (**a**) Reflectance image of the retina with a superimposed confocal image of Rose Bengal-labeled blood vessels (red). Vessel occlusion was produced by photoactivation of Rose Bengal in two branches of a primary venule (yellow dots). Red circles in this and other panels indicate the optic disc. (**b**) Ratio laser speckle flowmetry image of the retina shown in **a**. Photothrombosis produced a complete block of blood flow in the two occluded vessels (dark blue) and a partial block of blood flow in the adjacent tissue (light blue). (**c**) Quantification of the relative blood flow decrease measured by laser speckle flowmetry. Blood flow, measured at the red dot in **b**, decreases to 0% by the end of the photothrombosis period. (**d**-**f**) Photothrombosis of a single arteriole produced large-scale loss of retinal ganglion cells (RGCs) in the region supplied by the vessel following a 2 week survival time. Immunohistochemical labeling of RGCs (**d**) reveals a complete absence of cells in the region supplied by the occluded vessel (yellow dot). Differential interference contrast microscopy demonstrates an absence of cells in the ischemic region (**e**), compared to a healthy region far from the thrombus (**f**). V, vessel.

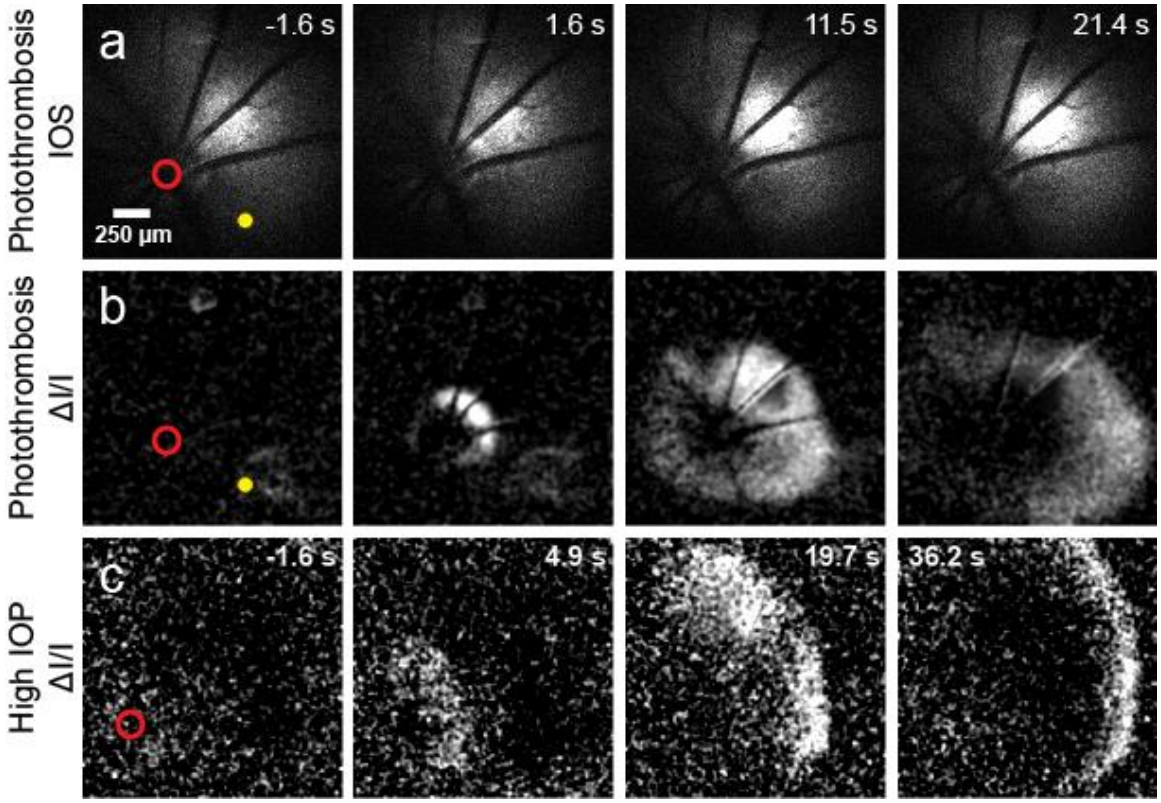

Figure 5.2. Retinal spreading depression occurs following vessel occlusion. (**a**) Intrinsic optical signal (IOS) images of a representative RSD event in response to focal thrombosis of an arteriole (yellow dot). Numbers in the upper right of each panel in this and other figures indicate time relative to RSD initiation. (**b**) Images from the series shown in **a** processed with each frame representing the Δ intensity/intensity (∆I/I) to better visualize the RSD wave front. Most RSD waves are initiated near the optic disc (red circle). (**c**) A RSD wave initiated following onset of global ischemia, produced by increasing intraocular pressure to 120 mmHg. The wave was initiated near the optic disc (red circle).

generated a secondary wave after reaching the optic disc and propagated outward again. This secondary wave always propagated into areas of the retina that had not sustained the initial wave. Rarely (6.9%), waves were initiated near the site of photothrombosis.

Accumulation of free radicals has been reported to initiate spreading depression in both the ex vivo retina[59, 70] and the cortex[153]. It is possible that the RSD waves we observed were initiated by this mechanism rather than by ischemia, as photothrombosis produces thrombi through free radical generation[59, 70]. If this were the case, then activating Rose Bengal in a retinal region containing capillaries rather than large vessels would also generate RSD. However, photothrombosis of capillaries produced no RSD events (n=3). Nor were RSD waves generated by photobleach illumination in the absence of Rose Bengal in the vasculature (n=6). In an additional control experiment, we tested whether RSD episodes were generated in a model of retinal ischemia where free radical production by photothrombosis was absent. Blood flow in the entire retinal circulation was blocked by raising intraocular pressure to ~120 mmHg. An RSD wave was generated within 1.5 - 2.3 min (n=3 waves in 3 animals) of blocking blood flow (Fig. 5.2C). Interestingly, in this global model of ischemia, only one RSD wave was generated per animal, rather than the multiple waves evoked by occlusion of a single branch vessel. However, if perfusion was reestablished by lowering intraocular pressure within a minute after an RSD wave occurred, additional waves could be evoked by subsequent increases in intraocular pressure. Together with the observation that RSD episodes are rarely initiated at the site of photothrombosis, these data strongly suggest that RSD is a response to the acute loss of vessel perfusion.

Electrophysiological properties of RSD

We characterized the electrophysiological properties of RSD in both the ex vivo rat eyecup and the in vivo rat preparation to determine whether it has the same electrophysiological characteristics as CSD. RSD waves were elicited in the eyecup by focal ejection of K^+ gluconate and were monitored by imaging IOS of the retina with reflectance microscopy. Concurrently, extracellular field recordings were made in the RGC layer. A negative shift in DC potential and a brief burst of RGC spiking followed by the silencing of activity was observed when the RSD wave front reached the recording pipette (Fig. 5.3a & b; n=3 rats). RSD waves were also evoked in the eyecup by oxygen

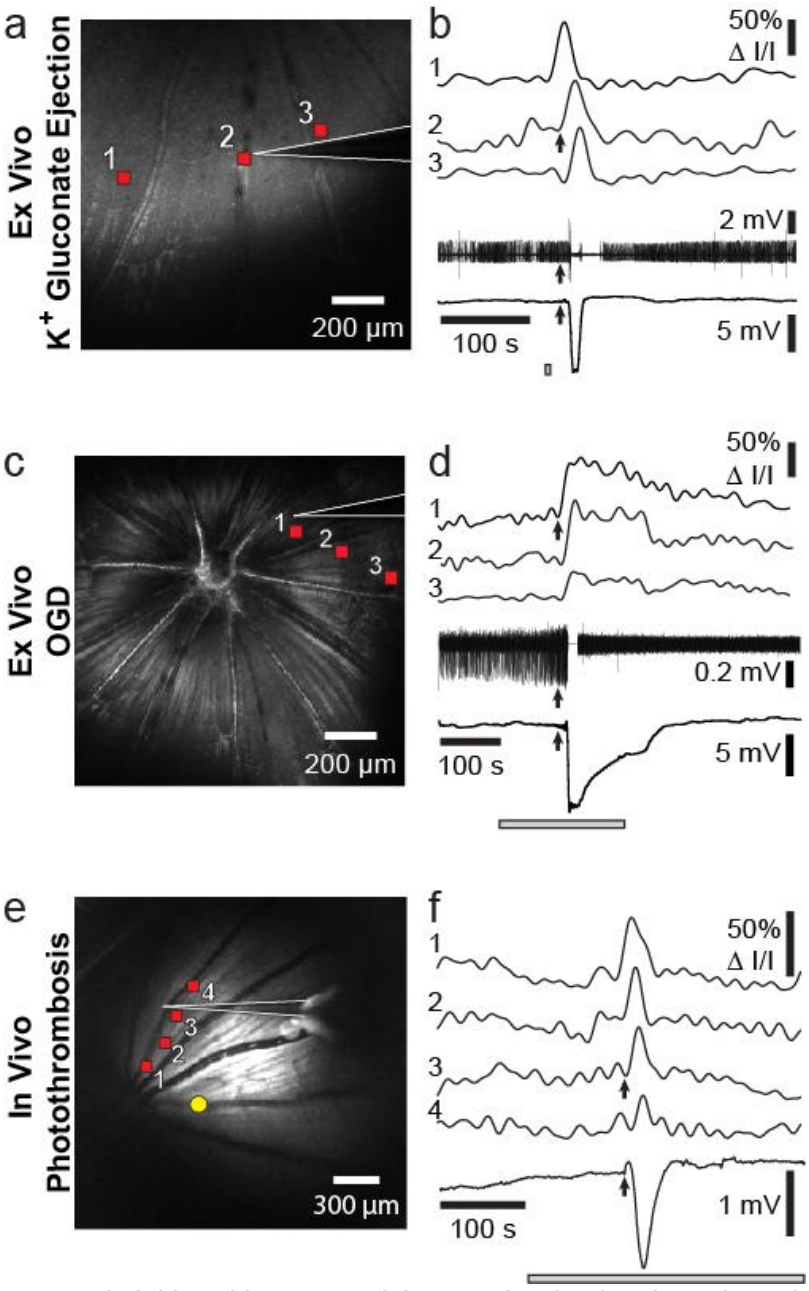

Figure 5.3. RSD waves have similar electrophysiological characteristics as CSD waves. Left panels show reflectance images of the retina and the recording pipette (white outlines). Right panels show IOSs of RSD waves (top traces) and electrophysiological responses (bottom traces). The IOS signals were recorded at the retinal locations indicated by the red squares in the left panels. Time course of the stimulus is indicated by the gray bars in the right panels. (**a** & **b**) A RSD wave in an eyecup was initiated by focal K^+ gluconate ejection (outside of the image in **a**). Spike activity of a RGC (2nd from bottom trace in **b**) and DC potential (bottom trace in **b**) are shown. Upon arrival of the RSD wave at the recording pipette (arrows in B) RGC spiking is briefly stopped and a negative DC potential is generated. (**c** & **d**). A RSD wave in the eyecup is initiated by oxygen/glucose deprivation (OGD). As in **b**, RGC activity is halted and a negative shift in DC potential is recorded upon arrival of the RSD wave at the recording pipette. The decrease in spike amplitude after the RSD wave is due to movement of the recording pipette. (**e** & **f**) A RSD wave is initiated in vivo by photothrombosis of an arteriole (yellow dot in E). Upon arrival of the RSD wave at the recording pipette (arrows in **f**) a negative DC potential is seen (bottom trace in **f**).

glucose deprivation (OGD), an ex vivo model of ischemia (n=3 rats). These RSD waves had similar electrophysiological properties as those observed in the K^+ gluconate model (Fig. 5.3C & D). Field potential recordings were also performed in vivo, with RSD waves evoked by photothrombosis of a primary branch vessel. As in the ex vivo experiments, a negative shift in DC potential was recorded as the RSD wave passed the recording pipette (Fig. 5.3e & f; n=3 rats). Together, these experiments demonstrate that the RSD waves observed in the retina have similar electrophysiological properties as CSD waves and that RSD waves are generated in the OGD model of ischemia.

Changes in blood flow associated with RSD

A series of blood flow changes are associated with CSD[54, 68, 154]. We used a number of techniques to determine whether similar blood flow changes are associated with RSD. Changes in the diameter of primary arterioles were monitored in vivo with confocal microscopy. A dramatic constriction of arterioles was observed as RSD waves passed the vessels (Fig. 5.4a & b). Arteriole constriction averaged 10.6 ± 1.8% (4.7 ± 1.1 µm; n=5 waves, 5 rats). Arteriole constriction recovered after 36 s. As described by the Hagen–Poiseuille fourth power relation, a constriction of 10.6% will result in a 36% decrease in blood flow.

Such a large drop in blood flow, coupled with the increased metabolic demand imposed by RSD, should lead to a decrease in O_2 partial pressure (pO_2). We tested this prediction by measuring pO_2 with an optical O_2 sensor at the surface of the retina. The sensor was positioned in a region far from the site of photothrombosis and outside the region directly affected by the thrombus, identified by laser speckle flowmetry. A rapid drop in pO_2 of 11.6 ± 1.4 mmHg (n=14 waves, 6 rats) was observed as the RSD wave passed the sensor (Fig. 5.4c & d). pO_2 decreases recovered slowly over 103 ± 10 s (n=14 waves, 6 rats) and generally returned to baseline or even exhibited an overshoot above baseline for RSD episodes that occurred shortly after thrombus formation. However, with subsequent RSD waves, baseline pO_2 dropped further and remained below pre-thrombus levels for the remainder of the monitoring session, in one case for over 60 min. These experiments demonstrate that RSD waves are accompanied by a transient drop in blood flow and a more prolonged decrease in retinal pO_2.

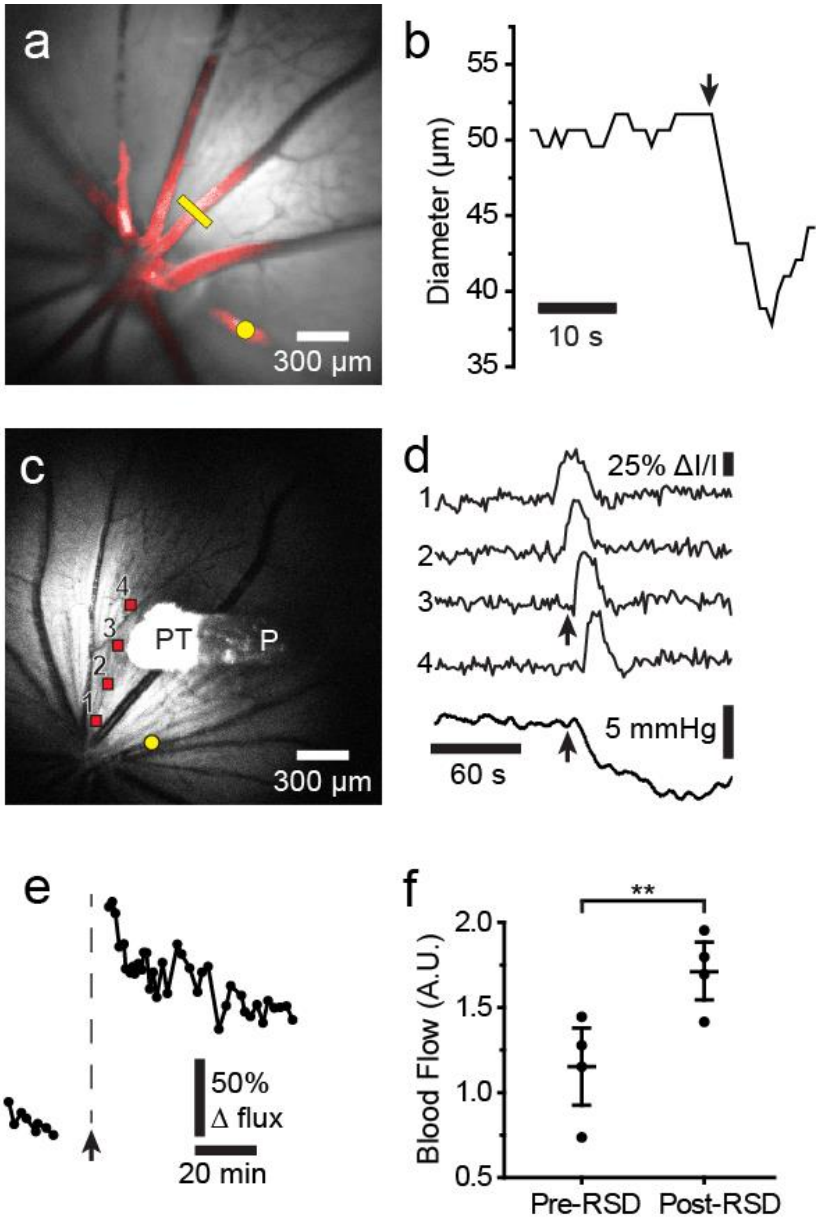

Figure 5.4. RSD-induced alterations in retinal blood flow and pO_2. (**a**) Reflectance image of the retina with a superimposed confocal image of Rose Bengal-labeled blood vessels (red). Photothrombosis of a primary arteriole (yellow dot) evoked a RSD wave. The diameter of a second arteriole was monitored with confocal line scans (yellow line). (**b**) Diameter of the arteriole indicated by the yellow line in **a**. A rapid 12% constriction of the vessel coincided with the arrival of the RSD wave (arrow). (**c**) Reflectance image of the retina, showing the O_2 probe (P) and the O_2-sensitive probe tip (PT). Photothrombosis of an arteriole (yellow dot) evoked a RSD wave. (**d**) IOSs (top four traces) show propagation of a RSD wave from the retina in C. The IOSs were recorded at the retinal positions indicated by the red squares in **c**. A large, rapid decrease in retinal pO_2 (bottom trace) occurs when the RSD wave reaches the O_2 probe (arrows). (**e**) Blood flow in a patent primary arteriole distant from the vessel occluded by photothrombosis, measured by monitoring red blood cell (RBC) flux. When the occlusion-evoked RSD wave reached the patent vessel (arrow), blood flow increased substantially. The blood flow increase decayed slowly over an hour. (**f**) Summary of blood flow changes induced by RSD, measured by monitoring RBC flux. Post-RSD flow represents the mean flow during the period 24-65 min following RSD wave generation. N=5 animals.

Longer-term changes in blood flow following a RSD episode were investigated by measuring the flux of labeled red blood cells as they passed through a primary arteriole that was not subjected to photothrombosis. Following the brief decrease in blood flow described above, there was a prolonged increase in flow which decayed slowly over several hours (Fig. 5.4e & f). We did not observe an oligemic phase, which is seen in CSD[54, 68].

Pharmacological block of RSD

BRVO and related vascular disorders are a leading cause of ischemic vision loss[5]. Our data suggests that RSD may accompany such disorders and contribute to tissue damage and vision loss in patients. Thus, it would be useful to identify drugs that block RSD. We found that the NMDA receptor antagonist MK-801, which blocks CSD[55, 155], significantly decreased the number of RSD events as well as the size and the velocity of the RSD waves evoked by photothrombosis (Fig. 5.5). A second NMDA antagonist, memantine, did not have a statistically significant effect on wave number, size, or velocity, but the data trended towards a reduction in these measures. Sumatriptan, a 5-HT(1D) agonist that has been shown to block RSD in the ex vivo retina[156], reduced the number RSD waves as well, but did not affect size and velocity (Fig. 5.5).

Discussion

The results of this study demonstrate, for the first time, that spreading depression can be generated in the in vivo retina. Multiple RSD waves were generated following photothrombosis occlusion of a primary retinal arteriole or venule. The RSD waves were not an artifact of the photothrombosis model of retinal ischemia, as RSD was also generated in vivo following global ischemia produced by an increase in intraocular pressure and in the eyecup following oxygen/glucose deprivation, an ex vivo model of ischemia. RSD waves had similar properties as CSD waves, including similar propagation velocities. RSD, as CSD, was associated with a change in the intrinsic optical signal of the tissue, a negative shift in DC potential, a transient increase followed by a longer silencing of neuronal spiking, a sequence of blood flow changes, and a decrease in tissue pO_2. Drugs that are effective in blocking CSD, including the NMDA antagonist MK-801 and the 5-HT(1D) agonist sumatriptan, were also effective in reducing the generation of RSD.

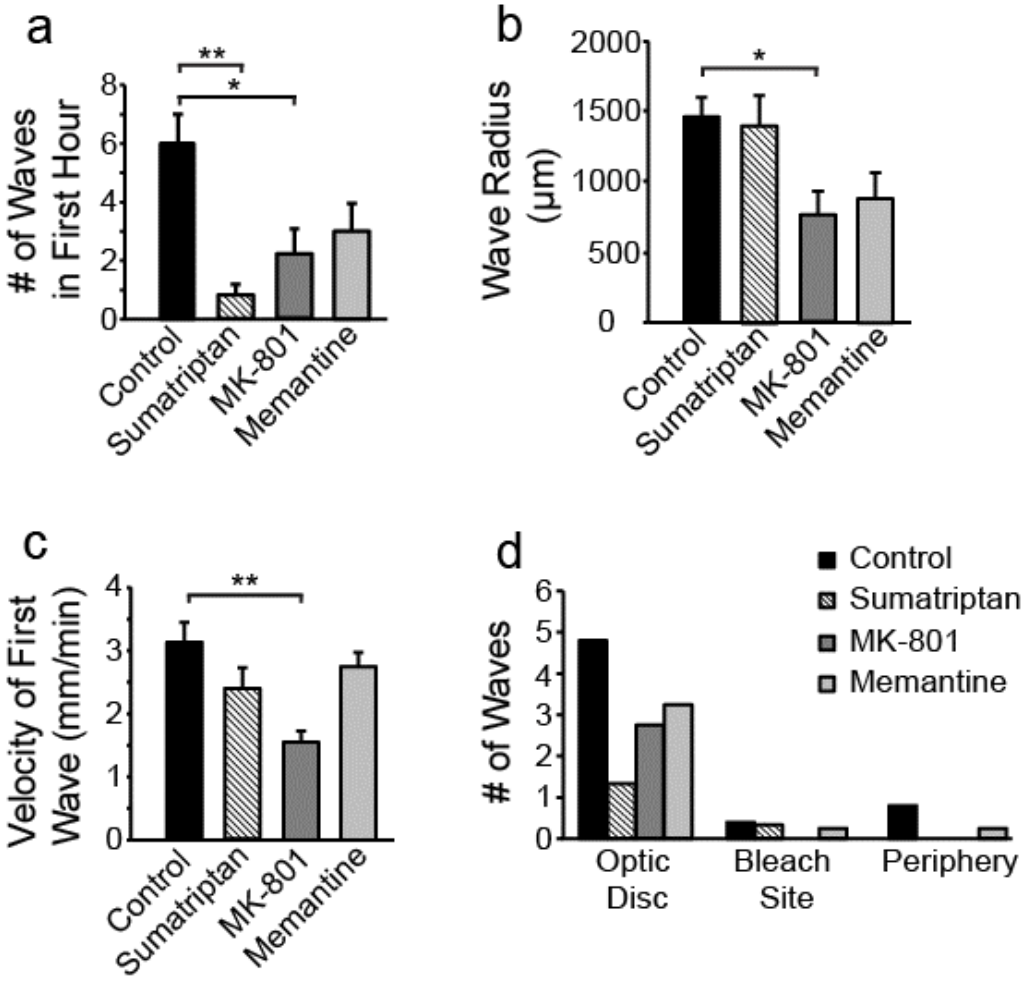

Figure 5.5. RSD is blocked by the 5-HT agonist sumatriptan, and by the NMDA antagonist MK-801. Drugs were injected i.v. 10 min before photothrombosis at concentrations of 3 mg/kg sumatriptan, 3 mg/kg MK-801, and 10 mg/kg memantine. (**a**) Sumatriptan and MK-801 decreased the incidence of wave generation during the first hour after photothrombosis. Memantine, another NMDA receptor antagonist, trended towards reducing the incidence of wave generation. (**b**) MK-801 decreased the size RSD waves. (**c**) MK-801 reduced RSD wave propagation velocity. (**d**) None of the drugs affected the site of RSD wave initiation. Regardless of treatment group, waves were predominantly initiated at the optic disc. For all panels, n = 5 animals per treatment group.

Most RSD waves were initiated near the optic disc, regardless of the site of thrombus formation. This property of RSD may be related to the nature of Müller cells, the primary glial cells in the retina. Müller cells are longer and thinner near the disc, where the retina is thickest[157]. Müller cells are primarily responsible for buffering extracellular levels of both glutamate[146] and K^{+}[20] and thinner cells may be less effective in rapidly removing glutamate and K^{+} from extracellular space[157]. This reduced capacity for glutamate and K^{+} buffering may render the region near the optic disc more sensitive to RSD initiation.

RSD was accompanied by a pronounced but brief arteriole vasoconstriction followed by a prolonged increase in blood flow lasting for an hour. The fact that blood flow increases following RSD at the same time that pO_2 remains below normal is not necessarily contradictory. In the minutes following a spreading depression episode a large metabolic demand is imposed on retinal tissue, as glutamate and K^{+} must be pumped back into neurons and glial cells[47, 54]. The increase in blood flow may result from this increased metabolic demand, but may not be sufficient to maintain O_2 at normal levels.

Oligemia, the third phase of altered blood flow that often accompanies CSD[54], was not observed in the retina. The reason for this difference is not clear, but could be related to the differing geometries of the retinal and cortical vasculatures. The retinal vasculature is restricted to two dimensions[158]. As such, there are fewer collateral routes for blood to supply an ischemic area. If total blood flow into the retina is redistributed across fewer vessels, blood flow will increase through the remaining patent vessels, accounting for the absence of oligemia.

A wealth of evidence demonstrates that CSD associated with pathology can expand the size of tissue damage. CSD events that occur following subarachnoid hemorrhage, malignant stroke, or traumatic brain injury can produce a delayed secondary ischemic infarct in patients[60]. In an animal model of ischemic stroke, CSD increases the metabolic demand in the penumbra and enlarges the ischemic core[47]. Blocking CSD events can limit injury expansion[155, 159] and cell death[155, 160]. The consequences of RSD on tissue damage in the retina are less clear. One study of cut injury-induced RSD in the hypoglycemic isolated chick retina found that RSD produced cell death in the macula, and that this damage could itself serve as a trigger for additional RSD waves. Blocking RSD prevented lesion formation[76]. Together, observations from the cortex and the

isolated retina strongly suggest that RSD has a deleterious effect on retinal health. Particularly following injury, such as ischemia, RSD could contribute to the evolution of retinal damage.

Our results have important clinical implications. It is not known whether RSD occurs in humans. However, given our observations that multiple RSD episodes are generated in an animal model of branch retinal vein and artery occlusion, and that CSD occurs in analogous vessel occlusions in the human cortex, it is likely that RSD also occurs in patients with BRVO and related vascular disorders. As in the cortex, tissue damage caused by vessel occlusion in the retina may be exacerbated by RSD episodes. Cell death may be reduced in these patients by blocking RSD generation. Importantly, we show that an NMDA receptor blocker and a 5-HT(1D) receptor agonist reduce the frequency of RSD wave generation. Drugs with these mechanisms of action are already clinically approved and may prove to be effective therapeutic agents that reduce vision loss in BRVO patients.

Chapter 6: General discussion

The methods developed and findings presented in this dissertation represent an effort to apply available tools in a novel way to study retinal blood flow and understand the consequences of blood flow disruption. Retinal vessel occlusion is among the leading causes of vision loss[5]. Previous research has been either clinically oriented, or has focused on elucidating the cellular evolution of injury by using histological techniques at discrete time points after injury. The data from these studies have been useful to understand the natural history of retinal vessel occlusion and the pathological changes that retinal tissue undergoes when faced with ischemia. However, research in this field can become more translational by combining clinical imaging methods with in vivo animal models to enable real-time observation of functional changes at the tissue and cellular level in various disease processes. In this thesis work, laser speckle flowmetry and in vivo glial Ca^{2+} imaging techniques already in use in brain research were developed for studying the in vivo retina.

LSF was first developed in the retina many decades ago[106], but computational demands limited the use of this imaging method. Since computers became more powerful and readily available, LSF has become a standard tool for studying hemodynamics in the brain[161]. Applying LSF to the retina has been more difficult due to the optical properties of the cornea and lens[162]. However, if these issues can be overcome, as we accomplished by illuminating the retina trans-sclerally, LSF offers the strengths of noninvasive imaging at high temporal and spatial resolution to generate a two dimensional map of blood flow changes. These advantages make LSF a useful tool for clinical imaging, and it has been applied to intraoperative brain imaging[163], and retinal imaging in disease[164]. We took advantage of these strengths and applied LSF imaging to animal models. In Chapter 5, LSF was used in a complimentary fashion to monitor blood flow in a model of retinal vessel occlusion. In Chapter 3, we applied LSF to image retinal functional hyperemia and discovered that local increases in blood flow are difficult to evoke when the stimulus is presented away from an arteriole, suggesting that arterioles, not capillaries, and the primary drivers of functional hyperemia. Since this observation, complementary techniques have corroborated this finding and shown that retinal capillaries dilate very little in response to neuronal stimulation[7].

Monitoring glial Ca^{2+} in vivo is a useful way to assess glial function and determine glial contributions to neurovascular coupling and pathophysiology. While Ca^{2+} indicator dyes, such as OGB (Chapter 4) have been applied to study cortical astrocyte function, in vivo use of these indicators for the study of retinal glia has been more difficult, since the retina is more difficult to access for dye administration. We developed a method to deliver Ca^{2+} indicators and caged Ca^{2+} compounds to the retina by way of intravitreal injection. Using these techniques, we demonstrated their utility in studying the role of glial Ca^{2+} in blood flow regulation. However, classical Ca^{2+} indicators have their limitations. First, while they tend to be preferentially taken up by glia, it is impossible to rule out some uptake by neurons. Thus, results obtained with these indicators always come with the caveat that some of the observed signal may be neuronal[165]. Secondly, their delivery always comes with some trauma. In the brain, they are ejected onto the cortical surface, often after exposing the brain through an invasive cranial window. In the retina, we must penetrate the globe with a needle and add volume into an enclosed space, both altering intraocular pressure. And these compounds are usually dissolved in DMSO, a highly toxic substance. Thirdly, the very nature of Ca^{2+} indicators disrupts physiological processes because a fluorescence signal relies on Ca^{2+} binding to the indicator, rather than acting at its target site[166].

In response to these limitations, there has been a rise in the use of newly developed genetically encoded Ca^{2+} indicators (GECIs). Unlike classical Ca^{2+} indicators, GECIs can be expressed in a genetic Cre-Lox system that allows the experimenter to regulate gene expression by systemic administration of tamoxifen[167]. However, use of GECIs without the need for viral vector delivery is currently limited to mouse lines. For in vivo retinal studies, the smaller eye and an apparent increased susceptibility to cataract formation make mice a more difficult model system to use than rats. Furthermore, observations from functional studies using GECIs to assess glial Ca^{2+} signaling in the brain have contradicted previous findings that used classical Ca^{2+} indicators, calling into question the role of glia in neurovascular coupling[165, 168]. As a result, there is a new need to carefully characterize the functional mechanisms of both Ca^{2+} indicator techniques to resolve these conflicting results.

Ongoing work in our laboratory has taken advantage of GECIs to characterize how Müller cell Ca^{2+} becomes altered in ischemic injury, since this topic has remained remarkably unexplored. The eventual goal of characterizing glial Ca^{2+} signals in ischemic pathology is to identify the functional consequences of this signaling. It is unclear whether increased Ca^{2+} signaling in ischemia is protective or injurious to the retina. In the brain, blocking Ca^{2+} signaling with Ca^{2+} chelators was found to be protective[34]. However, glial release of vasodilators occurs in a Ca^{2+} dependent manner. Could the increased glial Ca^{2+} to release vasodilators be a mechanism by which ischemic tissue tries to increase collateral blood flow? Or is increased Ca^{2+} a response to limited access to glucose and O_2? Understanding the functional role of glial Ca^{2+} in pathology could provide new clinical interventions that could harness the protective effects of glia or block glial contribution to injury.

The mainstay in retinal vessel occlusion therapy has been to manage the secondary complications of ischemia, as discussed in Chapter 1. However, these therapies do not reverse vision loss and are often laborious for both patient and clinician (ie: monthly intravitreal injections). The discovery of RSD in the in vivo, vascular retina has been a very exciting finding because it may provide a new therapeutic target that would limit cell death, reducing secondary complications and helping to preserve vision. Strong evidence from the brain shows that CSD contributes to injury. This is likely to be the case in the retina, too. The characterization of RSD in Chapter 5 leaves many outstanding questions. From a functional perspective, it is unclear why RSD would be generated with such consistency from the optic disc. We have proposed that it may be related to the differential Müller cell morphology and K^+ buffering and glutamate uptake capacity across the retina. This hypothesis needs to be tested. Understanding this peculiar susceptibility of the optic disc to generate RSD waves could provide new insights into retinal function and the mechanisms of RSD generation.

Additionally, the impact of RSD on injury progression is unknown. Our data shows that vessel occlusion produces RGC loss, and several pharmacological agents are able to affect RSD frequency, size, and velocity. However, can blocking RSD limit how many RGCs die and limit vision loss? Answering this question will be critical for assessing whether RSD is a viable target for developing new therapies. However, trying to separate drug effects on RSD from drug effects on excitotoxicity will complicate data

interpretation, since spreading depression and excitotoxicity are inexorably linked. Regardless, the possibility for clinical intervention also relies on answering the biggest outstanding question: does RSD occur in humans? This may be a difficult question to address since it is also unknown whether RSD continues to occur beyond an hour after vessel occlusion. CSD after injury occurs relatively infrequently, and capturing these events required a method of chronic monitoring that was unavailable until recently. Chronic subdural electrode monitoring finally allowed clinicians to record CSD episodes many days after initial injury. A similar advancement in retinal monitoring technology will likely be required to identify RSD in human patients, particularly since the latency between vessel occlusion and seeking medical care can be hours or days.

The findings presented here have used novel imaging methods in an in vivo rat model to demonstrate the involvement of glial Ca^{2+} signaling on blood flow (Chapter 4), and LSF imaging to demonstrate that retinal functional hyperemia is likely driven by arterioles rather than controlled at the capillary layer (Chapter 3). Use of these methods to study retinal ischemia led to the discovery of RSD, and is the first demonstration of RSD in vivo in a vascular retina (Chapter 5). In the future, these techniques can be applied to further characterize RSD, particularly with regard to glial Ca^{2+} signaling and blood flow changes.

Reference List

1. Miller,R.F. The physiology and morphology of the vertebrate retina in *Retina* (ed. Ryan,S.J.) 138-170 (Mosby, St.Louis, 2001).

2. Regatieri,C.V.S., Roh,S., & Weiter,J.J. Retinal and Choroidal Circulation in *Ophthalmology* (eds. Yanoff,M. & Duker,J.S.) 426-429.e1 (London : Elsevier/Saunders, London, 2013).

3. Anand-Apte,B. & Hollyfield,J.G. Developmental anatomy of the retinal and choroidal vasculature in *Encyclopedia of the Eye* (eds. Besharse,J. & Bok,D.) 9-15 (Academic Press, Elsevier Books, London, 2010).

4. Wassle,H. Parallel processing in the mammalian retina. *Nat. Rev. Neurosci.* **5**, 747-757 (2004).

5. Osborne,N.N. *et al.* Retinal ischemia: mechanisms of damage and potential therapeutic strategies. *Prog. Retin. Eye Res.* **23**, 91-147 (2004).

6. Bill,A., Sperber,G., & Ujiie,K. Physiology of the choroidal vascular bed. *Int. Ophthalmol.* **6**, 101-107 (1983).

7. Kornfield,T.E. & Newman,E.A. Regulation of blood flow in the retinal trilaminar vascular network. *J. Neurosci.* **34**, 11504-11513 (2014).

8. Yu,D.Y. & Cringle,S.J. Retinal degeneration and local oxygen metabolism. *Exp. Eye Res.* **80**, 745-751 (2005).

9. Newman,E.A. Glial cell regulation of neuronal activity and blood flow in the retina by release of gliotransmitters. *Philosophical Transactions of the Royal Society of London B: Biological Sciences* **370**, (2015).

10. Reichenbach,A. & Bringmann,A. New functions of Muller cells. *Glia* **61**, 651-678 (2013).

11. Newman,E.A. Retinal glia in *Encyclopedia of Neuroscience* (ed. Squire,L.R.) 225-232 (Academic Press, Oxford, 2009).

12. Lindsay,K.J. *et al.* Pyruvate kinase and aspartate-glutamate carrier distributions reveal key metabolic links between neurons and glia in retina. *Proc. Natl. Acad. Sci. U. S. A.* **111**, 15579-15584 (2014).

13. Huster,D., Reichenbach,A., & Reichelt,W. The glutathione content of retinal Müller (glial) cells: effect of pathological conditions. *Neurochem. Int.* **36**, 461-469 (2000).

14. Stevens,E.R. *et al.* D-serine and serine racemase are present in the vertebrate retina and contribute to the physiological activation of NMDA receptors. *Proc. Natl. Acad. Sci. U. S. A.* **100**, 6789-6794 (2003).

15. Newman,E.A. Glial cell inhibition of neurons by release of ATP. *J. Neurosci.* **23**, 1659-1666 (2003).

16. Linnertz,R. *et al.* Activation of voltage-gated Na^+ and Ca^{2+} channels is required for glutamate release from retinal glial cells implicated in cell volume regulation. *Neuroscience* **188**, 23-34 (2011).

17. Karwoski,C.J., Lu,H.K., & Newman,E.A. Spatial buffering of light-evoked potassium increases by retinal Müller (glial) cells. *Science* **244**, 578-580 (1989).

18. Kofuji,P. *et al.* Genetic inactivation of an inwardly rectifying potassium channel (Kir4.1 subunit) in mice: phenotypic impact in retina. *J. Neurosci.* **20**, 5733-5740 (2000).

19. Kofuji,P. & Newman,E.A. Potassium buffering in the central nervous system. *Neuroscience* **129**, 1045-1056 (2004).

20. Newman,E.A., Frambach,D.A., & Odette,L.L. Control of extracellular potassium levels by retinal glial cell K^+ siphoning. *Science* **225**, 1174-1175 (1984).

21. Metea,M.R. & Newman,E.A. Glial cells dilate and constrict blood vessels: a mechanism of neurovascular coupling. *J. Neurosci.* **26**, 2862-2870 (2006).

22. Pournaras,C.J., Rungger-Brandle,E., Riva,C.E., Hardarson,S.H., & Stefansson,E. Regulation of retinal blood flow in health and disease. *Prog. Retin. Eye Res.* **27**, 284-330 (2008).

23. Hamel,E. Perivascular nerves and the regulation of cerebrovascular tone. *J. Appl. Physiol.* **100**, 1059-1064 (2006).

24. Furukawa,H. Autonomic innervation of preretinal blood vessels of the rabbit. *Invest. Ophthalmol. Vis. Sci.* **28**, 1752-1760 (1987).

25. Schmidl,D. *et al.* Role of nitric oxide in optic nerve head blood flow regulation during an experimental increase in intraocular pressure in healthy humans. *Exp. Eye Res.* **116**, 247-253 (2013).

26. Kur,J. & Newman,E.A. Purinergic control of vascular tone in the retina. *J. Physiol.* **592**, 491-504 (2014).

27. Mosso,A. Sulla circolazione del sangue nel cervello dell'uomo. *R. Accad. Lincei* **5**, 237-358 (1880).

28. Roy,C.S. & Sherrington,C.S. On the regulation of the blood-supply of the brain. *J. Physiol.* **11**, 85-108 (1890).

29. Park,L. *et al.* Key role of tissue plasminogen activator in neurovascular coupling. *Proc. Natl. Acad. Sci. U. S. A.* **105**, 1073-1078 (2008).

30. Attwell,D. *et al.* Glial and neuronal control of brain blood flow. *Nature* **468**, 232-243 (2010).

31. Moskowitz,M.A., Lo,E.H., & Iadecola,C. The science of stroke: mechanisms in search of treatments. *Neuron* **67**, 181-198 (2010).

32. Duffy,S. & MacVicar,B.A. In vitro ischemia promotes calcium influx and intracellular calcium release in hippocampal astrocytes. *J. Neurosci.* **16**, 71-81 (1996).

33. Doyle,K.P. *et al.* B-lymphocyte-mediated delayed cognitive impairment following stroke. *J. Neurosci.* **35**, 2133-2145 (2015).

34. Ding,S., Wang,T., Cui,W., & Haydon,P.G. Photothrombosis ischemia stimulates a sustained astrocytic Ca^{2+} signaling *in vivo*. *Glia* **57**, 767-776 (2009).

35. Watson,B.D., Dietrich,W.D., Busto,R., Wachtel,M.S., & Ginsberg,M.D. Induction of reproducible brain infarction by photochemically initiated thrombosis. *Ann. Neurol.* **17**, 497-504 (1985).

36. Rossi,D.J., Brady,J.D., & Mohr,C. Astrocyte metabolism and signaling during brain ischemia. *Nat. Neurosci.* **10**, 1377-1386 (2007).

37. Szatkowski,M., Barbour,B., & Attwell,D. Non-vesicular release of glutamate from glial cells by reversed electrogenic glutamate uptake. *Nature* **348**, 443-446 (1990).

38. Kuchibhotla,K.V., Lattarulo,C.R., Hyman,B.T., & Bacskai,B.J. Synchronous hyperactivity and intercellular calcium waves in astrocytes in Alzheimer mice. *Science* **323**, 1211-1215 (2009).

39. Ding,S. *et al.* Enhanced astrocytic Ca^{2+} signals contribute to neuronal excitotoxicity after status epilepticus. *J. Neurosci.* **27**, 10674-10684 (2007).

40. Scemes,E. & Giaume,C. Astrocyte calcium waves: what they are and what they do. *Glia* **54**, 716-725 (2006).

41. Zheng,W., Talley,W.L., Holstein,D.M., Wewer,J., & Lechleiter,J.D. P2Y1R-initiated, IP3R-dependent stimulation of astrocyte mitochondrial metabolism reduces and partially reverses ischemic neuronal damage in mouse. *J. Cereb. Blood Flow Metab.* **33**, 600-611 (2013).

42. Dong,Q.P., He,J.Q., & Chai,Z. Astrocytic Ca^{2+} waves mediate activation of extrasynaptic NMDA receptors in hippocampal neurons to aggravate brain damage during ischemia. *Neurobiol. Dis.* **58**, 68-75 (2013).

43. Yemisci,M. *et al.* Pericyte contraction induced by oxidative-nitrative stress impairs capillary reflow despite successful opening of an occluded cerebral artery. *Nat. Med.* **15**, 1031-1037 (2009).

44. Hall,C.N. *et al.* Capillary pericytes regulate cerebral blood flow in health and disease. *Nature* **508**, 55-60 (2014).

45. Kamel,H. & Iadecola,C. Brain-immune interactions and ischemic stroke: clinical implications. *Arch. Neurol.* **69**, 576-581 (2012).

46. Iadecola,C. & Anrather,J. The immunology of stroke: from mechanisms to translation. *Nat. Med.* **17**, 796-808 (2011).

47. von Bornstädt,D. *et al.* Supply-demand mismatch transients in susceptible peri-infarct hot zones explain the origins of spreading injury depolarizations. *Neuron* **85**, 1117-1131 (2015).

48. Nedergaard,M. & Hansen,A.J. Characterization of cortical depolarizations evoked in focal cerebral ischemia. *J. Cereb. Blood Flow Metab.* **13**, 568-574 (1993).

49. Leão,A.A.P. Spreading depression of activity in the cerebral cortex. *J. Neurophysiol.* **7**, 359-390 (1944).

50. Lauritzen,M. Cortical spreading depression as a putative migraine. *Trends Neurosci.* **10**, 8-13 (1987).

51. Lauritzen,M. Pathophysiology of the migraine aura. The spreading depression theory. *Brain* **117**, 199-210 (1994).

52. Lauritzen,M. *et al.* Clinical relevance of cortical spreading depression in neurological disorders: migraine, malignant stroke, subarachnoid and intracranial hemorrhage, and traumatic brain injury. *J. Cereb. Blood Flow Metab.* **31**, 17-35 (2011).

53. Somjen,G.G. Mechanisms of spreading depression and hypoxic spreading depression-like depolarization. *Physiol. Rev.* **81**, 1065-1096 (2001).

54. Ayata,C. & Lauritzen,M. Spreading Depression, Spreading Depolarizations, and the Cerebral Vasculature. *Physiol Rev.* **95**, 953-993 (2015).

55. Zhou,N. *et al.* Regenerative glutamate release by presynaptic NMDA receptors contributes to spreading depression. *J. Cereb. Blood Flow Metab* **33**, 1582-1594 (2013).

56. de Oliveira Castro,G. & Martins-Ferreira,H. Deformations and thickness variations accompanying spreading depression in the retina. *J. Neurophysiol.* **33**, 891-900 (1970).

57. Basarsky,T.A., Feighan,D., & MacVicar,B.A. Glutamate release through volume-activated channels during spreading depression. *J. Neurosci.* **19**, 6439-6445 (1999).

58. Farkas,E., Pratt,R., Sengpiel,F., & Obrenovitch,T.P. Direct, live imaging of cortical spreading depression and anoxic depolarisation using a fluorescent, voltage-sensitive dye. *J. Cereb. Blood Flow Metab.* **28**, 251-262 (2008).

59. Netto,M. & Martins-Ferreira,H. Elicitation of spreading depression by rose bengal photodynamic action. *Photochem. Photobiol.* **50**, 229-234 (1989).

60. Dreier,J.P. *et al.* Delayed ischaemic neurological deficits after subarachnoid haemorrhage are associated with clusters of spreading depolarizations. *Brain* **129**, 3224-3237 (2006).

61. Jarvis,C.R., Anderson,T.R., & Andrew,R.D. Anoxic depolarization mediates acute damage independent of glutamate in neocortical brain slices. *Cereb. Cortex* **11**, 249-259 (2001).

62. Hinzman,J.M., DiNapoli,V.A., Mahoney,E.J., Gerhardt,G.A., & Hartings,J.A. Spreading depolarizations mediate excitotoxicity in the development of acute cortical lesions. *Exp. Neurol.* **267**, 243-253 (2015).

63. Unekawa,M. *et al.* Hyperperfusion counteracted by transient rapid vasoconstriction followed by long-lasting oligemia induced by cortical spreading depression in anesthetized mice. *J. Cereb. Blood Flow Metab* **35**, 689-698 (2015).

64. Fabricius,M., Akgoren,N., & Lauritzen,M. Arginine-nitric oxide pathway and cerebrovascular regulation in cortical spreading depression. *Am. J. Physiol.* **269**, H23-H29 (1995).

65. Lauritzen,M., Jørgensen,M.B., Diemer,N.H., Gjedde,A., & Hansen,A.J. Persistent oligemia of rat cerebral cortex in the wake of spreading depression. *Ann. Neurol.* **12**, 469-474 (1982).

66. Gouras,P. Spreading depression of activity in amphibian retina. *Am. J. Physiol.* **195**, 28-32 (1958).

67. Girouard,H. *et al.* Astrocytic endfoot Ca^{2+} and BK channels determine both arteriolar dilation and constriction. *Proc. Natl. Acad. Sci. U. S. A.* **107**, 3811-3816 (2010).

68. Fordsmann,J.C. *et al.* Increased 20-HETE synthesis explains reduced cerebral blood flow but not impaired neurovascular coupling after cortical spreading depression in rat cerebral cortex. *J. Neurosci.* **33**, 2562-2570 (2013).

69. Hertle,D.N. *et al.* Effect of analgesics and sedatives on the occurrence of spreading depolarizations accompanying acute brain injury. *Brain* **135**, 2390-2398 (2012).

70. Netto,M., do Carmo,R.J., & Martins-Ferreira,H. Retinal spreading depression induced by photoactivation: involvement of free radicals and potassium. *Brain Res.* **827**, 221-224 (1999).

71. do Carmo,R.J. & Martins-Ferreira,H. Spreading depression of Leao probed with ion-selective microelectrodes in isolated chick retina. *An. Acad. Bras. Cienc.* **56**, 401-421 (1984).

72. Mori,S., Miller,W.H., & Tomita,T. Muller cell function during spreading depression in frog retina. *Proc. Natl. Acad. Sci. U. S. A.* **73**, 1351-1354 (1976).

73. Olsen,J.S. & Miller,R.F. Spontaneous slow potentials and spreading depression in amphibian retina. *J. Neurophysiol.* **40**, 752-767 (1977).

74. Higashida,H., Sakakibara,M., & Mitarai,G. Spreading depression in isolated carp retina. *Brain Res.* **120**, 67-83 (1977).

75. Van Harreveld,A. Two mechanisms for spreading depression in the chicken retina. *J. Neurobiol.* **9**, 419-431 (1978).

76. Yu,Y. *et al.* Reentrant spiral waves of spreading depression cause macular degeneration in hypoglycemic chicken retina. *Proc. Natl. Acad. Sci. U. S. A.* **109**, 2585-2589 (2012).

77. Martins-Ferreira,H., Nedergaard,M., & Nicholson,C. Perspectives on spreading depression. *Brain Res. Rev.* **32**, 215-234 (2000).

78. Ripps,H., Mehaffey,L., III, & Siegel,I.M. "Rapid regeneration" in the cat retina: a case for spreading depression. *J. Gen. Physiol.* **77**, 335-346 (1981).

79. Rehak,J. & Rehak,M. Branch retinal vein occlusion: pathogenesis, visual prognosis, and treatment modalities. *Curr. Eye Res.* **33**, 111-131 (2008).

80. Muraoka,Y. *et al.* Morphologic and functional changes in retinal vessels associated with branch retinal vein occlusion. *Ophthalmology* **120**, 91-99 (2013).

81. Zhang,Y. *et al.* Natural history and histology in a rat model of laser-induced photothrombotic retinal vein occlusion. *Curr. Eye Res.* **33**, 365-376 (2008).

82. Schmid,H., Renner,M., Dick,H.B., & Joachim,S.C. Loss of inner retinal neurons after retinal ischemia in rats. *Invest Ophthalmol. Vis. Sci.* **55**, 2777-2787 (2014).

83. Ikeda,F. & Kishi,S. Inner neural retina loss in central retinal artery occlusion. *Jpn. J. Ophthalmol.* **54**, 423-429 (2010).

84. Mosinger,J.L. & Olney,J.W. Photothrombosis-induced ischemic neuronal degeneration in the rat retina. *Exp. Neurol.* **105**, 110-113 (1989).

85. Juarez,C.P., Tso,M.O., van Heuven,W.A., Hayreh,M.S., & Hayreh,S.S. Experimental retinal vascular occlusion. III. An ultrastructural study of

simultaneous occlusion of central retinal vein and artery. *Int. Ophthalmol.* **9**, 89-101 (1986).

86. Zhang,H. *et al.* Development of a new mouse model of branch retinal vein occlusion and retinal neovascularization. *Jpn. J. Ophthalmol.* **51**, 251-257 (2007).

87. Xin,X. *et al.* Hypoxic retinal Müller cells promote vascular permeability by HIF-1-dependent up-regulation of angiopoietin-like 4. *Proc. Natl. Acad. Sci. U. S. A* **110**, E3425-E3434 (2013).

88. Jung,S.H., Kim,K.A., Sohn,S.W., & Yang,S.J. Association of aqueous humor cytokines with the development of retinal ischemia and recurrent macular edema in retinal vein occlusion. *Invest Ophthalmol. Vis. Sci.* **55**, 2290-2296 (2014).

89. Rehak,M. *et al.* Retinal gene expression and Müller cell responses after branch retinal vein occlusion in the rat. *Invest. Ophthalmol. Vis. Sci.* **50**, 2359-2367 (2009).

90. Wurm,A. *et al.* Effects of ischemia-reperfusion on physiological properties of Müeller glial cells in the porcine retina. *Invest. Ophthalmol. Vis. Sci.* **52**, 3360-3367 (2011).

91. Mosinger,J.L. *et al.* Blockade of both NMDA and non-NMDA receptors is required for optimal protection against ischemic neuronal degeneration in the in vivo adult mammalian retina. *Exp. Neurol.* **113**, 10-17 (1991).

92. Hayreh,S.S. & Weingeist,T.A. Experimental occlusion of the central artery of the retina. IV: Retinal tolerance time to acute ischaemia. *Br. J. Ophthalmol.* **64**, 818-825 (1980).

93. Yu,D.Y., Cringle,S.J., Yu,P.K., & Su,E.N. Intraretinal oxygen distribution and consumption during retinal artery occlusion and graded hyperoxic ventilation in the rat. *Invest. Ophthalmol. Vis. Sci.* **48**, 2290-2296 (2007).

94. Wasilewa,P., Hockwin,O., & Korte,I. Glycogen concentration changes in retina, vitreous body and other eye tissues caused by disturbances of blood circulation. *Albrecht. Von. Graefes Arch. Klin. Exp. Ophthalmol.* **199**, 115-120 (1976).

95. Beaumont,P.E. & Kang,H.K. Clinical characteristics of retinal venous occlusions occurring at different sites. *Br. J. Ophthalmol.* **86**, 572-580 (2002).

96. Hayreh,S.S. & Zimmerman,M.B. Branch retinal vein occlusion: natural history of visual outcome. *JAMA Ophthalmol.* **132**, 13-22 (2014).

97. Hayreh,S.S., Podhajsky,P.A., & Zimmerman,M.B. Branch retinal artery occlusion: natural history of visual outcome. *Ophthalmology* **116**, 1188-1194 (2009).

98. Mason,J.O., III *et al.* Branch retinal artery occlusion: visual prognosis. *Am. J. Ophthalmol.* **146**, 455-457 (2008).

99. Goldman,D.R., Shah,C.P., Morley,M.G., & Heier,J.S. Venous Occlusive Disease of the Retina in *Ophthalmology* (eds. Yanoff,M. & Duker,J.S.) 526-534.e1 (London : Elsevier/Saunders, London, 2013).

100. Avitabile,T., Longo,A., & Reibaldi,A. Intravitreal triamcinolone compared with macular laser grid photocoagulation for the treatment of cystoid macular edema. *Am. J. Ophthalmol.* **140**, 695-702 (2005).

101. Yeh,S. *et al.* Therapies for macular edema associated with central retinal vein occlusion: a report by the American Academy of Ophthalmology. *Ophthalmology* **122**, 769-778 (2015).

102. Srienc,A.I., Kurth-Nelson,Z.L., & Newman,E.A. Imaging retinal blood flow with laser speckle flowmetry. *Front. Neuroenerg.* **2**, 128 (2010).

103. Schaffer,C.B. *et al.* Two-photon imaging of cortical surface microvessels reveals a robust redistribution in blood flow after vascular occlusion. *PLoS Biol.* **4**, 258-270 (2006).

104. Yuan,S., Devor,A., Boas,D.A., & Dunn,A.K. Determination of optimal exposure time for imaging of blood flow changes with laser speckle contrast imaging. *Appl. Opt.* **44**, 1823-1830 (2005).

105. Dunn,A.K., Bolay,H., Moskowitz,M.A., & Boas,D.A. Dynamic imaging of cerebral blood flow using laser speckle. *J. Cereb. Blood Flow Metab.* **21**, 195-201 (2001).

106. Fercher,A.F. & Briers,J.D. Flow visualization by means of single-exposure speckle photography. *Opt. Commun.* **37**, 326-330 (1981).

107. Cheng,H. & Duong,T.Q. Simplified laser-speckle-imaging analysis method and its application to retinal blood flow imaging. *Opt. Lett.* **32**, 2188-2190 (2007).

108. Jacobs,G.H., Fenwick,J.A., & Williams,G.A. Cone-based vision of rats for ultraviolet and visible lights. *J. Exp. Biol.* **204**, 2439-2446 (2001).

109. Riva,C.E., Logean,E., & Falsini,B. Visually evoked hemodynamical response and assessment of neurovascular coupling in the optic nerve and retina. *Prog. Retin. Eye Res.* **24**, 183-215 (2005).

110. Newman,E.A. & Zahs,K.R. Calcium waves in retinal glial cells. *Science* **275**, 844-847 (1997).

111. Newman,E.A. & Bartosch,R. An eyecup preparation for the rat and mouse. *J. Neurosci. Methods* **93**, 169-175 (1999).

112. Hultman,D. & Newman,E.A. A micro-advancer device for vitreal injection and retinal recording and stimulation. *Exp. Eye Res.* **93**, 767-770 (2011).

113. Kornfield,T.E. & Newman,E.A. Measurement of retinal blood flow using fluorescently labeled red blood cells. *eneuro* **2**, (2015).

114. Mead,B. *et al.* Comparative evaluation of methods for estimating retinal ganglion cell loss in retinal sections and wholemounts. *PLoS One* **9**, e110612 (2014).

115. Franceschini,M.A. *et al.* The effect of different anesthetics on neurovascular coupling. *Neuroimage* **51**, 1367-1377 (2010).

116. Newman,E.A. Propagation of intercellular calcium waves in retinal astrocytes and Müller cells. *J. Neurosci.* **21**, 2215-2223 (2001).

117. Kuchitsu,K., Ward,J.M., Allen,G.J., Schelle,I., & Schroeder,J.I. Loading acetoxymethyl ester fluorescent dyes into the cytoplasm of Arabidopsis and Commelina guard cells. *New Phytol.* **153**, 527-533 (2002).

118. Bolay,H. *et al.* Intrinsic brain activity triggers trigeminal meningeal afferents in a migraine model. *Nat. Med.* **8**, 136-142 (2002).

119. Ayata,C. *et al.* Laser speckle flowmetry for the study of cerebrovascular physiology in normal and ischemic mouse cortex. *J. Cereb. Blood Flow Metab.* **24**, 744-755 (2004).

120. Durduran,T. *et al.* Spatiotemporal quantification of cerebral blood flow during functional activation in rat somatosensory cortex using laser-speckle flowmetry. *J. Cereb. Blood Flow Metab.* **24**, 518-525 (2004).

121. Briers,J.D. & Fercher,A.F. Retinal blood-flow visualization by means of laser speckle photography. *Invest. Ophthalmol. Vis. Sci.* **22**, 255-259 (1982).

122. Tamaki,Y., Araie,M., Kawamoto,E., Eguchi,S., & Fujii,H. Noncontact, two-dimensional measurement of retinal microcirculation using laser speckle phenomenon. *Invest. Ophthalmol. Vis. Sci.* **35**, 3825-3834 (1994).

123. Cheng,H., Yan,Y., & Duong,T.Q. Temporal statistical analysis of laser speckle images and its application to retinal blood-flow imaging. *Opt. Express* **16**, 10214-10219 (2008).

124. Tamaki,Y., Araie,M., Tomita,K., & Tomidokoro,A. Effect of topical timolol on tissue circulation in optic nerve head. *Jpn. J. Ophthalmol.* **41**, 297-304 (1997).

125. Ishii,K. & Araie,M. Effect of topical Latanoprost-timolol combined therapy on retinal blood flow and circulation of optic nerve head tissue in cynomolgus monkeys. *Jpn. J. Ophthalmol.* **44**, 227-234 (2000).

126. Koseki,N. *et al.* A placebo-controlled 3-year study of a calcium blocker on visual field and ocular circulation in glaucoma with low-normal pressure. *Ophthalmology* **115**, 2049-2057 (2008).

127. Watanabe,G., Fujii,H., & Kishi,S. Imaging of choroidal hemodynamics in eyes with polypoidal choroidal vasculopathy using laser speckle phenomenon. *Jpn. J. Ophthalmol.* **52**, 175-181 (2008).

128. Iadecola,C. & Nedergaard,M. Glial regulation of the cerebral microvasculature. *Nat. Neurosci.* **10**, 1369-1376 (2007).

129. Duong,T.Q., Ngan,S.C., Ugurbil,K., & Kim,S.G. Functional magnetic resonance imaging of the retina. *Invest. Ophthalmol. Vis. Sci.* **43**, 1176-1181 (2002).

130. Bhutto,I.A. & Amemiya,T. Microvascular architecture of the rat choroid: corrosion cast study. *Anat. Rec.* **264**, 63-71 (2001).

131. Harel,N., Lee,S.P., Nagaoka,T., Kim,D.S., & Kim,S.G. Origin of negative blood oxygenation level-dependent fMRI signals. *J. Cereb. Blood Flow Metab.* **22**, 908-917 (2002).

132. Devor,A. *et al.* Coupling of the cortical hemodynamic response to cortical and thalamic neuronal activity. *Proc. Natl. Acad. Sci. U. S. A.* **102**, 3822-3827 (2005).

133. Tamaki,Y. *et al.* Real-time measurement of human optic nerve head and choroid circulation, using the laser speckle phenomenon. *Jpn. J. Ophthalmol.* **41**, 49-54 (1997).

134. Faraci,F.M. & Heistad,D.D. Regulation of large cerebral arteries and cerebral microvascular pressure. *Circ. Res.* **66**, 8-17 (1990).

135. Zweifach,B.W. Quantitative studies of microcirculatory structure and function. I. Analysis of pressure distribution in the terminal vascular bed in cat mesentery. *Circ. Res.* **34**, 843-857 (1974).

136. Iadecola,C. Neurovascular regulation in the normal brain and in Alzheimer's disease. *Nat. Rev. Neurosci.* **5**, 347-360 (2004).

137. Lipowsky,H.H. Microvascular rheology and hemodynamics. *Microcirculation* **12**, 5-15 (2005).

138. Boas,D.A., Jones,S.R., Devor,A., Huppert,T.J., & Dale,A.M. A vascular anatomical network model of the spatio-temporal response to brain activation. *Neuroimage* **40**, 1116-1129 (2008).

139. Kawamura,H. *et al.* ATP: a vasoactive signal in the pericyte-containing microvasculature of the rat retina. *J. Physiol.* **551.3**, 787-799 (2003).

140. Wu,D.M., Kawamura,H., Sakagami,K., Kobayashi,M., & Puro,D.G. Cholinergic regulation of pericyte-containing retinal microvessels. *Am. J. Physiol. Heart Circ. Physiol.* **284**, H2083-H2090 (2003).

141. Peppiatt,C.M., Howarth,C., Mobbs,P., & Attwell,D. Bidirectional control of CNS capillary diameter by pericytes. *Nature* **443**, 700-704 (2006).

142. Iadecola,C., Yang,G., Ebner,T.J., & Chen,G. Local and propagated vascular responses evoked by focal synaptic activity in cerebellar cortex. *J. Neurophysiol.* **78**, 651-659 (1997).

143. Erinjeri,J.P. & Woolsey,T.A. Spatial integration of vascular changes with neural activity in mouse cortex. *J. Cereb. Blood Flow Metab.* **22**, 353-360 (2002).

144. Takano,T. *et al.* Astrocyte-mediated control of cerebral blood flow. *Nat. Neurosci.* **9**, 260-267 (2006).

145. Kofuji,P. & Newman,E.A. Potassium homeostasis in glia in *Encyclopedia of Neuroscience* (ed. Squire,L.R.) 867-872 (Academic Press, Oxford, 2009).

146. Brew,H. & Attwell,D. Electrogenic glutamate uptake is a major current carrier in the membrane of axolotl retinal glial cells. *Nature* **327**, 707-709 (1987).

147. Newman,E.A. Calcium increases in retinal glial cells evoked by light-induced neuronal activity. *J. Neurosci.* **25**, 5502-5510 (2005).

148. Clark,B.D., Kurth-Nelson,Z.L., & Newman,E.A. Adenosine-evoked hyperpolarization of retinal ganglion cells is mediated by G-protein-coupled inwardly rectifying K^+ and small conductance Ca^{2+}-activated K^+ channel activation. *J. Neurosci.* **29**, 11237-11245 (2009).

149. Metea,M.R., Kofuji,P., & Newman,E.A. Neurovascular coupling is not mediated by potassium siphoning from glial cells. *J. Neurosci.* **27**, 2468-2471 (2007).

150. Gordon,G.R.J., Choi,H.B., Rungta,R.L., Ellis-Davies,G.C.R., & MacVicar,B.A. Brain metabolism dictates the polarity of astrocyte control over arterioles. *Nature* **456**, 745-749 (2008).

151. Kurth-Nelson,Z.L., Mishra,A., & Newman,E.A. Spontaneous glial calcium waves in the retina develop over early adulthood. *J. Neurosci.* **29**, 11339-11346 (2009).

152. Takano,T. *et al.* Cortical spreading depression causes and coincides with tissue hypoxia. *Nat. Neurosci.* **10**, 754-762 (2007).

153. Malkov,A. *et al.* Reactive oxygen species initiate a metabolic collapse in hippocampal slices: potential trigger of cortical spreading depression. *J. Cereb. Blood Flow Metab.* **34**, 1540-1549 (2014).

154. Piilgaard,H. & Lauritzen,M. Persistent increase in oxygen consumption and impaired neurovascular coupling after spreading depression in rat neocortex. *J. Cereb. Blood Flow Metab.* **29**, 1517-1527 (2009).

155. Gill,R., Andine,P., Hillered,L., Persson,L., & Hagberg,H. The effect of MK-801 on cortical spreading depression in the penumbral zone following focal ischaemia in the rat. *J. Cereb. Blood Flow Metab.* **12**, 371-379 (1992).

156. Maranhao-Filho,P.A., Martins-Ferreira,H., Vincent,M.B., Ribeiro,L.J., & Novis,S.A. Sumatriptan blocks spreading depression in isolated chick retina. *Cephalalgia* **17**, 822-825 (1997).

157. Reichenbach,A. & Wohlrab,F. Morphometric parameters of Muller (glial) cells dependent on their topographic localization in the nonmyelinated part of the rabbit retina. A consideration of functional aspects of radial glia. *J. Neurocytol.* **15**, 451-459 (1986).

158. Kur,J., Newman,E.A., & Chan-Ling,T. Cellular and physiological mechanisms underlying blood flow regulation in the retina and choroid in health and disease. *Prog. Retin. Eye Res.* **31**, 377-406 (2012).

159. Dreier,J.P. *et al.* Spreading ischemia after aneurysmal subarachnoid hemorrhage. *Acta Neurochir. Suppl.* **115**, 125-129 (2013).

160. Sadeghian,H. *et al.* Neuronal death by repetitive cortical spreading depression in juvenile rat brain. *Exp. Neurol.* **233**, 438-446 (2012).

161. Boas,D.A. & Dunn,A.K. Laser speckle contrast imaging in biomedical optics. *J. Biomed. Opt.* **15**, 011109-1 (2010).

162. Ponticorvo,A., Cardenas,D., Dunn,A.K., Ts'o,D., & Duong,T.Q. Laser speckle contrast imaging of blood flow in rat retinas using an endoscope. *J. Biomed. Opt.* **18**, 090501 (2013).

163. Hecht,N., Woitzik,J., Konig,S., Horn,P., & Vajkoczy,P. Laser speckle imaging allows real-time intraoperative blood flow assessment during neurosurgical procedures. *J. Cereb. Blood Flow Metab.* **33**, 1000-1007 (2013).

164. Aizawa,N. *et al.* Correlation between structure/function and optic disc microcirculation in myopic glaucoma, measured with laser speckle flowgraphy. *BMC. Ophthalmol.* **14**, 113 (2014).

165. Nizar,K. *et al.* In vivo stimulus-induced vasodilation occurs without IP_3 receptor activation and may precede astrocytic calcium increase. *J. Neurosci.* **33**, 8411-8422 (2013).

166. Biesecker,K.R. & Srienc,A.I. The functional role of astrocyte calcium signaling in cortical blood flow regulation. *J. Neurosci.* **35**, 868-870 (2015).

167. Paukert,M. *et al.* Norepinephrine Controls Astroglial Responsiveness to Local Circuit Activity. *Neuron* **82**, 1263-1270 (2014).

168. Bonder,D.E. & McCarthy,K.D. Astrocytic Gq-GPCR-linked IP3R-dependent Ca^{2+} signaling does not mediate neurovascular coupling in mouse visual cortex in vivo. *J. Neurosci.* **34**, 13139-13150 (2014).